Connecting mantle flow below passive margins and intraplate melt generation: an application to the Cameroon Volcanic Line.

MATTHEW DAVID CALLUM LIKELY

Connecting mantle flow below passive margins and intraplate melt generation: an application to the Cameroon Volcanic Line.

Matthew David Callum Likely

Department of Earth Sciences

Durham University

A thesis submitted for the degree of

Master of Science by Research (MScR)

2022

Abstract

Mantle plumes are the prevailing explanation for intraplate volcanism, with an age progression along the plume track and a geochemical signature suggesting a core-mantle boundary origin. But these observations do not correlate with some intraplate volcanism examples, requiring alternative mechanisms to explain these outliers.

One potential example is the Cameroon Volcanic Line (CVL), a large-scale near-linear chain, lacking an age progression with a suspected asthenospheric origin. Edge-driven convection (EDC) is a proposed mechanism and is a process which forms in regions of lithospheric thickness gradients, such as craton-oceanic boundaries. A self-sustained convection roll may form, bringing material from depth to decompress and melt. However, previous EDC work provides disagreeing results, and shows that melt generation in this process is a complex process. This thesis aims to test a recent hypothesis that an additional 'fertile layer', derived from metasomatized material at the base of a craton which has undergone continental collision, could aid in magma genesis and explain why EDC-derived melt is not widespread.

The use of 2D numerical models allows for a parameter sensitivity study on rheological parameters, with an ocean spreading model used to test additional parameters and examine the dynamics of this hypothesized fertile layer, which is used as a proxy for melt generation. Results show that oceanic spreading velocity is the most influential parameter in moving fertile material into the continent-ocean transition (COT), as shear-driven upwelling forms at higher velocities.

When applying the results to the CVL, fertile material moves into the COT, while EDC occurs as well. However, due to the slow spreading rate of the Atlantic, processes such as shear-driven upwelling is not influential. As such, it is proposed that further additional factors must influence the magmatism, and that modelling of the 3D geological complexities of the CVL is required to gain further insight.

Contents

Abstract 2

Declaration 7

Acknowledgements 8

Introduction 9

1.1 Intraplate Volcanism 9

1.2 The Cameroon Volcanic Line 10

1.2.1 Geological & Tectonic Setting 11

1.2.2 Cameroon Volcanic Line Geochemistry 14

1.3 Alternative Mechanisms for Intraplate Volcanism 15

1.3.1 Afar Plume Theory 16

1.3.2 Mid-Scale Convection Cells 17

1.3.3 Small-Scale Convection & Edge-Driven Convection 18

1.3.4 A Suitable Model for the Cameroon Volcanic Line 20

1.4 Melt Generation Mechanism Beneath the Cameroon Volcanic Line 21

1.5 The Conceptual Model of the Metasomatized Layer 22

1.6 Thesis Outline 25

1.6.1 Aims of this Thesis 25

1.6.2 Structure of this Thesis 26

Methodology 27

2.1 Governing Equations and Assumptions 27

2.1.1 The Conservation of Mass 27

2.1.2 The Conservation of Momentum 28

2.1.3 The Conservation of Energy 28

2.1.4 The Conservation of Composition 28

2.2 Rheology 29

2.2.1 Sublithospheric Rheology 30

2.2.2 Lithospheric Rheology 31

2.3 Initial 2D Static Lithosphere Model – Physical Setup 32

2.3.1 Dimensions, Implementation and Boundary Conditions 32

2.3.2 Implementation of a Reference Viscosity 33

2.3.3 Thermal Model Setup 35

2.4 ASPECT & Technical Model Setup 36

Mantle Dynamics Associated with Intraplate Volcanism: A Parameter Sensitivity Study ... 38

3.1 Introduction and Rationale 38

3.2 Parameter Sensitivity Study 42

3.2.1 Diffusion Creep Pre-factor 42

3.2.2 Dislocation Creep Pre-factor 43

3.2.3 Grain Size 45

3.3 Optimal Viscosity Profiles 47

3.4 Static Lithosphere Numerical Model Results 49

3.4.1 The Evolution of Convective Processes 51

3.4.2 Metasomatized Layer Dynamics 51

3.5.1 Metasomatized Layer Dynamics and its Correlation to the Cameroon Volcanic Line Geometry 52

Mantle Dynamics During the Opening of an Ocean 56

4.1 Ocean Opening Models 56

4.2 Model Setup 57

4.3 Ocean Opening Reference Model Results 60

4.3.1 Density of the Fertile Material 61

4.3.2 Oceanic Spreading Rate 63

4.3.3 Relative Compositional Position of the Metasomatized Layer 65

4.4 2D Atlantic Ocean Opening Model Discussion 68

4.4.1 The Nature of Oceanic Spreading Models 68

4.4.2 The Effect of Half-spreading Rate Velocity 69

4.4.3 Metasomatized Layer Parameters and Their Implications 69

Discussion 71

5.1 Introduction 71

5.2 2D Static Lithosphere Model Comparison 71

5.2.1 Model Setup Comparison 71

5.2.2 Mantle Dynamics 73

5.2.3 Effects of a Metasomatized Layer on Melt Generation 73

5.3 Implications of an Ocean Opening Model 74

5.4 Parameter Controls on Metasomatized Layer Drainage and Their Influence on Intraplate Volcanism 78

5.4.4 Application to the Cameroon Volcanic Line 81

5.6 Model Limitations and Future Work 83

Conclusion 86

Bibliography 88

Appendices 107

Appendix A 107

Appendix B 108

Appendix C 109

Declaration

I, Matthew David Callum Likely, declare that this thesis, presented for the degree of Master of Science at Durham University, is a result of my own original research and has not been previously submitted to Durham University or any other institution. I have clearly indicated, when appropriate, the contributions of colleagues and have made every effort to acknowledge all collaborative work.

Matthew David Callum Likely

Durham University

June 2022

Acknowledgements

I would firstly like to thank both Jeroen van Hunen and Jenny Jenkins for their time, patience and guidance over these past, unprecedented 18 months. They kept me and this project moving forward, and even pushed me to disseminate results at both national and international conferences, something I would not have pictured myself doing prior to this project. I would like to also show my gratitude to Bethan Williams for her exceptional support both before and during this project, as without her I probably would not be in the position I am today. I am grateful for the unconditional love and support from my family during my academic journey, even if you don't quite know what it is I do, thank you. Shout out to Amelia Thacker & Owain Smith for their emotional and geophysical support, you've definitely made these past 4 years at Durham easier. A broad thank you to: Charlotte Elliot, Dan Coleman, Dániel Adorján, Faiz Zaman, Holly Whittome, Josh Hill, Keke Xu, Kyle Kean, Max Kirk, Sophie Buss & everyone I had the pleasure of competing with/against in Archery and Ultimate during my time at Durham.

This work has made use of the Hamilton HPC Service of Durham University and we thank the Computational Infrastructure for Geodynamics (geodynamics.org) which is funded by the National Science Foundation under award EAR-0949446 and EAR-1550901 for supporting the development of ASPECT.

This thesis is dedicated to my late friend Bartosz Kusiak

Love and miss you man.

Chapter 1

Introduction

1.1 Intraplate Volcanism

The vast majority of volcanoes on Earth are produced through processes described by plate tectonics, but this does not account for the ~10% of 'intraplate volcanism'. Traditionally, mantle plumes have been used to explain intraplate volcanism; characterised by volcanic chains with clear age progression as the lithosphere moves over the relatively stationary plume, giving rise to a younger, hotter and buoyant edifice. These volcanic chains have a unique Ocean Island Basalt (OIB) geochemistry, which pins their origin deep within the Earth at the Core-Mantle Boundary (CMB) (Wilson, 1963; Morgan, 1971; Larson, 1991; Stein & Hofmann, 1994; Storey, 1995; White, 2010). However, some intraplate volcanism cannot be explained by either plate tectonics nor mantle plume processes.

These remaining intraplate volcanic outliers lack characteristics of a plume-derived volcanic chain, with an asthenospheric origin (e.g. Lee *et al.,* 1994; Déruelle *et al.,* 2007; De Plaen *et al.,* 2014), lack of age progression (e.g. Fitton & Dunlop, 1985; Fitton, 1987) and no deep-seated positive thermal anomaly (e.g. Reusch *et al.,* 2010, 2011; Celli *et al.,* 2020; Boyce *et al.,* 2021b). One such example is the Cameroon Volcanic Line (CVL), a large-scale volcanic chain possessing the features of a non-plume driven volcanic chain and a focus of this study.

Prior explanations for non-plume driven intraplate magmatism have, thus far, failed to produce a mechanism that fits all observables. For example, geochemical observations suggests a plume influence, albeit masked by contamination (Lee *et al.,* 1994; Kamgang *et al.,* 2013) , but seismic tomography is unable to identify a deep-seated thermal anomaly associated with a mantle plume (Forte *et al.,* 2010; Reusch *et al.,* 2010, 2011; Celli *et al.,* 2020; Boyce *et al.,* 2021b). Furthermore, geodynamical models show conflicting results on alternative mechanisms and their melt generation

(e.g. King & Anderson, 1995, 1998; Ebinger & Sleep, 1998; Meyers *et al.,* 1998; Kaislaniemi & van Hunen, 2014; Córdoba & Ballmer, 2021; Negredo *et al.,* 2022). A model that can fit all of these observations could have profound implications on our understanding of magma genesis, lithosphere evolution and its stability.

This chapter is split into two sections with the first examining the observations along the CVL, and the second investigating the physical concepts, proposed theories and literature which reviews them, as well as the potential mechanism for melt in the CVL.

1.2 The Cameroon Volcanic Line

The Cameroon Volcanic Line (CVL) is a 1600 km, near-linear chain of volcanoes and seamounts running 30°N from the island of Pagalu to Lake Chad [Figure 1.2]. As such, it crosses both oceanic and continental lithospheres, with 6 major volcanoes on the oceanic sector and numerous volcanoes, including plutonic anorogenic complexes and monogenic cones, on the continental sector (Montigny *et al.,* 2004; Déruelle *et al.,* 2007; Njome & de Wit, 2014). The geochemistry across these sectors shows similar trace element signatures and Sm/Nd isotopic ratios, suggesting that neither oceanic nor continental crust play an important role in magma genesis. Instead a single sublithospheric source has been suggested as the origin of the magmatism (Rankenburg *et al.,* 2005; Déruelle *et al.,* 2007).

The CVL shares many similarities with a prolonged magmatic province in the NE of Brazil, which formed contemporaneously. Volcanism of the Fernando de Noronha displays no age progression and is present on both continental and oceanic lithosphere (Knesel *et al.,* 2011; Perlingeiro *et al.,* 2013; Souza *et al.,* 2013). The geochemistry of these alkaline rocks also suggests an asthenospheric origin, with trace element signatures of the oceanic sector indistinguishable from those along the oceanic sector of the CVL (Halliday *et al.,* 1992), with the continental sectors displaying a greater scatter of Sr- and Nd-isotope data due to contamination from the continental crust (Gerlach *et al.,* 1987; Halliday *et al.,* 1988; Lee *et al.,* 1994; Fodor *et al.,* 1998). Volcanism has been long lived, with the magmatic events along both Fernando de Noronha and the CVL occurring from 52 Ma to

1 Ma and 65 Ma to Present respectively (Knesel *et al.*, 2011; Perlingerio *et al.*, 2013; Souza *et al.*, 2013; Njome & de Wit, 2014), with the last eruption from Mt. Cameroon in 2000 (Suh *et al*., 2003; Déruelle *et al*., 2007). Both chains formed 40-50 Myr after the opening of the Atlantic (Guimarães *et al.*, 2020), making a plume origin hard to reconcile, as the likelihood of two plumes moving at a similar rate to the spreading rate of the Atlantic and producing indistinguishable melt, is very low.

Investigating this type of volcanism will provide a better understanding of the Earth's interior dynamics and supercontinent evolution, and may be applied to other non-plume driven intraplate volcanism examples.

1.2.1 Geological & Tectonic Setting

On average, the crust within the African continent is old with several cratons and associated shields forming in the Archean and Paleo/Mesoproterozoic. These ancient pieces of lithosphere are dominant in the Western (West African Craton), Central (Congo Craton) and Southern (Kalachari craton) regions of the continent. The basement under the Northern and Eastern parts of Africa are almost exclusively Neoproterozoic, with the Saharan Metacraton, a craton that has been remobilised during an orogenic event but with cratonic characteristics still identifiable (Abdelsalam *et al*., 2011), a major feature in the North (van Hinsbergen et al., 2011). The youngest areas of Africa are orogenic zones such as the Cape and Mauritanide dating back to the Late Palaeozoic (Lécorché *et al.*, 1991; Hansma *et al.*, 2016), and the Atlas Orogen even younger, Mesozoic to Cenozoic (Missenard *et al.*, 2006; van Hinsbergen *et al*., 2011).

Western Africa had a close geological and tectonic relationship with eastern South America until the breakup of Pangea. As a result, remnants of a large mountain belt, which formed in the Neoproterozoic and once ran through Brazil and Western Africa, can still be seen in Africa in the form of the Oubanguides. This belt was a result of the collision which formed Gondwana between the three main cratons: the São Francisco craton in South America and the West African and Congo cratons in Africa (Castaing *et al.*, 1994; Ngako *et al.*, 2003; Toteu *et al.*, 2004).

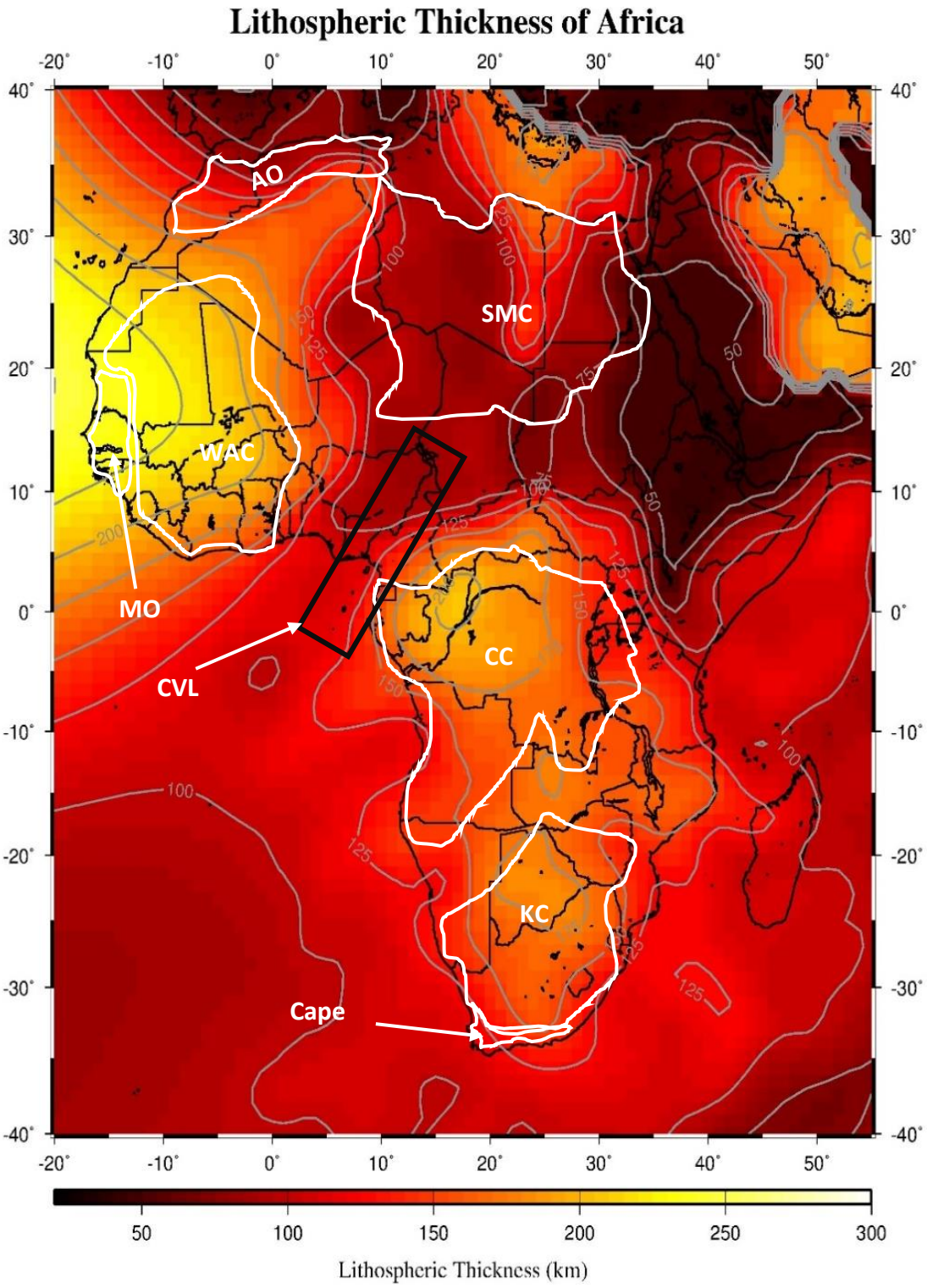

Figure 1.1. A map of lithospheric thickness of the African continent with the Cameroon Volcanic Line (CVL) outlined by a black box. Outlined in white are the: Congo Craton (CC); West African Craton (WAC); Kalachari Craton (KC); Saharan Metacraton (SMC); Atlas Orogen (AO); Mauritanide Orogen (MO) and Cape (Adapted from van Hinsbergen et al., 2011).

There are three main units identified north of the Congo Craton [Figure 1.2] ordered from south to north: Yaounde Domain (Neoproterozoic), Adamawa-Yade Domain (Paleoproterozoic) and the Western Cameroon Domain (Neoproterozoic). The contrasts in age are a result of the Sanaga Shear Zone and the Tchollir-Banyo Shear Zone (TBSZ) which form the boundaries of the domains. Both these shear zones are thought to be derived from the much larger Central African Shear Zone (CASZ) which extends from Dafur, Sudan, across the African continent to the Adamawa Plateau in Cameroon (e.g. Castaing *et al.*, 1994; Toteu *et al.*, 2004). Due to the CASZ being Precambrian in age, it is thought that the Pernambuco lineament which runs through Brazil is a possible extension emplaced before the Pan-African split (Dorbath *et al.*, 1986; Poudjom Djomani *et al.*, 1995). Reactivation of strike-slip faults along the CASZ resulted in a ≥40 km dextral displacement (Daly *et al.*, 1989), which occurred during the opening of the South Atlantic (~130 Ma) and allowed for subsiding rift basins to be infilled with Cretaceous-Tertiary sediments (Fairhead, 1988).

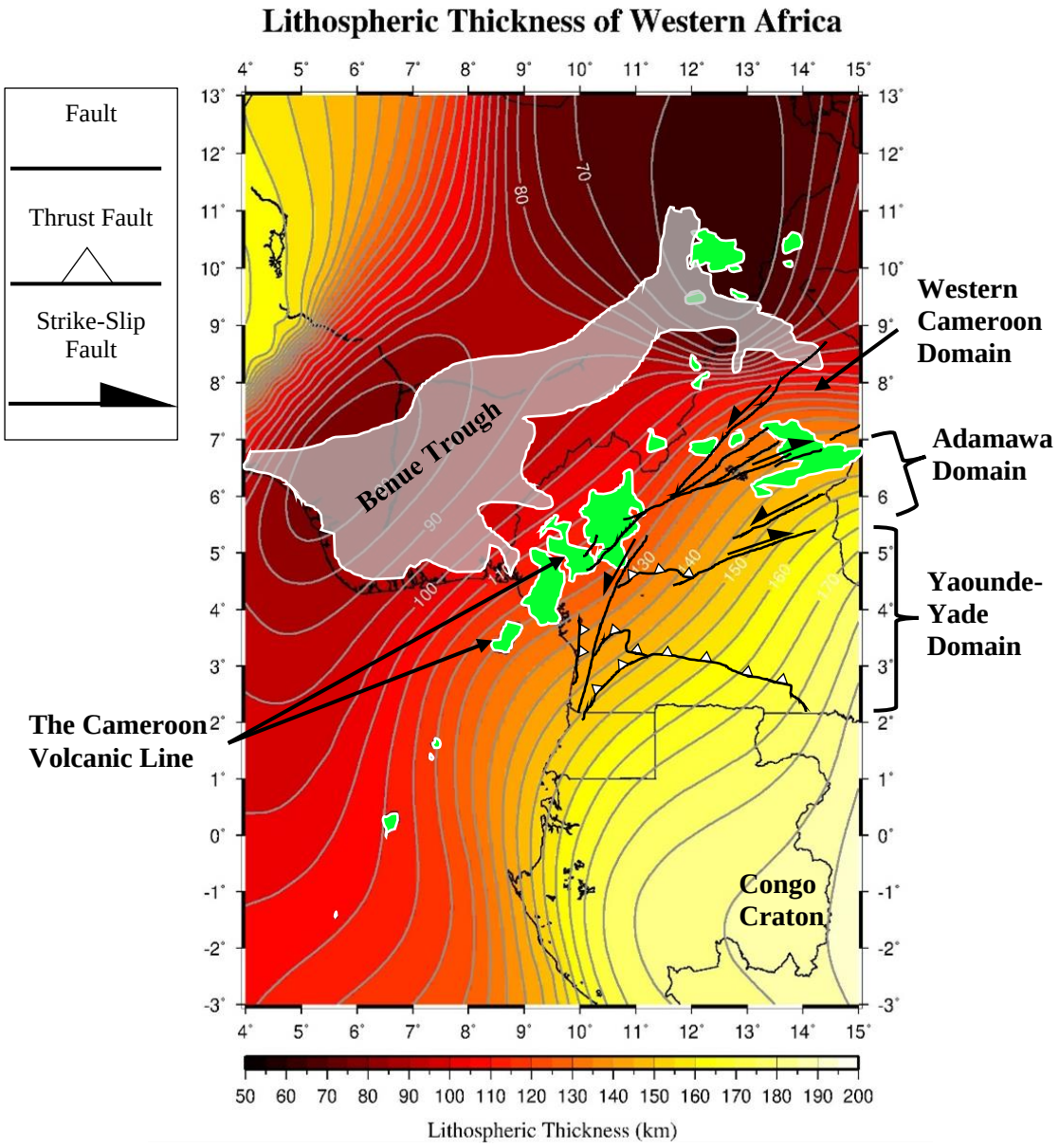

Figure 1.2. Lithospheric thickness map of Western Africa, with the outlines of the continent and countries within. Contours are in increments of 5 km, with annotation every 10 km. The Benue Trough is highlighted in grey and its formation is associated with a failed rift arm during the opening of the Central Atlantic. The volcanic massifs seen at the surface are coloured green, and the basic tectonics of the area have been highlighted (Adapted from Henriques & Neto, 2019).

1.2.2 Cameroon Volcanic Line Geochemistry

Investigating the geochemistry of igneous rocks can give vital insight in the melt composition, and thus, their origin. The volcanic material produced by the CVL is mostly alkaline basalt, with the basalts from the oceanic and continental sectors possessing very similar chemical and isotopic compositions (Fitton & Dunlop, 1985; Fitton, 1987). Lee *et al.* (1994) investigated the three volcanic islands along the oceanic sector. They utilised ^{40}Ar-^{39}Ar data as well as pre-existing K-Ar

ages, concluding they have all been active in the last 5 Ma. They notice the earliest volcanic ages along Principe, São Tome and Pagalu (31, 13 and 4.8 Ma respectively (Dunlop & Fitton, 1979)) correlate with the overall motion of the African plate whilst having similar ratios of Sr, Nd and Pb, implying a common source. Lee *et al.* (1994) suggest that the initial magmas were potentially from an upper mantle source which was entrained by a plume, with a HIMU (high μ = high $^{238}U/^{204}Pb$) component from the lower mantle modifying the magma conduits over time. This initial material shows signs of depletion and enrichment indicative of components such as depleted mid-ocean ridge basalt mantle (DMM) and enriched mantle one (EM1), which is thought to be derived from the recycling of pelagic sediment (Weaver, 1991; Woodhead *et al.,* 1993) or the metasomatized subcontinental upper mantle (Zinder & Hart, 1986; Tatsumoto & Nakamura, 1991; Elkins- Tanton, 2007). Kamgang *et al.* (2013) supports this with the idea that a HIMU source hybridises with asthenospheric melts, producing the anomalous signatures in Sr and Eu seen in mafic rocks in the Bamenda Mountains, Cameroon. However, with tomographic imaging (Forte *et al.,* 2010; Reusch *et al.,* 2010, 2011; Celli *et al.,* 2020; Boyce *et al.,* 2021b) there appears to be a lack of deep-seated thermal anomalies, like those seen in some mantle plume examples (e.g. Afar (Boyce *et al.,* 2021a), Hawaii (French & Romanowicz, 2015), Yellowstone (Yuan & Dueker, 2005)). Nevertheless, the resolution of such imaging techniques and the complex nature of mantle plumes suggests an atypical plume origin cannot be ruled out.

1.3 Alternative Mechanisms for Intraplate Volcanism

Potential geophysical and geodynamic models of the CVL, and alternative intraplate volcanism mechanisms, gained traction at the turn of the century. Theories ranged from direct plume interaction (Burke, 2001), plume material migration (Ebinger & Sleep, 1998), large-scale mantle convection convergence (Meyers *et al.,* 1998) and small-scale convection (King & Anderson, 1995, 1998; King and Ritsema, 2000). Here we will assess the main theories to distinguish which is the most probable.

1.3.1 Afar Plume Theory

With multiple areas of magmatism in the African continent, Burke and Wilson (1976) initially proposed ~40 volcanic hotspots beneath the continent, yet Duncan and Richards (1991) could only confirm one clearly identifiable hotspot. Trying to reconcile these studies to explain how on plume can produce this scattered volcanism, Ebinger and Sleep (1998) suggested that material from the Afar plume was migrating via lithospheric thickness differences, to different regions across the continent, similar to that of a drainage basin in river systems [Figure 1.3]. This migration of plume material could explain why there are no deep-seated thermal anomalies observed under such volcanic regions, as well as the contamination of HIMU melts by the entrainment of material as it travels along the base of the lithosphere.

The thermal anomalies observed by Reusch *et al.* (2010) are confined to the upper mantle (300 km), whereas the model proposed by Ebinger & Sleep (1998) would produce a low velocity anomaly at <100 km. Other issues with this model include its inability to explain the lack of age progression, but ultimately the most compelling evidence against this model is the fact that the Afar plume impinged 45 Ma (Ebinger & Sleep, 1998; Bastow *et al*., 2008) and it is thought that it would take material 40 Myr to travel to the Adamawa Plateau (Reusch *et al.*, 2010). Yet the CVL has experienced volcanism for at least 65 Myr (Njome & de Wit, 2014). If other, unknown plumes were found to have impinged under the African continent at a time before the volcanism seen along the CVL, this theory could still be viable, however with present day observations this model is not favourable in terms of the CVL's origin.

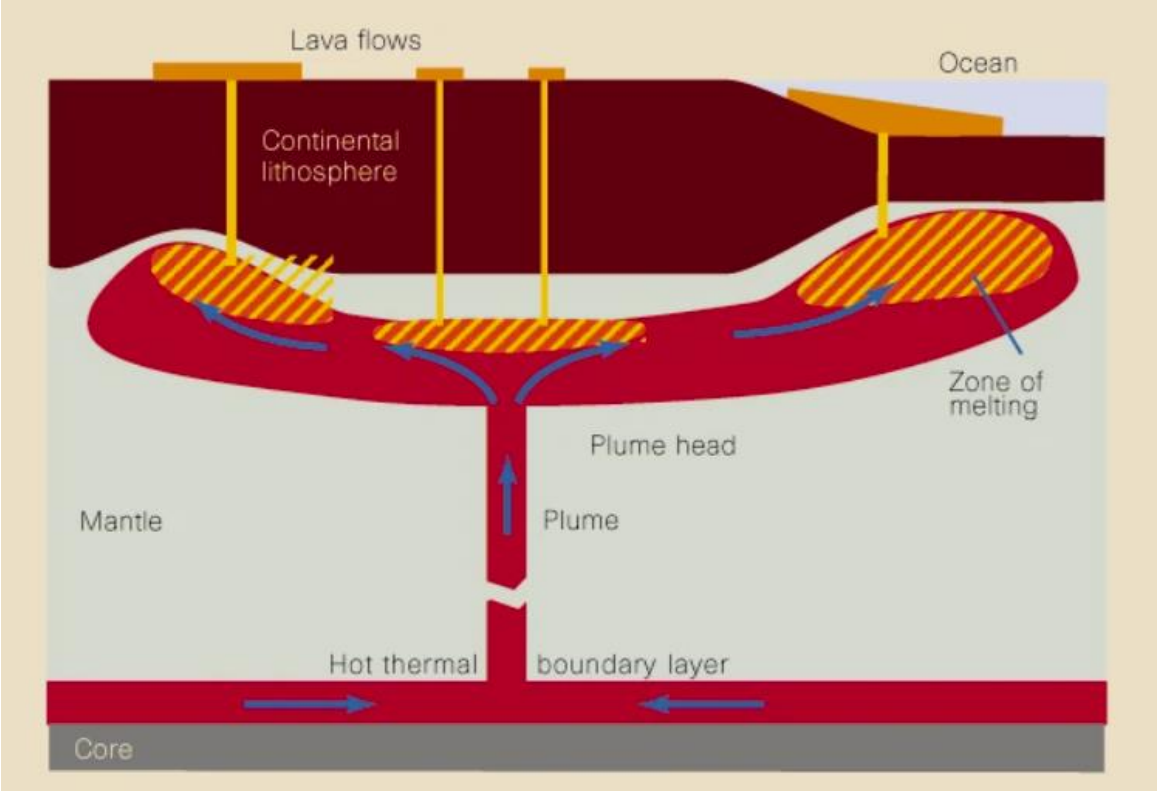

Figure 1.3. The proposed 'single plume' model to explain the scattered volcanism across the African continent, including the Cameroon Volcanic Line. The plume head material diverges from its initial point of contact and begins to flow into areas of thinner lithosphere. As it does so, decompression melt can form (taken from Ebinger and Sleep, 1998).

1.3.2 Mid-Scale Convection Cells

Whilst investigating deep-imaging seismic and gravity results from the Cameroon Volcanic Line (CVL), Meyers *et al*. (1998) discussed its possible origin, as well as other NE trending volcanic chains and rises off West Africa. They suggest that these volcanic chains are the product of hot upwelling flow currents resulting from two cylindrical Rayleigh-Bernard convection rolls (henceforth referred to as mid-scale convection cells), the result of small-scale instabilities (Korenaga & Jordan, 2004). These rolls are driven at the 660 km discontinuity as a result of heat transfer and shearing by the convection in the lower mantle [Figure 1.4]. Observations of the transition zone thickness (TZT), defined by the thickness between the 410 km and 660 km discontinuities, would be able to distinguish if there is heating at these discontinuities. Localised heating would allow the phase change from ringwoodite to perovskite at a shallower depth, reducing the TZT. Reusch *et al.* (2011) found that the TZT in the Cameroon region was 251±10 km, similar to that of the global average which ranges from 242 to 260 km (Chevrot *et al.*, 1999; Lawrence &

Shearer, 2006), suggesting the 280 K thermal anomaly they observed in their 2010 study, did not extend as deep as the 660 km discontinuity. This result suggests that neither mid-scale convection cells or mantle plumes are the likely driving force of magmatism along the CVL.

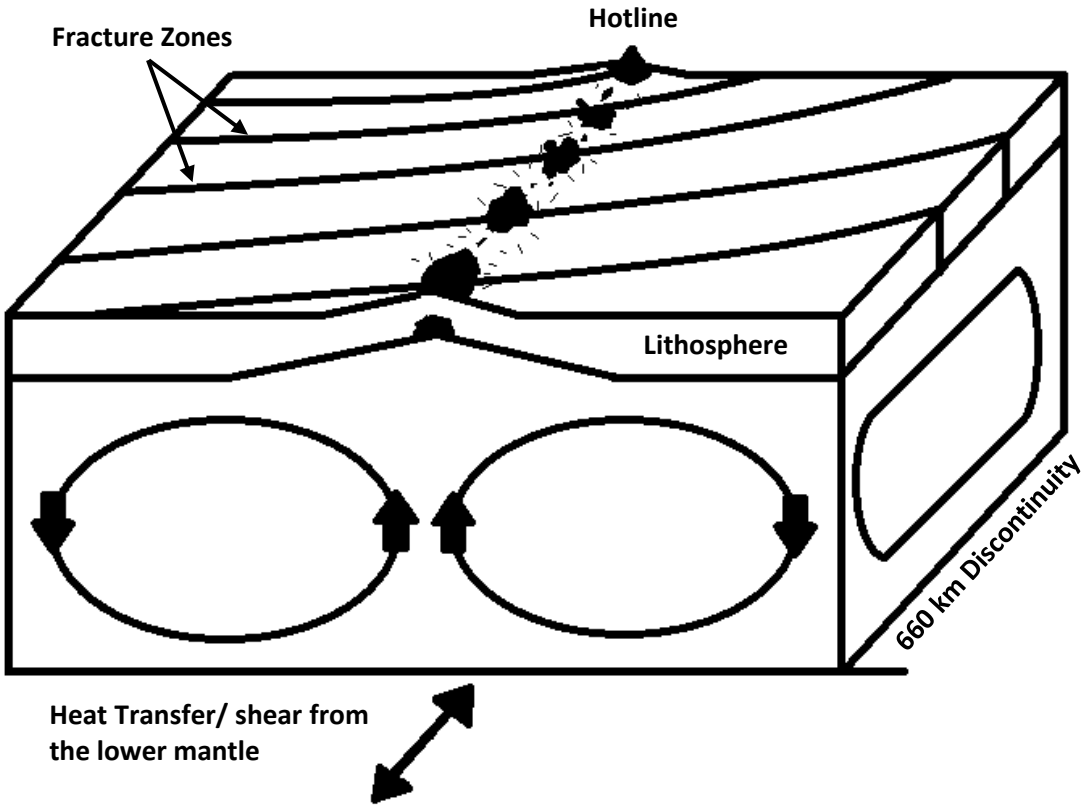

Figure 1.4. A simplified model illustrating the proposed mid-scale convection cells confined to the upper mantle. Heat transfer and shearing along the 660 km discontinuity allows for the formation of cylindrical, longitudinal convection rolls. Hotlines form between the upwellings of these convection rolls, where re-fertilized mantle from the 660 km discontinuity allows for enriched partial melt (adapted from Meyers et al., 1998).

1.3.3 Small-Scale Convection & Edge-Driven Convection

Edge-driven convection (EDC) was initially proposed by King & Anderson (1995, 1998) and entails lithospheric instabilities forming small-scale convection, which is able to self-organise due to a local flow at the edge of a thick lithosphere, or, more precisely, at a significant gradient (an 'edge') in the thickness of the lithosphere. As knowledge on the chemical, mechanical and thermal properties of cratonic roots is limited, there is a difficulty in placing a minimum lithospheric thickness. Numerical experiments have, however, suggested that 150 km is the minimum lithospheric thickness required to allow for EDC to form and sustain (Lenardic *et al.*, 2003). Kaislaniemi & van Hunen (2014) find that there is potentially two types of EDC: stricto sensu

(EDC_{SS}) which is the type initially described by King and Anderson (1995, 1998), where an instability at the edge of the craton produces a lithospheric downwelling, forming a subsequent upwelling under the thinner lithosphere [Figure 1.5a]; edge-driven convection with asthenospheric shear (EDC_{WS}), convection which is similar to its EDC counterpart, however there is a greater influence via shear flow providing a convection roll moving in the opposite direction, with warmer material upwelling below the craton, and downwelling below the thinner lithosphere. This asthenospheric flow can induce a second, smaller convection roll in the continent-ocean transition, invoking melt [Figure 1.5b]. As intraplate volcanism associated with edge-driven convection is not observed at every craton-oceanic boundary, there may be specific conditions required to produce melt. For example, an increase in mantle temperature (e.g. via either an influx of heat or by greater radiogenic heating) or alternatively, an increase in the presence of volatiles in the mantle which could lower the solidus enough to produce sufficient melt.

An argument against EDC as the origin for the CVL made by Adams *et al.* (2015) stems from the continuation of volcanism in the oceanic sector, whilst there is no adjacent craton. They argue that convection rolls formed by EDC are parallel to the craton boundary, so the oceanic sector should continue to follow the craton boundary south, instead of remaining linear. However, a 3D EDC model by Kaislaniemi & van Hunen (2014) does not necessarily show this, with velocity vectors running both parallel and perpendicular to the craton boundary. This means flow, and therefore melt, could be produced in either of these directions in relation to the craton.

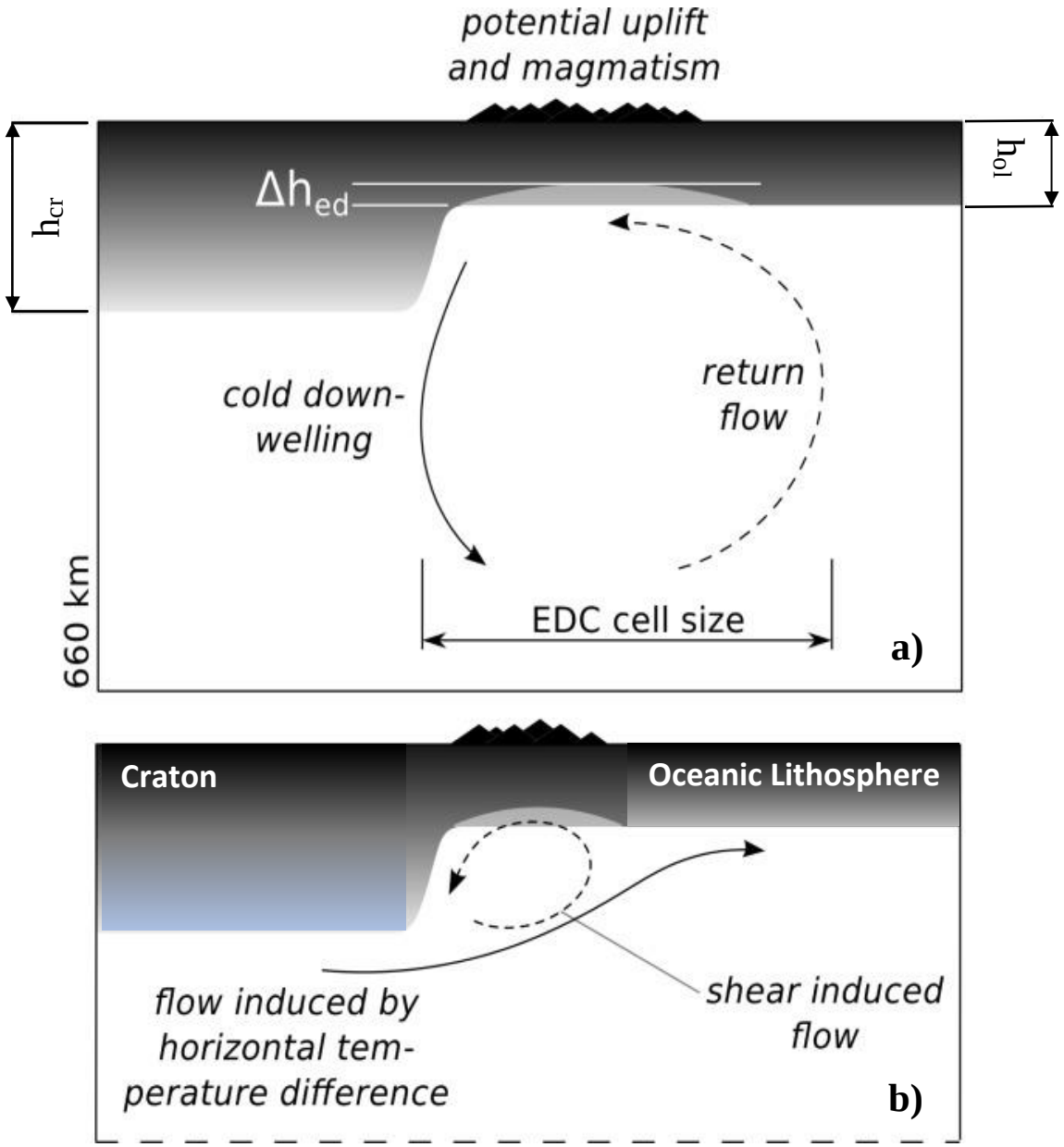

Figure 1.5. Diagrams of the two types of edge-driven convection, with h_{cr} and h_{oc} denoting the thickness of the craton and oceanic lithospheres respectively. The first (a) is of edge-driven convection stricto sensu (EDC_{SS}), which has cooler material below the craton forming a downwelling. This downwelling then forms a subsequent upwelling beneath the thinner lithosphere, producing convection. The second (b) is edge-driven convection with shear (EDC_{WS}), and is characterised by warm material below the thicker lithosphere which rises up toward the thinner lithosphere, inducing shear as it flows (adapted from Kaislaniemi & van Hunen, 2014).

1.3.4 A Suitable Model for the Cameroon Volcanic Line

Reusch *et al.* (2010) investigated potential models for the origin of the CVL by using seismic tomography to image the region below. They could only observe <300 km deep due to limitations in model resolution. They observed a thermal anomaly at 300 km depth, which narrowed the

potential candidates down to edge-driven convection or mid-scale convection cells, as they found little evidence to support a mantle plume or the 'one plume' theory (Ebinger & Sleep, 1998). Reusch *et al*. (2011) later investigated the transition zone thickness (TZT) between the 410 km and 660 km discontinuities. Here they aimed to determine whether whole mantle Rayleigh-Bernard convection rolls or edge-driven convection (EDC) was the cause of magmatism at the CVL. If the former were to be true, a thinner than average TZT would be observed due to heating below the 660 km discontinuity, while the latter has no effect on TZT as EDC does not require excess heating from the lower mantle. They found that the TZT showed no difference compared to the global average, with both low velocity and high velocity anomalies confined to the 660 km discontinuity, but with no evidence of excess heating, and as such they deduced that EDC was more likely. Recent investigations by Boyce *et al.* (2021b) and Celli *et al*. (2020) indicate that there is a complex signature at the 410 km discontinuity, with the 660 km discontinuity remaining at a depth relatively similar to the global average. This observation also suggests that mid-scale convection is not the source of volcanism, as the 660 km discontinuity would be shallower through heating from the lower mantle. The dynamics of the region is still unclear, and new constraints are needed to obtain a better understanding.

1.4 Melt Generation Mechanism Beneath the Cameroon Volcanic Line

There are broadly three mechanisms in producing melt: hot material subjected to a reduction in pressure producing decompression melt (e.g. mid-ocean ridge); a region of anomalously greater temperature allowing the solidus of a material to be surpassed (e.g. mantle plumes); the presence of volatiles in a material, reducing the overall solidus and allowing melt at lower temperatures (e.g. subduction zones). If we are assuming edge-driven convection (EDC), as proposed by King & Anderson (1998) and King & Ritsema (2000) as the potential model for melt generation at the CVL, then the strong convection it forms in the upper mantle will allow material to heat up and then rapidly rise, forming decompression melt. Yet, this alone may not be enough to produce sufficient melt, as some EDC tests require either an increase in local temperature, or the addition of volatiles

in conjunction with the convection to produce melt (e.g. Córdoba & Ballmer, 2021; Negredo *et al.*, 2022).

Observations into the lithospheric thickness across the region [Figure 1.2] show the gradients between the two cratons (~200 km thick) and continental lithosphere (65-100 km thick) is large, due to the abnormally thin lithosphere below the Benue Trough. This thinness is associated with the early rifting it underwent during the formation of the Central Atlantic. It is thought that this region was once a rift arm associated with the opening of the Atlantic, which subsequently failed as rifting continued N-S (Fairhead & Okereke, 1990). However Milelli *et al.*, (2012) suggest its formation was a result of an instability event which occurs in regions possessing a low Rayleigh such as the African continent. Through their laboratory testing, Milelli et al., (2012) observed that buoyant, dense material (simulating a craton) developed instabilities at its edge when heated from below, which exhibited a geometric structure similar to those seen along the Benue Trough and CVL. This extension means that the continental lithosphere of the Benue Trough is similar in thickness to the neighbouring oceanic lithosphere (Bonvalot *et al.*, 2010; Fishwick & Bastow, 2011).

1.5 The Conceptual Model of the Metasomatized Layer

Throughout their long history, cratons have been subjected to metasomatism, making the base of the lithosphere weaker, denser and more fertile (Menzies *et al.*, 1987; Foley, 2008; Wenker & Beaumont, 2017; Eeken *et al.*, 2018; Afonso *et al.*, 2022). These metasomatic assemblages are derived from carbonate-rich melts (Foley, 2008; Tappe *et al.*, 2017; Groves & Santosh, 2021) and can become unstable spontaneously, which would lead to this material detaching from the overlying continent, and remelting if it sinks into the mantle (Elkins-Tanton, 2007). Events such as continental collision can further trigger its independence (Guimarães *et al.*, 2020): such collision would shorten and thicken the lithosphere, which transposes the fertile material to greater depths, and vertically stretches the geotherm. Over time, the geotherm slowly equilibrates to pre-collisional values, with the lithosphere-asthenosphere boundary moving upwards over time. This makes the metasomatized fertile layer (henceforth referred to as the ‘metasomatized layer’) become part of the hot, weak, and

mobile asthenosphere [Figure 1.6] (Guimarães *et al.*, 2020). Here it remains neutrally or positively buoyant below the base of the cratonic lithosphere, and may not migrate until the break-up of Pangea, where the metasomatized layer may begin to migrate with the associated induced asthenospheric flow. It is hypothesized that this fertile material may slowly start to drain into thinner lithospheres, where its fertility leads to additional melt (Guimarães *et al.*, 2020). For the case of the Cameroon Volcanic Line, the fertile material moves below the thin Benue Trough where it is channelled toward the oceanic lithosphere, which may explain the seismic anisotropy observations displaying a flow pattern NW-SE (Elsheikh *et al.*, 2014). This movement of fertile material from below the craton to the thinner lithosphere is thought to correspond to the 40 Myr delay in volcanism after the Atlantic Ocean opened, seen in the oldest rocks along the CVL (Njome & de Wit, 2014). The channelisation of material can lead to small-scale convection (Koch *et al.*, 2012) which can generate large-scale edge-driven convection (Kaislaniemi & van Hunen, 2014). Through EDC in conjunction with the fertile material migrating along the Benue Trough, melt will more readily occur, potentially explaining why volcanism occurs along the CVL but not more generally at craton-oceanic boundaries (e.g. Córdoba & Ballmer, 2021).

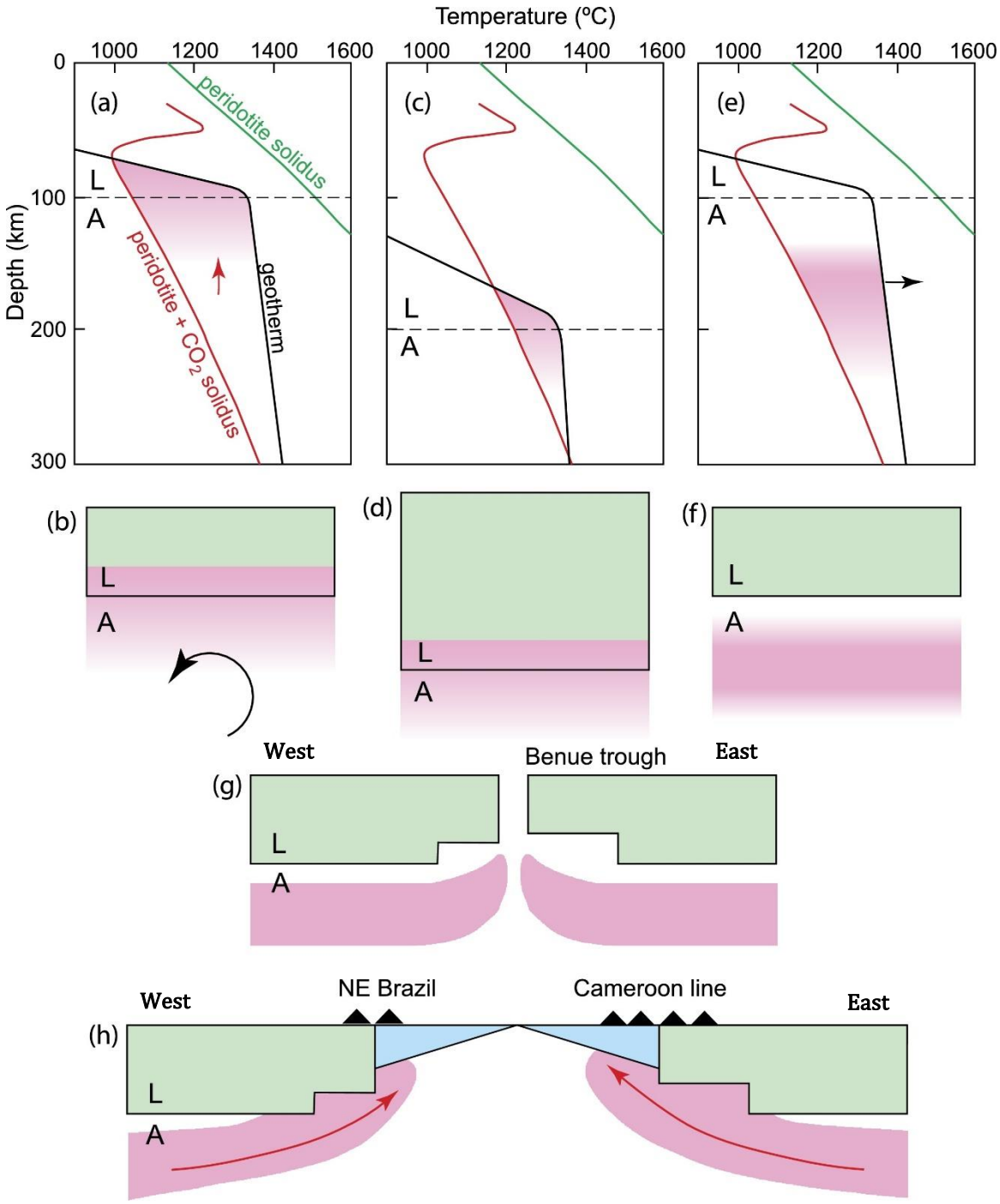

Figure 1.6, The thermal evolution of the metasomatized layer over time. Figures 1.6a – 1.6f show the evolution of the lithosphere-asthenosphere boundary (LAB) before, during and after continental collision. Figure 1.6g shows the mobilisation of the metasomatized layer into the Benue Trough as the Atlantic Ocean fails to rift here. Figure 1.6h shows the full migration of fertile material once the Atlantic opens, with material predicted to take 40-50 Myr to move into the oceanic lithosphere (taken from Guimarães et al., 2020).

1.6 Thesis Outline

1.6.1 Aims of this Thesis

The origin of non-plume driven intraplate volcanism observed along the Cameroon Volcanic Line (CVL) is poorly understood. This study will focus on the dynamics of a hypothesized subcontinental metasomatized layer and whether it can drain into the adjacent ocean basin and influence potential melt generation derived from EDC. The flow of such fertile material from below the craton and into the Benue Trough may explain the geometry of the CVL and why this type of volcanism does not occur at every craton-oceanic boundary. The link between basal weakening during episodes of supercontinents, and the dynamics of a metasomatized metasomatized layer is investigated through a series of numerical models.

The overall objectives of this thesis are to determine whether EDC can form in an environment similar to that found along the CVL, and to assess the dynamics of a subcontinental metasomatized layer and whether these match with the predictions made by Guimarães *et al*. (2020). The aims of this thesis can be broken down as follows:

Assess whether a proposed subcontinental fertile material can migrate to aid melt generation

The process of edge-driven convection may not be enough to produce melt by itself, so here we look to investigate whether the addition of a metasomatized layer below the base of the craton will move and mix in a region effected by edge-driven convection. Here, a continuous drainage of fertile material from the base of the cratonic lithosphere to thinner oceanic lithosphere may explain the long-lived volcanism along the Cameroon Volcanic Line.

Assess whether mantle flow due to the opening of the Atlantic plays a significant role in the formation of the Cameroon Volcanic Line

Whether the development of numerical models that include a spreading ridge impact edge-driven convection, mantle asthenospheric flow and metasomatized layer dynamics as oceanic lithosphere forms and matures. Here, we look at the key influential factors which may allow greater concentrations of fertile material into the thinner lithosphere.

1.6.2 Structure of this Thesis

The structure of this thesis follows the following layout:

Chapter 2 - outlines the governing geodynamical and rheological equations utilised within this study. The initial model set-up is described in terms of temperature, viscosity and flow field, with the general structure, initial conditions and boundary conditions described.

Chapter 3 – the testing of grain size, diffusion creep and dislocation creep pre-factors to help better understand their impacts on mantle flow. The development of a 2D static lithosphere model allows for observations into initial mantle and metasomatized layer dynamics.

Chapter 4: - the rationale, model setup and investigation of non-rheological parameters associated with the metasomatized layer are investigated through a 2D ocean opening model. The concentration of fertile material moving into the continent-ocean transition and the effects of shearing in the asthenosphere will be assessed for each parametric alteration, gaining an understanding in their impact on metasomatized layer mobility.

Chapter 5 – discussion on the obtained model results in context to previous literature with an application to the Cameroon Volcanic Line, as well as a discussion on the overall feasibility of the proposed hypothesis.

Chapter 6 – concluding remarks, the proposed limitations and some potential future follow up work.

Chapter 2

Methodology

This chapter is broken down into three main constituents:

- The governing equations applied to the models, specifically explaining the equations for the conservation of mass, momentum, energy and composition.
- Rheology, deformation and the material physics equations
- Basic model setup, including initial conditions, boundary conditions, and technical modelling aspects.

2.1 Governing Equations and Assumptions

Due to the highly viscous nature of the mantle, over long periods of time it acts as a fluid and as such, equations governing fluid dynamics can be applied when considering the dynamics of the Earth. These fluid equations can be defined in terms of the conservation of mass, momentum, energy and composition, with the parameters used in each equation found in Table 1.

2.1.1 The Conservation of Mass

The conservation of mass for a fixed control volume can be defined as the rate of change of the control volume's mass proportional to the rate of flow into or out of the volume (Ismail-Zadeh & Tackley, 2010). This can simply be described as:

$$\frac{\partial \rho}{\partial t} + \nabla \cdot (\rho \boldsymbol{u}) = 0 \tag{2.1}$$

Where ρ is the pressure and temperature dependent fluid density, t is time and $\boldsymbol{u}$ is the fluid velocity.

The Extended Boussinesq Approximation (EBA) assumes material is incompressible, with the density changes associated with the conservation of mass within the mantle small enough that they are negligible (e.g. Oxburgh & Turcotte, 1978; Christensen & Yuen, 1985; Gerya, 2010;

Gassmöller *et al*., 2020), and can consequently be ignored. As a result, this approximation simplifies the conservation of mass to:

$$\nabla \cdot \boldsymbol{u} = 0 \tag{2.2}$$

2.1.2 The Conservation of Momentum

The Navier-Stokes equation describes the conservation of momentum for a compressible fluid within a gravitational field. As previously stated, the EBA assumes that the mantle is an incompressible material, and as such the Navier-Stokes equation for the conservation of momentum can be simplified to leave the Stokes equation (Oxburgh & Turcotte, 1978; Christensen & Yuen, 1985).

$$\nabla \cdot (\eta \dot{\varepsilon}) - \nabla p + \rho \boldsymbol{g} = 0 \tag{2.3}$$

Where η is the dynamic viscosity, $\dot{\varepsilon}$ is the strain rate, p is the deviatoric pressure and $\boldsymbol{g}$ is the acceleration due to gravity. The assumption that mantle material is incompressible is valid as the mantle is a highly viscous fluid and as such, inertial forces are far smaller, and thus less impactful on the conservation of momentum than forces such as gravity and viscous resistance.

2.1.3 The Conservation of Energy

Besides advection and diffusion of heat, the EBA acknowledges the processes of shear heating and adiabatic heating, which leads to the following equation:

$$\rho C_p \left(\frac{\partial T}{\partial t} + \boldsymbol{u} \cdot \nabla T\right) - \nabla \cdot (k \nabla T) = \rho H + 2\eta \varepsilon(\boldsymbol{u}) : \varepsilon(\boldsymbol{u}) - \alpha \rho T (\boldsymbol{u} \cdot \mathbf{g}) \tag{2.4}$$

Where C_p is the specific heat capacity (at constant pressure), T is temperature, k is the thermal conductivity, H is the intrinsic specific heat production and α is the thermal expansion coefficient.

2.1.4 The Conservation of Composition

Material properties are tracked in the model setup, assuming no compositional diffusion or material changes. Such behaviour is described using a pure advection equation:

$$\frac{\partial c}{\partial t} + \boldsymbol{u} \cdot \nabla c = 0 \tag{2.5}$$

where c is the chemical composition of a material, t is time and $\boldsymbol{u}$ is the velocity vector.

Symbol	Parameter	Units
c	Composition of a material	-
C_p	Specific heat capacity	J kg^{-1} K^{-1}
$\boldsymbol{g}$	Gravitational acceleration	m s^{-2}
H	Rate of internal heat production	W kg^{-1}
k	Thermal conductivity	W m^{-1} K^{-1}
p	Pressure	Pa
T	Temperature	K
t	Time	S
$\boldsymbol{u}$	Velocity	m s^{-1}
α	Thermal expansion coefficient	K^{-1}
$\boldsymbol{\varepsilon}$	Strain rate	s^{-1}
η	Dynamic viscosity	Pa s
ρ	Density	kg m^{-3}

Table 1. A list of used symbols and parameter notation with associated units used in Section 2.1.

2.2 Rheology

How a rock deforms or flows in response to forces within the Earth's interior is known as its rheology, and a number of different deformation mechanisms are typically considered (Bürgmann & Dresen, 2008). In this section the deformation through dislocation and diffusion creep is defined, as well as the brittle deformation and failure within the crust and lithosphere. These defining rheologic processes are then combined to give the total effective viscosity, which shall be used during modelling. All parameters used to define the rheological equations in this section can be found in Table 2.

2.2.1 Sublithospheric Rheology

Within the Earth's mantle, both diffusion and dislocation creep are the dominant deformation mechanisms. Dislocation creep deforms material via dislocations in the crystal lattice, either through growth of imperfections or impurities. With this mechanism, strain rate increases nonlinearly with stress and, unlike diffusion creep, is insensitive to grain size. This mechanism of deformation is known to occur in the asthenosphere and upper mantle. As material deforms in a way which allows for a lattice preferred orientation (LPO), evidence of dislocation creep can subsequently be observed through seismic anisotropy (Karato & Wu, 1993), or in rock samples displaying microstructures with a LPO, which originated at ~200 km depth (Boyd, 1973; Karato & Wu, 1993).

Diffusion creep is the active transport of atoms through crystal interiors and between crystal grains via migration of crystal vacancies. This is most common in regions of low stress, small grain size or both. This mechanism increases linearly with stress and is most prominent within mantle deeper than ~300 km (Karato & Wu, 1993). Due to a decrease in seismic anisotropy observations below 200-300 km depth, it is inferred that diffusion creep becomes the dominant mechanism below these depths.

Both the viscosity resulting from diffusion and dislocation creep can be defined as:

$$\eta_i = \frac{1}{2} A_i^{-\frac{1}{n_i}} d^{\frac{m_i}{n_i}} \dot{\varepsilon}_i^{\frac{1-n_i}{n_i}} \exp\left(\frac{E_i^* + pV_i^*}{n_i RT}\right) \tag{2.6}$$

where d is the grain size, i relates to either dislocation creep or diffusion creep, $\dot{\varepsilon}$ the square root of the second invariant of the strain rate tensor, T is temperature, p is pressure and R is the ideal gas constant. A_i are the prefactors, n_i are the stress exponents, m_i is the grain size exponent which, for the modelling within this thesis, will remain constant providing no further physical meaning , E_i are the activation energies and V_i are the activation volumes (e.g. Billen & Hirth, 2007).

A composite viscosity, which combines deformation by both dislocation and diffusion creep, can be described as:

$$\frac{1}{\eta_{comp}} = \frac{1}{\eta_{diff}} + \frac{1}{\eta_{disl}} \quad (2.7)$$

where η_{diff} and η_{disl} are the viscosities resulting from diffusion creep and dislocation creep respectively.

2.2.2 Lithospheric Rheology

For rocks at lower temperature such as those situated in the lithosphere, brittle failure and deformation can occur through Mohr-Coulomb yielding (Byerlee, 1978). Within this thesis, this viscosity for 2D models is calculated through the Drucker Prager frictional plasticity criterion, with the 2D Drucker Prager yield surface equating to the Mohr-Coulomb surface (e.g. Thieulot, 2011):

$$\sigma_y = Psin(\phi) + Ccos(\phi) \quad (2.8)$$

where P is pressure, ϕ is the angle of internal friction and C is the value of cohesion. For the purpose of calculating the 'complete' or effective viscosity, Equation 2.8 can be converted to the yield viscosity:

$$\eta_y = \frac{\sigma_y}{2\varepsilon_{ii}} \quad (2.9)$$

With ε the square root of the second invariant of the strain rate tensor. The effective viscosity is then defined by the combination of the minimum values of composite viscosity, yield viscosity and the maximum viscosity (the upper limit emplaced on viscosity for numerical stability [see Section 2.3.2])

$$\eta_{eff} = \min(\eta_{comp}, \eta_y, \eta_{max}) \quad (2.10)$$

Where η_{eff} is the effective viscosity, η_{comp} is the composite viscosity, η_y is the yield viscosity and η_{max} is the maximum viscosity used during modelling.

Symbol	Parameter	Units
A	Pre-exponential exponent	$Pa^{-n}\,s^{-1}$
C	Cohesion	MPa
d	Grain size	m
E^*	Activation energy	$J\,mol^{-1}$
$\boldsymbol{i}$	Dependent of dislocation or diffusion creep	-
P	Pressure	Pa
R	Ideal gas constant	$J\,K^{-1}\,mol^{-1}$
T	Temperature	K
V^*	Activation volume	$cm^3\,mol^{-1}$
η_{comp}	Composite viscosity	Pa s
η_{diff}	Viscosity of diffusion creep	Pa s
η_{disl}	Viscosity of dislocation creep	Pa s
σ_y	Yield stress	Pa
Φ	Internal angle of friction	°

Table 2. A list of both symbol and parameter notation with associated units used with in Section 2.2.

2.3 Initial 2D Static Lithosphere Model – Physical Setup

2.3.1 Dimensions, Implementation and Boundary Conditions

The model is built as a box of dimensions 660 x 2640 km, allowing ample depth for the edge-driven convection cells proposed by King & Anderson (1998). This is comprised of three compositionally distinct materials [Figure 2.1]: a default mantle material which compositionally forms the oceanic lithosphere that is thermally 80 km thick, due to being assigned an age of 50 Ma. The oceanic lithospheric thickness is then calculated by a given isotherm. A 180 km compositional thick cratonic lithosphere and a 50 km thick layer at the base of the craton that contains a small percentage (a few percent) of fertile material.

Cratonic lithosphere is generally assumed to be both strong and chemically buoyant, with low volatile contents in cratonic peridotites from depletion related to ancient melting processes (Jordan, 1978; Pollack, 1986; Lenardic and Moresi, 1999; Sleep, 2003; Petit, 2010). To replicate this, the craton compositional block is assigned a viscosity of 1×10^{24} Pa s and a density of 50 kg m^{-3} lower than the mantle material.

The velocity boundary conditions for these lithosphere models are free-slip to allow for no inflow or outflow of material, and to ensure that all motion is driven by gravitational forces only. This setup implies that the upper-lower mantle transition is assumed to be fully impermeable.

Modified boundary conditions are used in Chapter 4, where details for that model are given.

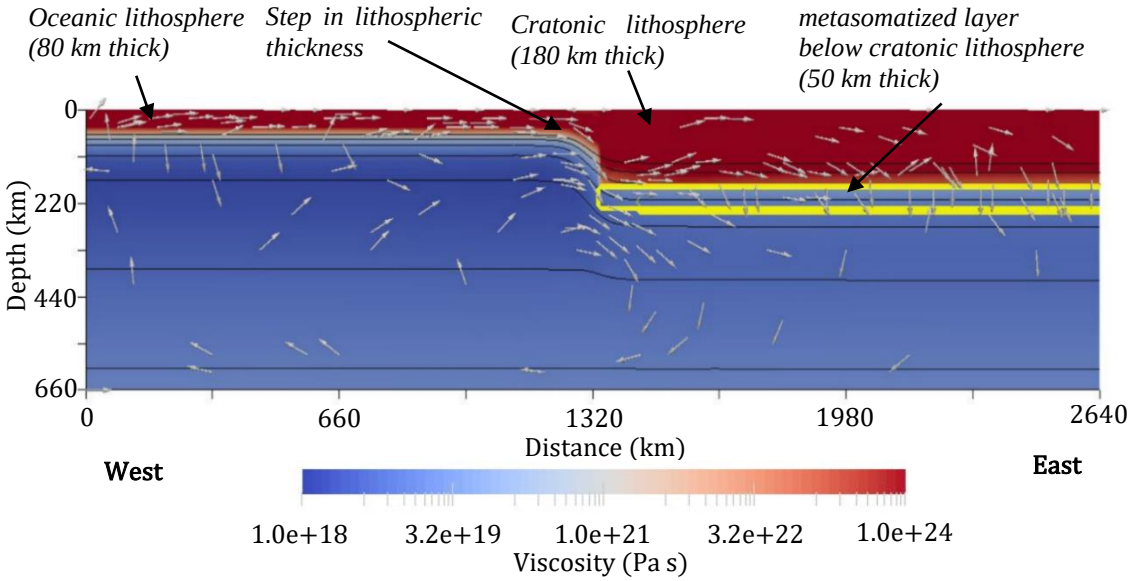

Figure 2.1. Model setup showing the initial conditions. The left lithosphere is oceanic with a half-space cooling thickness of around 80 km. The right lithosphere is a compositionally defined craton of 180 km thickness. Colours illustrate initial viscosity. The black contours are temperatures from 1173 K (taken as the estimated lithosphere-asthenosphere boundary temperature) to 1973 K (the maximum temperature of the initial model), with increments of 100 K. The yellow contour below the cratonic lithosphere outlines the subcontinental metasomatized layer.

2.3.2 Implementation of a Reference Viscosity

Typical values for viscosities within the mantle are hard to constrain, however investigations into the speed of post-glacial rebound (Gasperini & Sabadini, 1989; Forte & Mitrovica, 1996; Paulson *et al.*, 2007) provide viscosity values ranging from $1 \times 10^{21} - 1 \times 10^{22}$ Pa s, yet there is a large uncertainty attached (Schubert *et al.*, 2001). Default rheological parameters in the model are based

on laboratory studies by Hirth & Kohlstedt (2003) [Table 3]. A maximum and minimum viscosity (1×10^{24} Pa s and 1×10^{18} Pa s, respectively) are applied for numerical stability.

Parameter	*Metasomatized* Layer	Craton	Mantle
Activation energies for diffusion creep [J mol^{-1}]	375×10^{3}	375×10^{3}	375×10^{3}
Activation energies for dislocation creep [J mol^{-1}]	530×10^{3}	530×10^{3}	530×10^{3}
Activation volumes for diffusion creep [m^{3} mol^{-1}]	6.00×10^{-6}	6.00×10^{-6}	6.00×10^{-6}
Activation volumes for dislocation creep [m^{3} mol^{-1}]	14.0×10^{-6}	14.0×10^{-6}	14.0×10^{-6}
Angle of internal friction [°]	5.7392	5.7392	5.7392
Cohesion	20×10^{6}	20×10^{6}	20×10^{6}
Density [kg m^{-3}]	2800	3350	3400
Grain size [m]	1.00×10^{-3}	1.00×10^{-3}	1.00×10^{-3}
Heat capacity [J K^{-} kg^{-1}]	1250	1250	1250
Maximum yield stress [Pa]	1×10^{10}	1×10^{10}	1×10^{10}
Pre-factor for diffusion creep [Pa^{-1} m^{m} s^{-1}]	1.50×10^{-15}	1.50×10^{-19}	1.50×10^{-15}
Pre-factor for dislocation creep [Pa^{-n} s^{-1}]	1.00×10^{-16}	1.00×10^{-20}	1.00×10^{-16}
Stress exponent for dislocation creep [-]	3.50	3.50	3.50
Thermal diffusivity [m^{2} s^{-1}]	1.00×10^{-6}	1.00×10^{-6}	1.00×10^{-6}
Thermal expansivities [K^{-1}]	3.00×10^{-5}	3.00×10^{-5}	3.00×10^{-5}
Acceleration due to gravity [m s^{-2}]	9.81		
Grain size exponent [-]	3		
Internal mantle temperature [K]	1350		
Maximal temperature [K]	2000		
Maximal viscosity [Pa s]	1.00×10^{24}		
Minimal temperature [K]	273		
Minimal viscosity [Pa s]	1.00×10^{18}		
Radiogenic heating [W kg^{-1}]	25.0×10^{-12}		
Reference strain rate [s^{-1}]	1.00×10^{-16}		
Reference viscosity [Pa s]	1.00×10^{22}		

Table 3. List of rheological parameters and associated values for the three compositionally different layers: Metasomatized Layer, Craton and Mantle, as well as more general parameters which were kept constant throughout the modelling process.

2.3.3 Thermal Model Setup

Previous models investigating edge-driven convection have either produced a model with two thermal boundary layers at the top and bottom of the model (e.g. Córdoba & Ballmer, 2021), or with just a single boundary layer at the top, with the heat from the bottom boundary layer supplemented through increased radiogenic heating (e.g. Kaislaniemi & van Hunen, 2014; Negredo *et al.*, 2022). A thermal boundary layer at the base of the model will produce small plume-like features that interfere with the formation and sustainment of EDC. This complicates the analysis of the EDC dynamics, and therefore a model setup without a bottom thermal boundary layer is adopted in all models in this thesis. To compensate for the absence of basal heat flowing into the model, an increase in radiogenic heating is used to sustain upper mantle temperatures (Kaislaniemi & van Hunen, 2014; Negredo *et al.*, 2022), with the base of the model defined as the reference temperature of the mantle [Table 3]. Models also have a fixed temperature at the surface of 273 K.

Both oceanic and cratonic lithosphere have a temperature field based on the half-space cooling (HSC) model:

$$T = T_m \cdot \mathrm{erf}\left(\frac{z}{(2\sqrt{(\kappa t)})}\right) \tag{2.11}$$

Here the oceanic lithosphere was given an age of 50 Ma and the continental lithosphere an age of 250 Ma (Córdoba & Ballmer, 2021).

Equation 2.4 includes an adiabatic heating component. Therefore, in the reference model [Figure 2.2], the initial mantle potential temperature is 1350 K in addition to an adiabatic heating term, which is added to the geotherm:

$$\Delta T_{adiab} = (T_m + T_s)\exp\left(\frac{\alpha g z}{C_P}\right) - T_m \tag{2.12}$$

Where T_m is the internal mantle temperature, T_s is the surface temperature, α is the thermal expansion coefficient, $\boldsymbol{g}$ is the acceleration due to gravity, z is depth and C_P is the specific heat capacity.

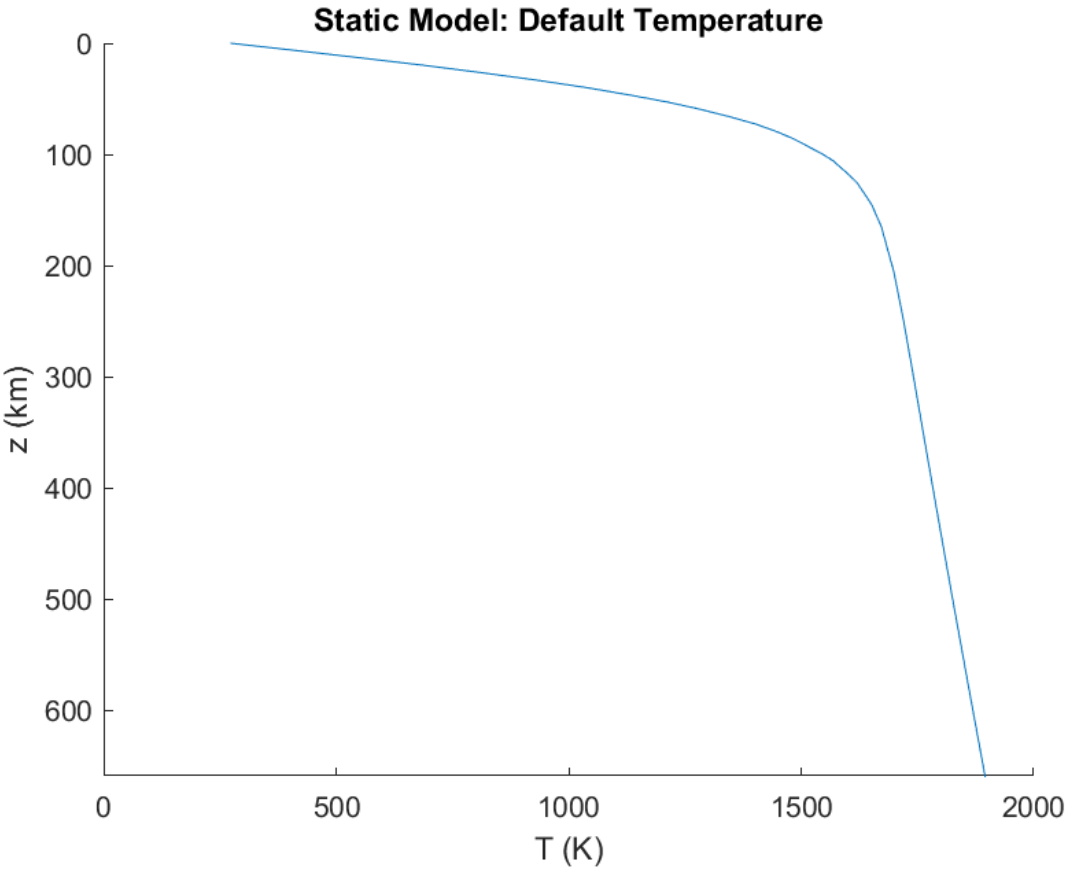

Figure 2.2. The default geotherm profile, resulting from the half-space cooling model and simple adiabatic function, taken through the oceanic lithosphere at timestep zero. These two functions produce the two distinct trends in the geotherm, with the smoothness of the transition between them dictating the ease in which small-scale convection and lithospheric dripping can occur.

2.4 ASPECT & Technical Model Setup

Modelling results are obtained using the community-driven software tool ASPECT (Advanced Solver for Problems in Earth's ConvecTion) version 2.2.0 (Kronbichler *et al.*, 2012; Heister *et al.*, 2017; Bangerth *et al.*, 2020a, 2020b). ASPECT is specifically built to compute equations defined in this chapter using a finite element method (FEM). This software tool is versatile and allows users to investigate a broad range of models, all whilst scaling well with a large number of processors associated with high performance computing (HPC) (e.g. Gassmöller *et al.*, 2016; Heister *et al.*, 2017; Dannberg *et al.*, 2017).

ASPECT can readily calculate a simplified melt fraction using the formulation by Katz *et al.* (2003), but in our models we did not track any resulting depletion or enrichment. As a consequence., accurate melt volumes or a local degree of melting cannot be obtained from these models, and a more qualitive approach was adopted instead using the concentration of fertile material to assess the potential for local intraplate volcanism.

ASPECT allows for sophisticated adaptive mesh refinement [Figure 2.3]. Here, there are two main ways ASPECT can refine: global mesh refinement which is the number of times all the cells in the model are split, e.g. a mesh refinement of 3 would mean a cells are $2^3 = 8$ times more resolved than if the global mesh refinement was not used; adaptive mesh refinement which adds further resolution based on large gradients in user defined parameters, e.g. at increased strain rates, viscosities and temperatures. The adaptive mesh refinement allows for greater resolution where the model is more dynamic, and more coarse resolution in stagnant areas, saving computational power compared to making the whole model as finely resolved. This mesh refinement was used to perform a resolution test for the models (Gassmöller *et al.*, 2018).

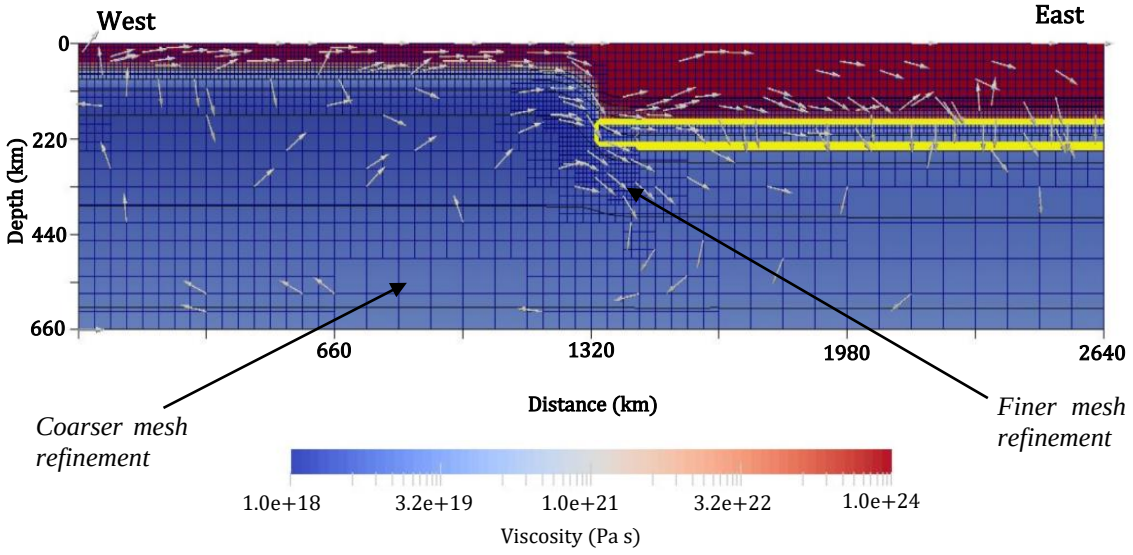

Figure 2.3. The basic lithosphere model with ASPECT-default values, with the model showing mesh size. Where there is a large change in gradient from one of the user specified strategies, the adaptive mesh refinement makes this area more resolved. For example, as there is a large change in strain rate and velocity at the edge of the craton due to a downwelling, the resolution has increased. This process is done at every timestep, giving higher resolution in sections of the model that require it, and lower resolution to more stagnant areas.

Chapter 3

Mantle Dynamics Associated with Intraplate Volcanism: A Parameter Sensitivity Study

3.1 Introduction and Rationale

The aim of this study is to utilise 2D numerical models to explore whether a subcontinental metasomatized layer can explain the occurrence of intraplate volcanism, such as the Cameroon Volcanic Line (CVL). Results of these models are strongly dependent on rheological parameters and as such, a parameter study to investigate the sensitivity of the model dynamics to rheological parameters is conducted. This is followed by an investigation into the nature of convection, metasomatized layer dynamics and the fit the numerical model has to observables.

Constraining the rheology of the upper mantle comes from the compilation of multiple observations. Laboratory studies investigating the effects of pressure on olivine crystals have been used to derive key rheological parameters associated with deformation mechanisms (Hirth & Kohlstedt, 2003; Rutter & Brodie, 2004a, 2004b; Dimanov & Dresen, 2005; Rybacki *et al.*, 2006; Bürgmann & Dresen, 2008). These studies are useful, however there are caveats associated with the extent of pressure exerted on the olivine grains, as well as the length of time under pressure, as typical studies utilise a pressure of 300 MPa, and are relatively short. As such, extrapolation is required to reconcile the observations to those expected in the mantle, with pressures of ~23-25 GPa expected at the 660 km discontinuity (Ishii *et al.*, 2019), and deformation occurring over millions of years. The use of just olivine does not capture the full extent of the mantle composition, with minerals that are only stable at high pressure, like orthopyroxene and wadsleyite (~1 GPa and

~14 GPa respectively (Karato, 1988; Karato, 2010)) not explored. Subsequently, the values presented in these laboratory studies are limited to shallow environments; fail to capture the full extent of mineral diversity, including olivine phase transition and any resulting viscosity change towards greater mantle depths.

Post-glacial rebound (PGR) observations have also been used to determine rheology due to the relationship between the rate of rebound and the viscosity of the mantle. Generally, these studies are in agreement that the viscosity of the upper mantle is on the order of 10^{21} Pa s (Peltier, 1974; Cathles, 1975; Mitrovica & Peltier, 1991a, 1991b; Forte & Mitrovica, 1996; Paulson *et al.,* 2007), with Kaufmann & Lambeck (2000) suggesting a slightly lower value of $2 \times 10^{20} – 5 \times 10^{20}$ Pa s. These studies become more complex once a weak transition zone is considered, as well as large-scale geodynamical processes such as plate subduction, particularly as comparisons to 1D synthetic data shows that PGR resolution is limited to approximately two layers when conducting an inversion for viscosity (Paulson *et al.,* 2007).

Investigations into geoid variation, in conjunction with mantle flow models derived from seismic velocity anomalies can determine relative changes in mantle viscosity, as the geoid is insensitive to absolute viscosity (King, 1995). Results from geoid studies are conflicting, particularly when determining the viscosity of the lower mantle, due to the seismic complexities of lower mantle structures implying compositional heterogeneities, e.g. large low shear velocity provinces (LLSVP) and whether they are purely a thermal anomaly (e.g. Davies *et al.,* 2012) or thermo-chemical (Wen *et al.,* 2001; Ni *et al.,* 2002). Upper mantle viscosities are easier to reconcile, with values between 10^{20} and 10^{21} Pa s (Nakada & Lambeck, 1989; Peltier & Tushingham, 1989; Ricard & Vigny, 1989; Lambeck & Nakada, 1990; Liu & Zhong, 2016; Rudolph *et al.,* 2020).

In this thesis, the rheological values reported by laboratory studies from Hirth & Kohlstedt (2003) are used as a starting point [Figure 3.1], and are adapted based on a parameter sensitivity study to find the best fit with the other observations. From this sensitivity study, a more adequate viscosity profile compared to the one produced when applying values from Hirth & Kohlstedt (2003), can be built, with justification of which set of values may be best for future modelling.

By comparing the viscosity profile when applying ASPECT default values (Hirth & Kohlstedt, 2003) to a set of diffusion and dislocation creep dominant profiles [Figure 3.1], it seems certain parameters need to be altered to produce a more appropriate viscosity. Preferably, a composite viscosity should be comprised of a dislocation creep dominant domain from the lithosphere-asthenosphere boundary (LAB), to ~250 km depth observed via seismic anisotropy (Schubert *et al.*, 2015), with mantle material below this diffusion creep dominant based on laboratory data [see Section 2.2.1]. Figure 3.1 shows the key characteristics that both a diffusion (red) and dislocation (yellow) creep dominant regime possess, which proves useful when trying to distinguish if a profile is composite. In this case the default viscosity profile (blue) produced by using values provided by Hirth & Kohlstedt (2003), follows the diffusion creep curve suggesting the dislocation creep is potentially too strong [Equation 2.7]. This means that instead of being a composite viscosity, the default viscosity profile produced by ASPECT (Hirth & Kohlstedt, 2003) is under a diffusion creep dominant regime, even where dislocation creep is expected to be dominant (Karato & Wu, 1993). The viscosity values at the 660 km discontinuity of the default profile are lower than expected, with the viscosity at this discontinuity suspected to be 1×10^{21} Pa s, as seen in PGR and geoid observations. Based on the parameter sensitivity studies conducted in this chapter, a more appropriate viscosity profile can be created, with a dislocation creep signature from the LAB to ~250 km depth as observed through seismic anisotropy [Figure 3.1].

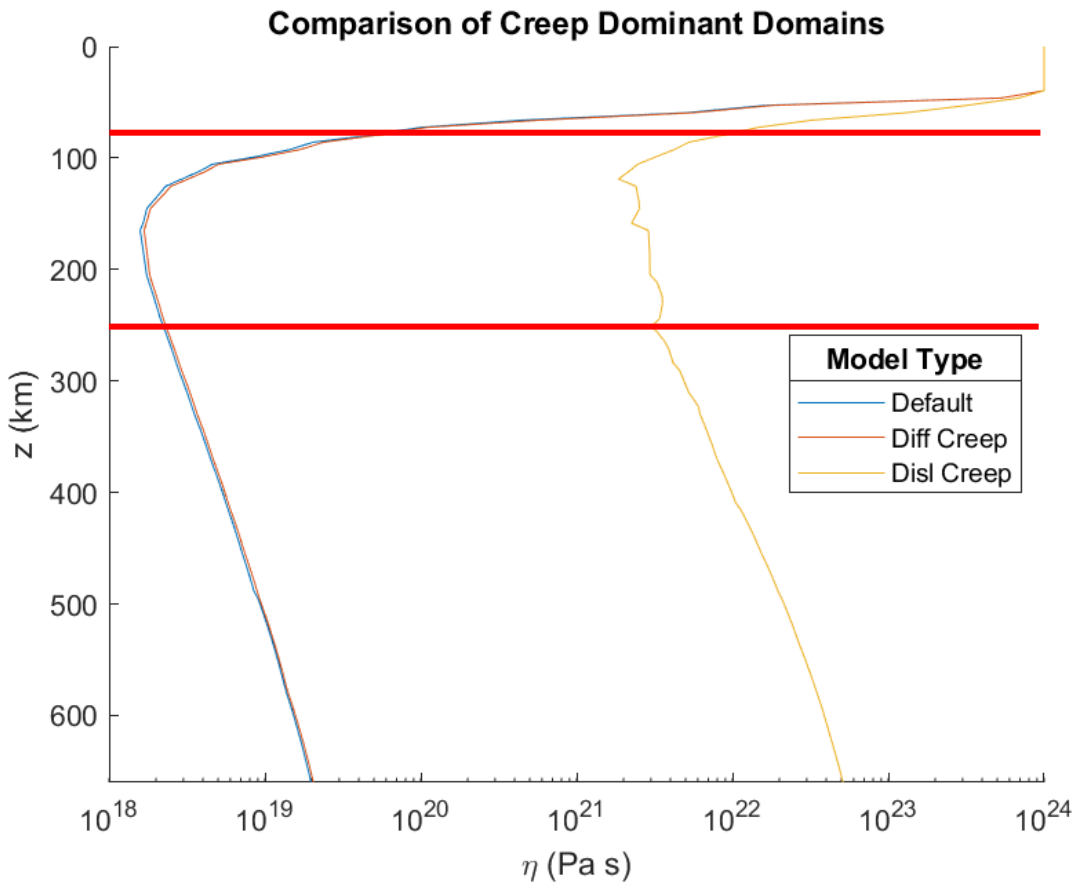

Figure 3.1. A graphical comparison between a diffusion creep dominant regime (labelled 'Diff Creep' and in red), dislocation creep dominant regime (labelled 'Disl Creep' and in yellow) and the default profile (blue). This plot is a useful tool in identifying the different characteristics of each regime which can then be applied in determining whether a viscosity profile is composite. Here the two red lines mark the approximate depth of the lithosphere-asthenosphere boundary and 250 km depth. The diffusion creep dominant profile is a smooth curve through the LAB and continues to the 660 km discontinuity in a linear fashion. The dislocation creep dominant profile begins to fluctuate through the LAB, as it is dependent on the variability of strain rate. Diffusion creep does not share this relationship with strain rate, instead sharing a relationship with grain size, which does not change throughout this model. These plots were produced at t = 0 and run through oceanic lithosphere.

After applying the results of the sensitivity study to produce a preferred model setup, the subcontinental metasomatized layer dynamics are investigated through a 2D numerical model which possesses both static oceanic and cratonic lithospheres (Kaislaniemi & van Hunen, 2014; Córdoba & Ballmer, 2021; Negredo *et al.*, 2022). Success criteria include whether edge-driven convection (EDC) can form and remain long-lived for a period similar or longer than the age of the CVL, with the EDC potentially correlating to the linear shape of the CVL. Whether the subcontinental metasomatized layer behaves in a comparable way to that hypothesized by

Guimarães *et al.* (2020), with the presence of fertile material used as a proxy for increased melt rates [Chapter 2.4]. This is followed by a brief discussion of this chapter's results and the next numerical modelling steps.

3.2 Parameter Sensitivity Study

This sensitivity study looks at factors which potentially have a large impact on viscosity whilst influencing which deformation mechanism is most prevalent, such as the grain size, diffusion creep pre-factor and dislocation creep pre-factor, which are investigated to understand their effect on the effective viscosity profile.

3.2.1 Diffusion Creep Pre-factor

Initially, the default diffusion creep pre-factor assigned in ASPECT (Hirth & Kohlstedt, 2003) was used as a starting point [Table 4]. Dislocation creep is not considered here, so any changes to viscosity directly correlate to the changes in diffusion creep pre-factor. A series of viscosity profiles are taken through the numerical models at timestep 0 and through the oceanic lithosphere [Figure 3.2] The magnitude of the diffusion creep pre-factor is inversely proportional to the change in viscosity, since, with grain size remaining constant and diffusion creep not effected by strain rate, the only influence on viscosity is the pre-factor coefficient, A_i which is inversely proportional to viscosity.

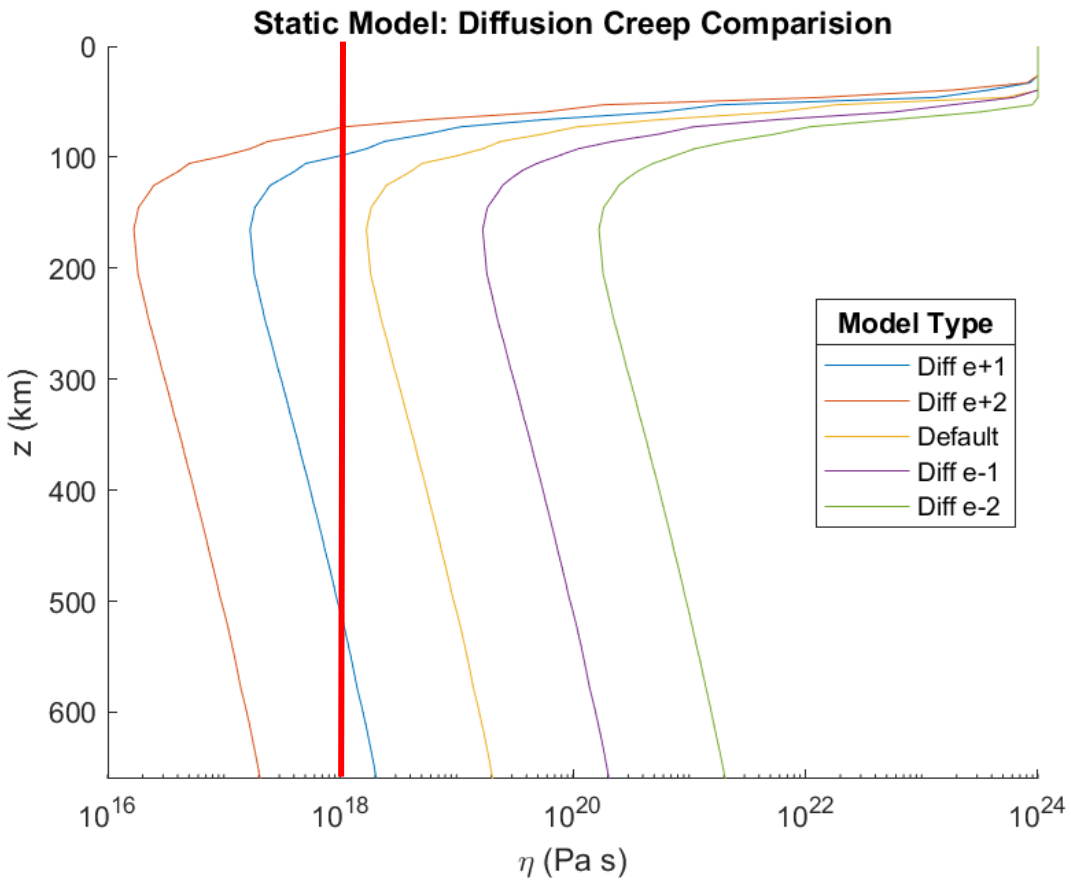

Figure 3.2 shows the five different viscosity profiles produced when altering the order of magnitude of the diffusion creep pre-factor. As diffusion creep is dominant in low stress environments (Karato & Wu, 1993), this is the region of interest. The red line denotes the minimum viscosity used in the models.

3.2.2 Dislocation Creep Pre-factor

Similar to the testing in Section 3.2.1, the dislocation creep pre-factor starts with the default ASPECT value (Hirth & Kohlstedt, 2003) as a median point [Table 4], with subsequent values having a 1 or 2 order of magnitude increase or decrease. Within this section, dislocation creep is the only mechanism influencing the sensitivity results, as diffusion creep is not considered. All five profiles in Figure 3.3 intersect the model through oceanic lithosphere at timestep 0, to give the initial viscosity profile for each test.

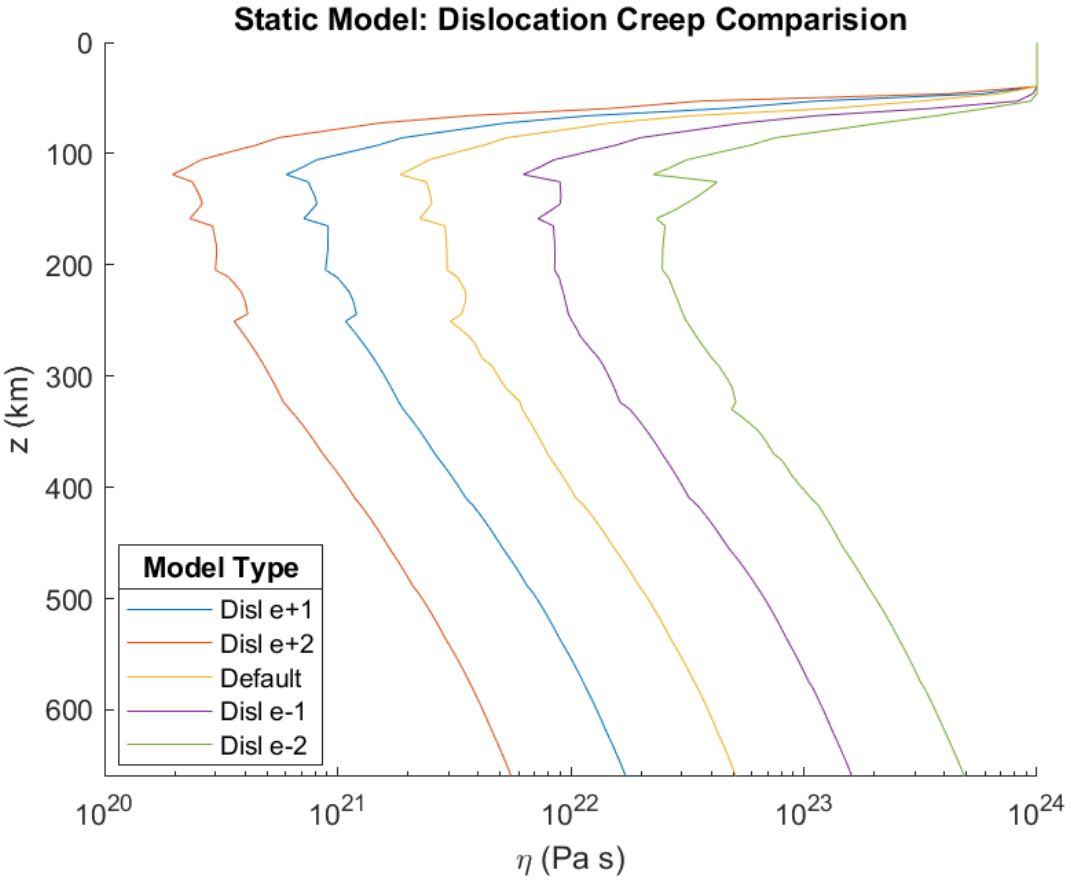

Figure 3.3 shows the five different viscosity profiles produced when altering the order of magnitude of the dislocation creep pre-factor. As dislocation creep is dominant in high stress environments with large strain rates (LAB to 250 km), this is the region of interest. From >100 km depth the viscosity fluctuates, with the increases in dislocation creep pre-factor magnitude displaying these fluctuations over a greater range of depths (100 – 250 km).

By altering the dislocation creep pre-factor by an order of magnitude the viscosity changes by a factor $\frac{1}{n_i}$, which for dislocation creep $n_i = 3$ (e.g. Rybacki & Dresen, 2000; Hirth & Kohlstedt, 2003). However, by altering the dislocation creep pre-factor, strain rates in the models would change, therefore impacting the effective viscosity.

When testing dislocation creep and its effect on viscosity, the patterns in Figure 3.3 are indicative of dislocation creep influences which, as shown through seismic anisotropy observations, cease at ~250 km depth. The profiles were taken at t = 0, which provided the initial viscosity profile of the model, and showed the influence that altering the dislocation creep pre-factor has on viscosity. However, due to low strain rates at this moment, it may not have been adequate to take a value of viscosity here, instead, allowing the model to evolve into a steady-state before measuring the effect

on viscosity. Acknowledging this, it is also fair to mention that these tests on dislocation creep were in a geologically passive region, yet strain rate varies with geological setting. For example, at a subduction zone, the subducting slab would generate high strain rates and so a lower dislocation creep strength is expected, leading to a lower overall viscosity compared to beneath the centre of a large continent. This is also reflected in the depth at which seismic anisotropy is observed in these high strain rate environments (e.g. Wang *et al.*, 2017).

3.2.3 Grain Size

In geodynamical modelling, grain size is a poorly constrained parameter, yet it is highly influential on long-time-scale mantle dynamics (Hall & Parmentier, 2003) and rheology, impacting on diffusion creep strength and thus viscosity (Dannberg *et al.*, 2017). Grain size is assumed to be constant throughout each model calculation, and is tested under a composite regime, where both dislocation and diffusion creep are active. Grain size values were chosen around the ASPECT default grain size of 0.001 m [Figure 3.4].

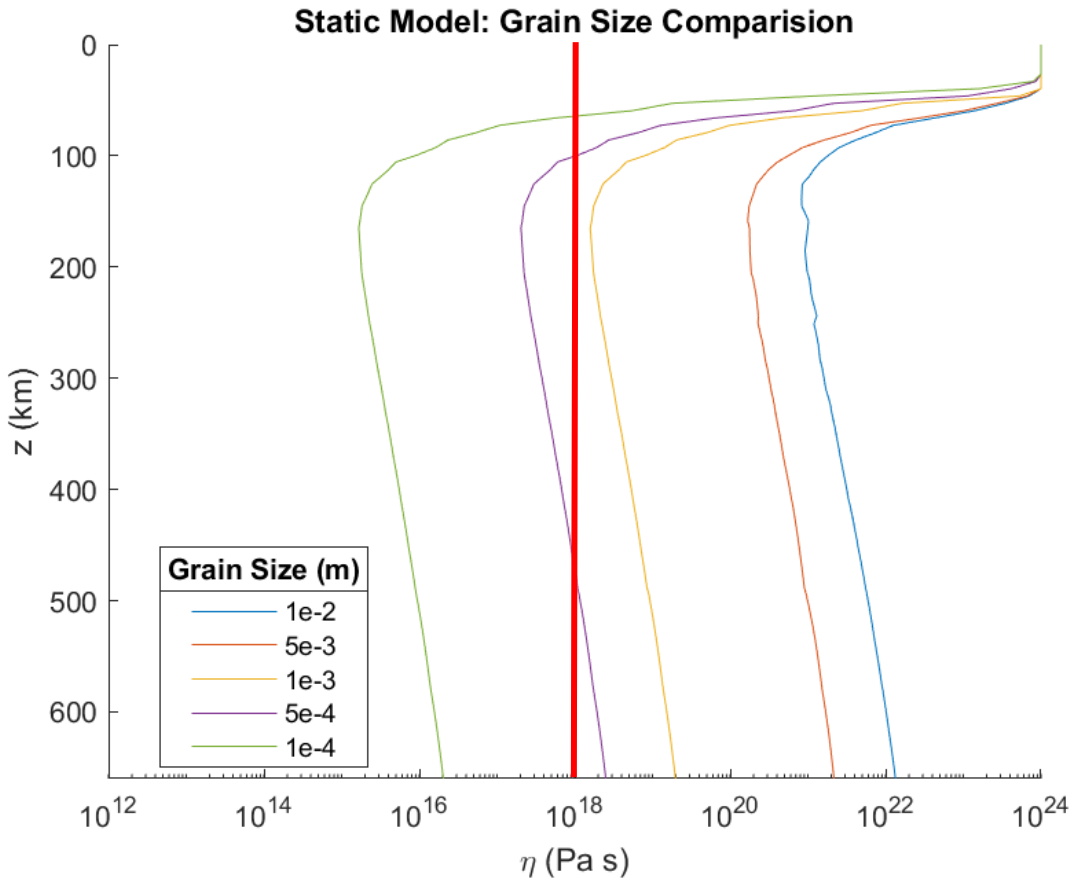

Figure 3.4 displays the five different viscosity-depth profiles produced when altering the values of grain size. Grain size has a large impact on diffusion creep with no influence on dislocation creep and as such, results could be used to influence viscosity with little to no change to creep pre-factors. The red line denotes the minimum value of viscosity emplaced on the models within this thesis, so grain sizes <1e-3 m would require changes in other parameters to provide a suitable viscosity for modelling.

The distribution of the viscosity profiles can be explained as the grain size exponent (m_i [see equation 2.6]) for diffusion creep is 3 (Billen & Hirth, 2007), meaning the viscosity changes by the power 3 for every order of magnitude change in grain size.

Due to the composite nature of the environment, models with larger grain sizes begin to display the fluctuations from the LAB to ~250 km, as seen to a greater extent in the dislocation creep testing. This is due to the relationship grain size has with diffusion creep which is not shared with dislocation creep. As viscosity is determined by the weakest form of deformation, there comes a point when the grain size becomes large enough that diffusion creep is sufficiently strong. As a result, in regions with large strain rates like the LAB, dislocation creep becomes dominant.

Grain size has a large impact on viscosity in diffusion creep dominant regions (e.g. Karato & Wu, 1993), and as such is an important parameter to constrain, however values within geodynamical models are over-simplified, and are poorly constrained. The nature of grain size within the mantle is far more complex, with factors such as the heterogeneity of the mantle, the growth rate of minerals, the depth and phase of grains, as well as the water content of the local mantle having an impact on grain size (Rutter & Brodie, 2004a; Rybacki *et al.,* 2006). So to model grain size as a single value for the entirety of the mantle fails to capture the complexities associated with a parameter which is highly influential in mantle dynamics (Dannberg *et al.,* 2017 and references therein).

3.3 Optimal Viscosity Profiles

From testing within the prior sections, a set of composite viscosity profiles can be produced. In order to match observations from post-glacial rebound (Gasperini & Sabadini, 1989; Forte & Mitrovica, 1996; Paulson *et al.,* 2007) and the dislocation dominance from the LAB to 250 km depths observed through seismic anisotropy (Karato & Wu, 1993; Schubert *et al.,* 2015), the grain size, diffusion and dislocation creep pre-factors are modified to generate viscosity profiles that may fit the data better. Here, altering grain size and the diffusion creep pre-factor both impact the strength of diffusion creep, and although they have the same effect, future models where grain size varies they would be independent. So by testing these parameters separately [Table 4] gives physical insight that may become useful in the future.

Figure 3.5 shows the obtained viscosity profiles developed through altering parameters found in Table 4, and are used in subsequent studies in Chapter 4.

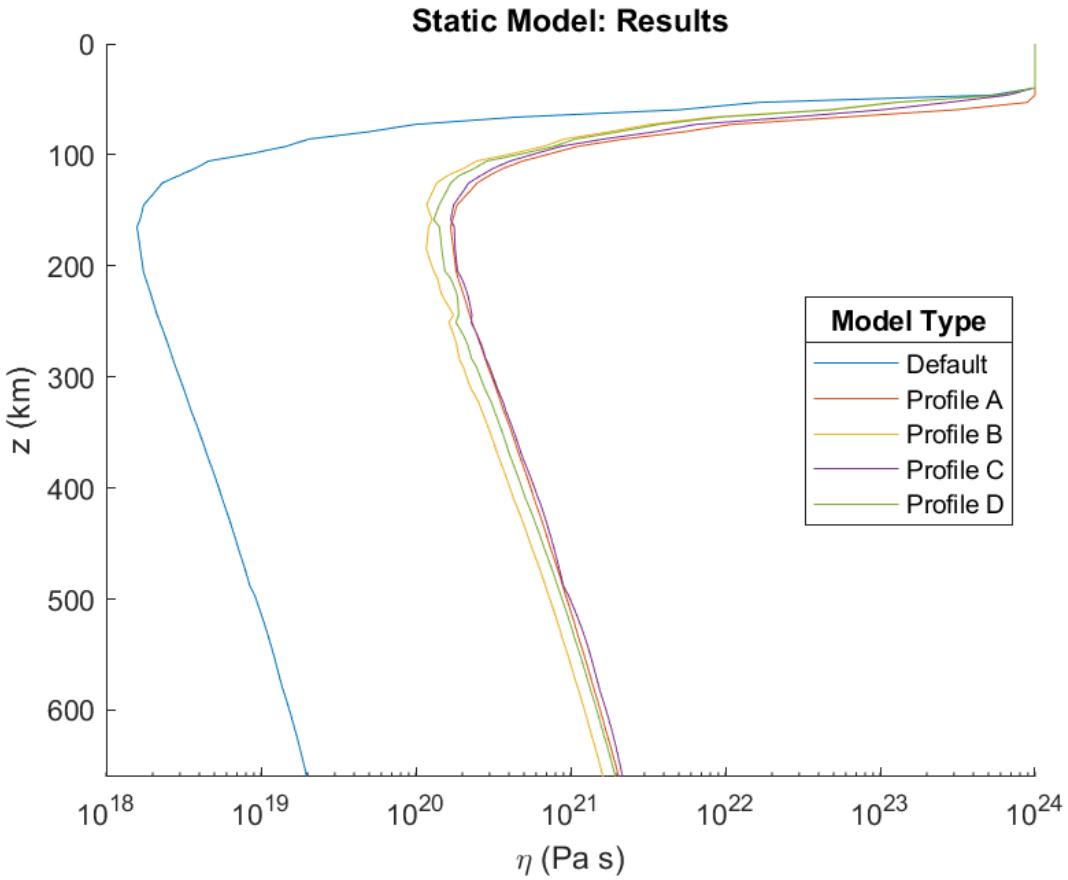

Figure 3.5. Four appropriate viscosity profiles compared to the profile produced by implementing values from ASPECT (Hirth & Kohlstedt, 2003) at t=0 and through oceanic lithosphere [Table 4]. The new models display a viscosity ~ 2 orders of magnitude greater than the default profile, with fluctuations from the LAB to ~250 km, suggesting dislocation creep is active in this domain. This signature is more prominent in the models which weaken the dislocation creep pre-factor by an order of magnitude (profiles B and D).

It must be noted that these are only a sample of adequate viscosity profiles, however it is best not to deviate greatly from the values reported by Hirth & Kohlstedt (2003), as these values have been found through laboratory data. As such, the profiles where only grain size was altered are to be carried forward, due to the variability and uncertainty of the grain size of the mantle, it is more easily justifiable compared to the changes in creep pre-factors made. In doing so, acceptable viscosity profiles are produced within the bounds of realistic values.

Profile	Diffusion creep pre-factor $(Pa^{-1}\ m^{m}\ s^{-1})$	Dislocation creep pre-factor $(Pa^{-n}\ s^{-1})$	Grain Size (m)
Default	1.5×10^{-15}	1.1×10^{-16}	1.0×10^{-3}
A	1.5×10^{-17}	1.1×10^{-16}	1.0×10^{-3}
B	1.5×10^{-17}	1.1×10^{-15}	1.0×10^{-3}
C	1.5×10^{-15}	1.1×10^{-16}	5.0×10^{-3}
D	1.5×10^{-15}	1.1×10^{-15}	5.0×10^{-3}

Table 4 lists the changes in the diffusion creep pre-factor, dislocation creep pre-factor and grain size in each of the five profiles plotted on Figure 3.5.

3.4 Static Lithosphere Numerical Model Results

The viscosity profile presented in the previous section is applied to investigate the mantle dynamics related to the CVL. The investigation into certain observables during the model run include: whether the models can form, develop and sustain edge-driven convection; the behaviour and dynamics of the subcontinental metasomatized layer and whether it correlates with the predictions made by Guimarães *et al.* (2020) and whether general dynamics of the model correlate to other 2D numerical models from literature.

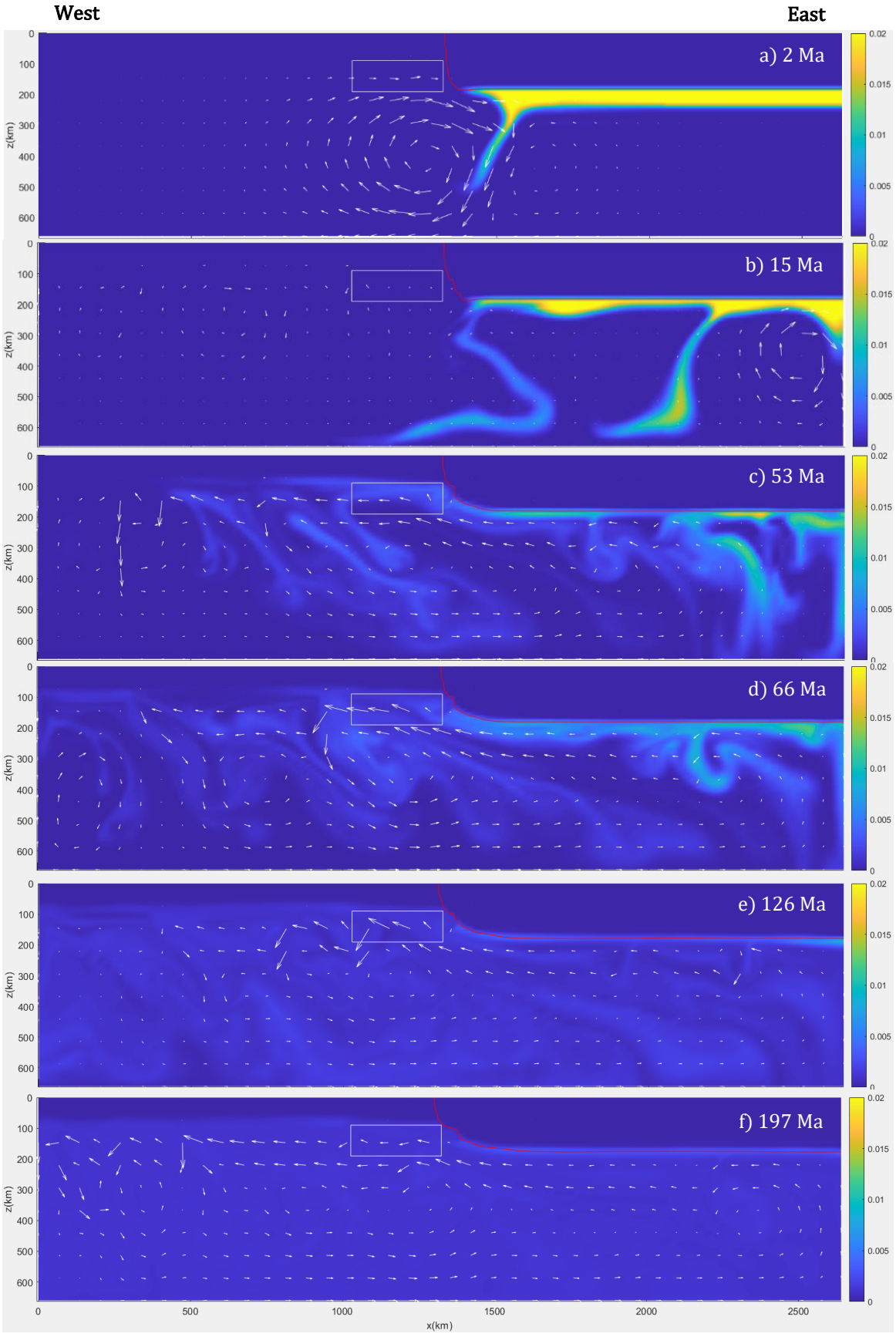
West
East
a) 2 Ma
b) 15 Ma
c) 53 Ma
d) 66 Ma
e) 126 Ma
f) 197 Ma
z(km)
x(km)
0
100
200
300
400
500
600
500
1000
1500
2000
2500
0.02
0.015
0.01
0.005

Figure 3.6 shows the evolution of a 2D static lithosphere model through time, with an initial maximum fertile material fraction of 0.02 (equivalent to 2 volume % - as seen on the colour bar). The outline of the craton is denoted by the red contour, with white arrows representing velocity vectors, and the white box is where metasomatized layer derived melt would originate and, in future models, the fertile material concentration data is collected.

3.4.1 The Evolution of Convective Processes

Initially in Figure 3.6a, a cratonic lithospheric drip allows for the initiation of edge driven convection stricto sensu (EDC_{SS}) bringing material down to the base of the model, where it is subsequently heated becoming more thermally buoyant. Approximately 13 Myr later [Figure 3.6b], the type of edge-driven convection changes from 'stricto sensu' to 'with asthenospheric shear' (EDC_{WS}) [see Section 1.3.3]. This convective pattern evolves to become a large-scale convective feature, with material from below the centre of the craton becoming entrained. In Figure 3.6c, small-scale convection and lithospheric dripping forms from instabilities under mature oceanic lithosphere, aiding mantle mixing.

3.4.2 Metasomatized Layer Dynamics

The metasomatized layer is influenced by the movement of both lithospheric and mantle material, with downwellings from the colder lithosphere dragging large concentrations of fertile material down to the 660 km discontinuity [Figure 3.6b]. In large part, material remains at the transition zone whilst it is heated, with small concentrations being redistributed by convection rolls at shallower depths. At ~50 Myr, the fertile material at the base of the model becomes sufficiently buoyant to rise up under the craton [Figure 3.6c]. Here, the large-scale convective processes pull material along the base of the craton, and up under the oceanic lithosphere, before descending 350-500 km from the edge of the craton. Here the influence of small-scale convection and lithospheric dripping allow the fertile material to continue mixing further from its origin. The continuation of varying convective processes allows for greater mixing and dilution of fertile material in the local upper mantle.

3.5 Static Lithosphere Numerical Model Dynamics: Application and Evolution

The numerical models display dynamic characteristics, such as the formation of EDC, which initially alternated between EDC_{SS} and EDC_{WS} similar to that observed by Negredo *et al.* (2022). This was also observed by Kaislaniemi & van Hunen (2014), although their models show a continuous EDC-type alternation with a periodicity between 14-27 Myr. This may be a feature of them using a continent-continent (proton-tecton) setting, with the lithospheric thickness defined by the tectonothermal ages of the two lithospheric terranes (with the proton a lithospheric terrane characterised by its older than Neoproterozoic age, making it thicker and more viscous than the younger tecton, which typically refers to thinner, younger lithosphere (Janse, 1991; Griffin *et al.*, 2003; Kaislaniemi & van Hunen, 2014)), similar to that observed at the Atlas Mountains (e.g. Missenard & Cadoux, 2012), however this may not be applicable everywhere (e.g. Negredo *et al.*, 2022). Lithospheric instabilities and small-scale convection form drips along mature oceanic lithosphere, and limit the equilibrium thickness of the lithosphere whilst aiding in mantle mixing (Richter, 1973; Richter & Parsons, 1975; Ballmer *et al.*, 2009).

3.5.1 Metasomatized Layer Dynamics and its Correlation to the Cameroon Volcanic Line Geometry

The dynamics of the subcontinental metasomatized layer suggests an initially negative buoyancy, as it sinks to the base of the model. The fertile material remains at the 660 km discontinuity until it is sufficiently hot, where it becomes thermally buoyant, rising under the cratonic lithosphere. This initial behaviour is not consistent with the hypothesis by Guimarães *et al.* (2020), where they propose that the subcontinental metasomatized layer would flow directly from below the craton into the continent-ocean transition (COT), rather than sink to the 660 km discontinuity. The models suggest that after the material is heated at depth, it moves from below the cratonic lithosphere into the COT through the metasomatized layer's buoyancy, as well as large-scale convective processes [Figure 3.6c, 3.6d] similar to the predictions made by Guimarães *et al.* (2020). This suggests that the model setup may require more time in situ to allow for the geotherm to develop as depicted in Figure 1.6. The subcontinental metasomatized layer should be present in the hotter asthenosphere

for a long period of time, to become sufficiently hot and weak to allow for neutral or positive buoyancy before the model begins.

Volcanism through edge-driven convection alone is thought to produce narrow ranges of melt close to the craton (Negredo *et al.*, 2022). Given the lower melting point of the subcontinental fertile material, it is hypothesized that such intraplate volcanism could be produced or aided through drainage of this fertile material. Therefore, we track how this fertile material moves through the white box in Figure 3.6, which we assume will correlate to potential melt generation to build the Cameroon Volcanic Line. It must be noted that the volume percentage of the fertile material within the subcontinental metasomatized layer is poorly constrained.

The first significant arrival of fertile material into the white box in Figure 3.6 was ~40 Myr [Figure 3.7], which correlates well with the delay in volcanism along the Cameroon Volcanic Line after the breakup of Pangea and the opening of the Atlantic Ocean. However, the dynamics of the metasomatized layer within this 2D static lithosphere model does not fit with the hypothesis of Guimarães *et al.* (2020), with material sinking to the 660 km discontinuity [Figure 3.6b]. As this numerical model has no spreading rate imposed, key mantle flows and dynamical processes may

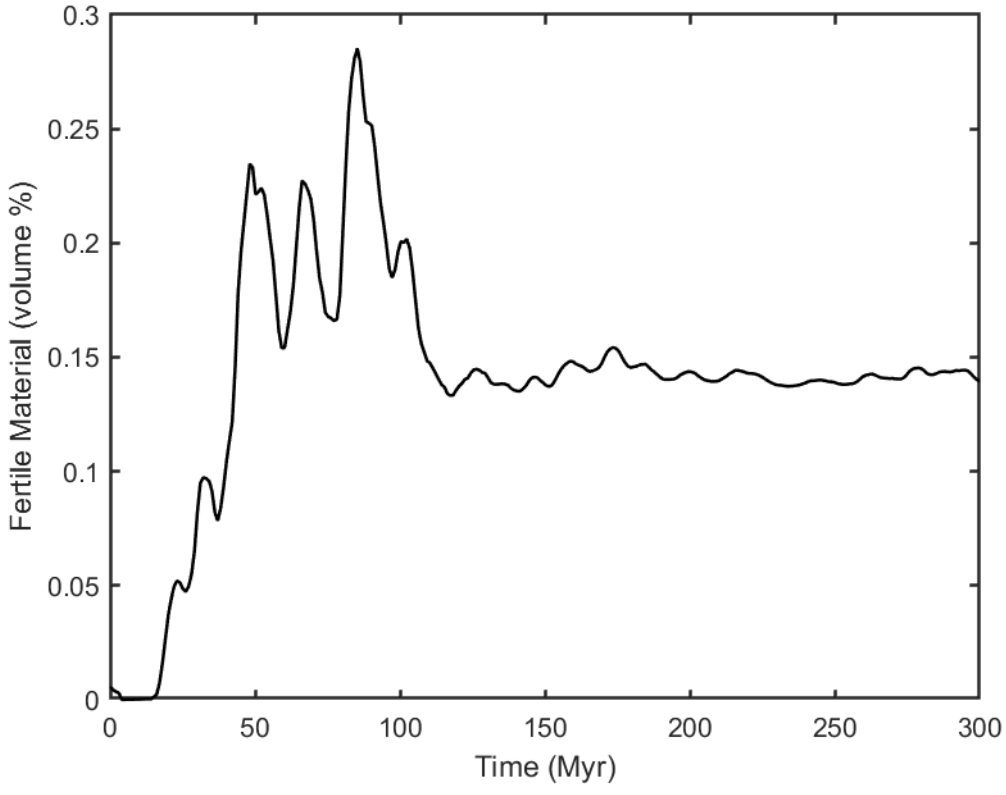

not be taken into account, impacting the rate of fertile material flow into the COT. Subsequently, these dynamics are further investigated in Chapter 4.

Figure 3.7 the concentration of fertile material in the white box at the continent-ocean transition for the static lithosphere model. An increase in fertile material moving into the white box occurs ~40 Myr, which may correlate to the delay in volcanism along the Cameroon Volcanic Line.

3.5.2 Evolution of the Lithospheres

The evolution of the model through time sees both oceanic and cratonic lithospheres change, and it is important to assess whether they remain realistic. The oceanic lithosphere grows in thickness during the model run from 80 km to 126 km, suggesting as the oceanic lithosphere became older, it thickened, but was also affected by lithospheric instabilities to remain realistically thick. The cratonic lithosphere, on the other hand, becomes thinner over time from 180 km to 165 km, due to large lithospheric instabilities and erosion. Unperturbed cratonic lithosphere has been thermally equilibrating for a long time, so is not expected to undergo such significant thinning. However, in the case for the Congo Craton and West African Craton, it could be argued that this thinning is the equilibrising of lithosphere previously thickened by continental collision (e.g. Foley, 2008; Guimarães *et al.*, 2020). It has been observed through numerical modelling that EDC enhances the thinning of cratons as well as smoothening the gradient of the cratonic step, with the strength of the craton playing a critical role in the rate of cratonic lithospheric thinning (Currie & van Wijk, 2016; Liu & Chen, 2019). The strength of a craton is partially impacted by its hydration, with hydrous cratons more readily eroded compared to dry cratons, which can preserve a steep cratonic step for ~100 Ma (Currie & van Wijk, 2016). The Congo Craton was highly metasomatized (e.g. Afonso *et al.*, 2022), however if the development of a subcontinental metasomatized layer, as described by Guimarães *et al.* (2020) is the case under the Congo Craton, then the craton itself would be dry and more resistant to erosion. Due to these different growth rates and erosion the COT between the two lithospheres shallows over time, until EDC ceases.

3.6 Concluding Remarks and Modelling Next Steps

The overall dynamics of the 2D model compare well to other numerical models (e.g. Kaislaniemi & van Hunen, 2014; Córdoba & Ballmer; 2021; Negredo *et al.*, 2022). However, the edge-driven convection within the model did not periodically alternate from EDC_{SS} to EDC_{WS}, an observation made by Kaislaniemi & van Hunen (2014). Instead, there is an initial change from EDC_{SS} to EDC_{WS} with the latter prevailing until EDC ceases (Negredo *et al.*, 2022). This, in conjunction with the large scale convective process, produces a large shearing force through the asthenosphere, which may suppress the formation of convective rolls later in the model (van Hunen *et al.*, 2003; Kaislaniemi & van Hunen, 2014).

The presented model has a weak metasomatized layer at the base of the craton which tends to delaminate and sink to the deep mantle, something which does not fit the hypothesis of Guimarães *et al.* (2020). At the 660 km discontinuity, the material warms until it becomes buoyant and, once sufficiently hot, it behaves as envisaged, mixing in the region where asthenospheric melting would correlate to the formation of the Cameroon Volcanic Line. Typically, crust is expected to sink into the deep mantle, but it may get trapped at the 660 km discontinuity (e.g. van Keken *et al.*, 1996). So, although the subcontinental metasomatized layer does not possess the initial dynamics envisioned, this behaviour is perhaps not completely unrealistic. To investigate further, observables that can distinguish shallow and deep pathways need to be recognised.

Some limitations with this model stem from the fact that the metasomatized layer is highly influenced by mantle flow, and yet this model does not display dynamical effects stemming from oceanic spreading, for example shear-driven upwelling (Conrad *et al.*, 2010; Ballmer *et al.*, 2013). Another key factor that impacts the development of EDC is the geometry of the passive margin, with large thickness gradients and a narrow COT able to produce strong EDC (Córdoba & Ballmer, 2021; Negredo *et al.*, 2022). To further investigate the effects these environmental parameters have, a more dynamic, self-consistent model with a spreading ocean may resolve this, which is addressed in the next chapter.

Chapter 4

Mantle Dynamics During the Opening of an Ocean

4.1 Ocean Opening Models

The mechanism underpinning the origin and formation of the Cameroon Volcanic Line (CVL) is still unknown. It does not display an age progression (Fitton & Dunlop, 1985), its geochemistry suggests an asthenospheric origin rather than a deep-seated origin associated with mantle plumes, and its formation occurs contemporaneously with another volcanic chain of NE Brazil, which possesses indistinguishable geochemistry, while being separated by a spreading Atlantic Ocean (Guimarães *et al.*, 2020). A commonly proposed mechanism to explain the volcanism is edge-driven convection (EDC), but for that to work, an increase in mantle temperatures or volatile concentration is required to produce substantial volumes of melt (Kaislaniemi & van Hunen, 2014; Negredo *et al.*, 2022). Here, we aim to investigate the dynamics of a hypothesized subcontinental metasomatized layer, resulting from long-lived metasomatism under cratons which undergo continental collision and thermal equilibration, subjecting the material to greater temperatures and making the metasomatized material hot, weak and mobile.

Most previous EDC research utilises a 2D static lithosphere model (e.g. Kaislaniemi & van Hunen, 2014; Córdoba & Ballmer, 2021; Negredo *et al.*, 2022), but this does not capture the dynamical evolution of the mantle as oceanic lithosphere forms. Alternatively, a model simulating ocean opening would provide a more dynamic picture of the interaction between oceanic lithosphere and EDC. Such a model would consist of the initiation of ocean spreading beside a slab of cratonic lithosphere, spreading at a constant velocity. During this model, a natural continent-ocean transition (COT) would form following the evolution of oceanic lithosphere adjacent to the craton. The processes of spreading would induce a potentially important mantle flow which would influence

mantle convection, alongside the process of shear-driven upwelling (SDU), which would provide a natural source of upwelling at the edge of the craton and assist in fertile material drainage (Conrad *et al.,* 2010; Ballmer *et al.,* 2013).

The aim of this chapter is to use a new ocean opening model to investigate the impact that ocean spreading has on the development of EDC and the dynamics of the metasomatized metasomatized layer, which is situated directly below the craton (Guimarães *et al.,* 2020). This is done by conducting a parameter sensitivity study which aims to test the effect of changing non-rheological parameters: the half-rate spreading velocity, the compositional positioning of the metasomatized layer relative to the craton and the density of the fertile material. These parameters specifically test the fertile material mobility, and its ability to drain into the COT over a period of 40 Myr as hypothesized by Guimarães *et al.* (2020).

4.2 Model Setup

The ocean spreading model builds and adapts from models in Chapter 3, utilising the same physical governing equations as described in Chapter 2. The default model dimensions in these new models have been changed, from 660 x 2640 km for the static lithosphere models in Chapter 3, to a 660 x 4620 km model to allow for the movement of material whilst spreading [Figure 4.1]. In some of the presented models, the dimensions are altered to allow internally consistent testing of influence of the half-spreading rate, as is described in Section 4.3.2. The thermal evolution of the models within this chapter differs from the static lithosphere model in Chapter 3. An initial continental geotherm is imposed across the entire model domain, with a surface temperature of 273K and a mantle potential temperature of 1350+273 K, in addition to the adiabatic component $\exp\left(\frac{\alpha g z}{C_P}\right)$ in Equation 2.12. To simulate the development of a thermal steady state during a supercontinent period before the ocean opening, a 100 Myr delay on spreading is emplaced, to allow the model to evolve into a natural steady-state (Sleep, 2007; Kaislaniemi & van Hunen, 2014; Negredo *et al.*, 2022). After this supercontinent period, ocean spreading is simulated, and as oceanic lithosphere forms at the mid-ocean ridge (MOR), it self-consistently develops an oceanic geotherm and a natural step in lithospheric thickness at the continent-ocean transition.

Similar to the model used in Chapter 3, there is a lack of a self-consistent depletion model, therefore models in this chapter do not directly allow for investigating the development of any melt [Section 2.4]. Instead, a simplifying assumption is made that with a higher concentration of the initially subcontinental fertile material, a larger degree of melting is expected.

Ocean spreading is modelled by imposing a fixed half-spreading rate at the top surface, and symmetry boundary conditions ($\frac{dT}{dx} = 0$ and free-slip flow) on the left-hand side boundary to simulate a MOR. The right-hand side boundary has a fixed, continental geotherm, and a free horizontal flow boundary condition imposed ($v_z = 0, \frac{dv_x}{dx} = 0$) [Figure 4.1]. Once the 100 Myr delay is complete, a constant default velocity of 2 cm/yr is imposed on the top boundary [Table 5], moving the craton from left to right, with the bottom boundary possessing a free-slip flow boundary condition and an imposed potential temperature of 1350+273 K, in addition to the adiabatic component $\exp\left(\frac{\alpha g z}{C_P}\right)$ in Equation 2.12. The compositional model of the reference metasomatized layer, craton and mantle material are the same as those described in Chapter 2 [Table 4]. An important element to model is the maturation of the artificial geotherm, as the development of lithospheric instabilities depends strongly on the thermal structure of the lithosphere (van Hunen *et al.*, 2005; Kaislaniemi *et al.*, 2014).

The models within this chapter are comprised of 3 compositionally distinct layers: a cratonic lithosphere 180 km thick; the mantle material below all other layers and the derivative of the oceanic lithosphere; the subcontinental metasomatized layer located directly below the base of the craton and 50 km in thickness [Figure 4.1], with its composition derived from mantle material and a more fusible material in a ratio 95:5. Within the models, a white box is used as a visual aid to show where the collection of fertile material concentration data takes place. This box is 300 x 100 km, situated at 100 km depth and directly beside the craton edge as this is where EDC-derived melt would occur; for fertile material to have an impact on melt generation, it has to be in this region (e.g. Negredo *et al.*, 2022).

Due to the recondite nature of the hypothesized metasomatized fertile layer at the base of the continental lithosphere, we test a range of model parameters to see which play an important role in its dynamical behaviour. In particular, three key parameters are tested: the density of the subcontinental fertile material, the velocity of the half-spreading rate and the position of the subcontinental metasomatized layer relative to the compositional base of the craton. The fertile material ranges from a 200-1200 kg m^{-3} relative density decrease compared to the mantle material (noting that this fertile material makes up 5% of the overall metasomatized layer, with the mantle material making up the remaining 95%). The half-spreading rates between 2-5 cm/yr are investigated to explore potential dynamical phenomenon and their influence on fertile material drainage, as well as EDC formation. The relative position of the metasomatized layer, and hence the extent to which it is embedded into the lithosphere above, will likely affect mobility of fertile material. Models test metasomatized layer positions from fully within the (compositionally strong) craton to 50 km below the base of the craton and fully within the mantle.

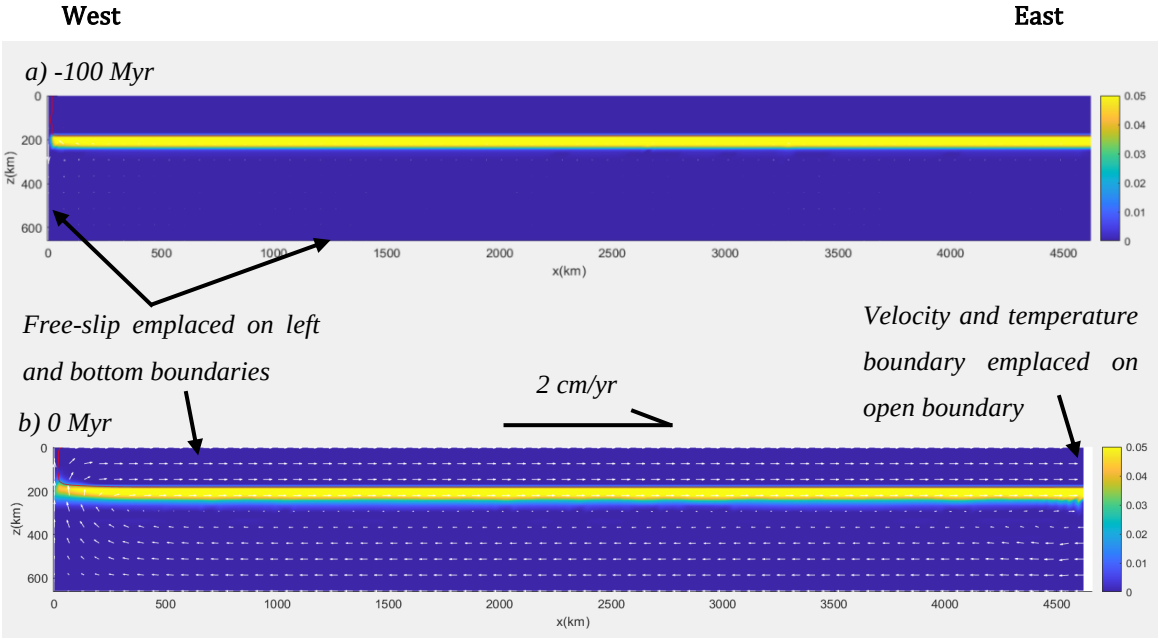

Figure 4.1. The initial model and its thermal evolution over a period of 100 Myr, allowing the artificial geotherm to mature. Here t=-100 Myr denotes the start of the model delay, where it sits in situ and t=0 is the start of the 2 cm/yr ocean spreading imposed on the top boundary, moving from left to right. Herein t=0 will be the starting point of subsequent models in the forthcoming Chapters. The craton boundary is marked by a red contour, the velocity vectors are denoted by white arrows and the metasomatized layer is scaled via the colour plot which shows the fertile material fraction.

4.3 Ocean Opening Reference Model Results

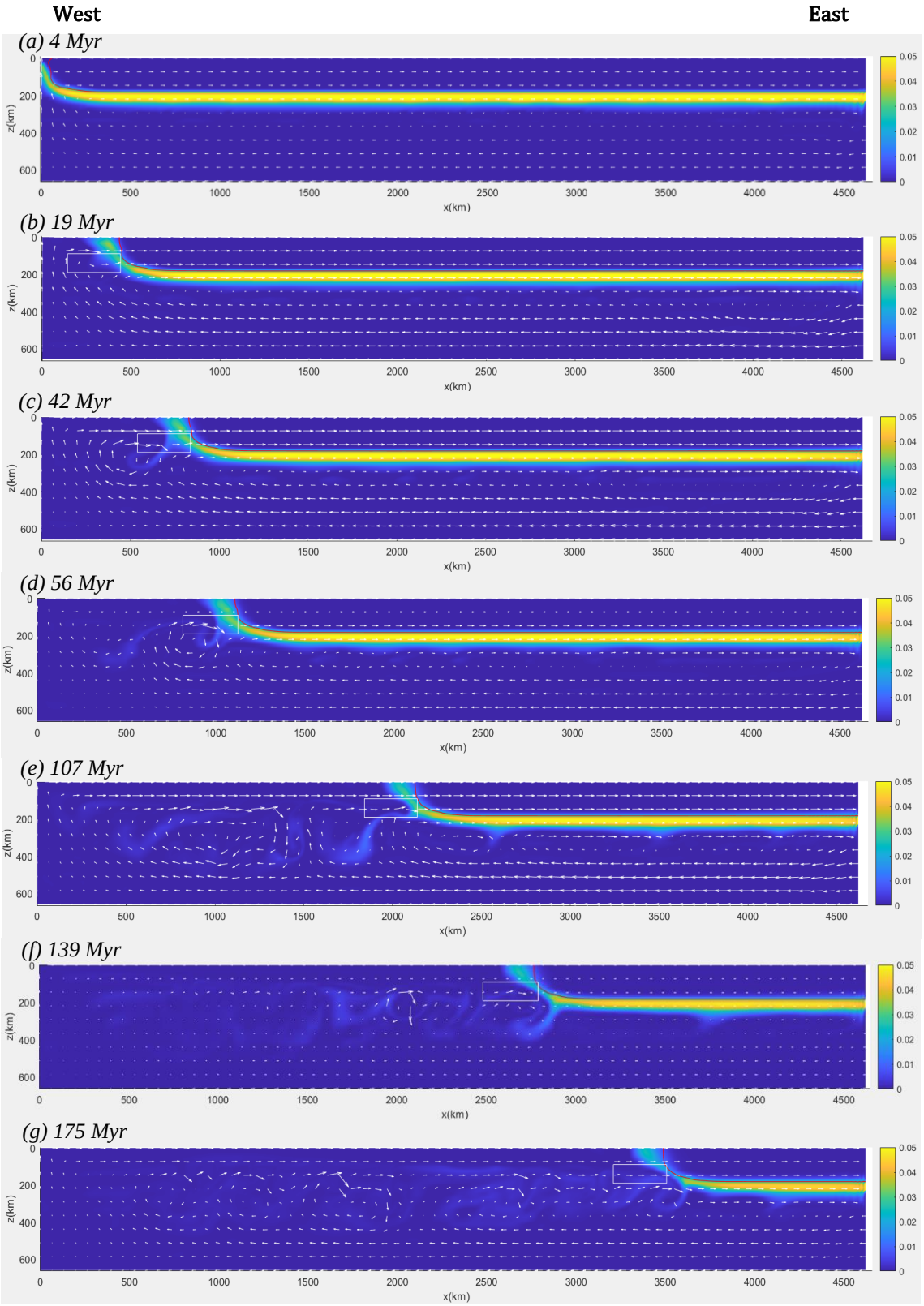

Figure 4.2. The reference ocean opening model using the default values in Table 5. Subcontinental fertile material moves into the white box, which is where the concentration data will be collected for future figures in this chapter. The craton (red contour) is moving from left to right, with the left

hand side simulating a mid-ocean ridge spreading centre. The colour-plot denotes fertile material concentration, and the white arrows denote velocity vectors.

Parameter	Default Value	Value Range
Half-spreading rate [cm/yr]	2.0	$2.0 - 5.0$
Relative compositional position of metasomatized layer [km]	0.0	$-50.0 - 50.0$
Density of fertile material relative to mantle [kg m^{-3}]	-600	$-1200 - -200$

Table 5. The default values used in Figure 4.2, as well as the range of values used in the non-rheological testing throughout Chapter 4.

4.3.1 Density of the Fertile Material

Geochemically, it has been suggested that metasomatized material in cratons is derived from carbonate-rich metasomatism (Menzies *et al.*, 1987; Tappe *et al.*, 2017; Guimarães *et al.*, 2020; Groves & Santosh, 2021) which suggests the fertile material to be close to 2800 kg m^{-3} in density. This value is used as a starting point with densities of fertile material ranging from 2200-3200 kg m^{-3} with testing of values at intervals of 200 kg m^{-3}, due to the uncertainty of the material's composition, and therefore its density. The other non-rheological parameters are set to their default values [Table 5]. Figure 4.3 shows the two end members of the study, as well as the initial density correlating to a carbonate-rich metasomatized layer.

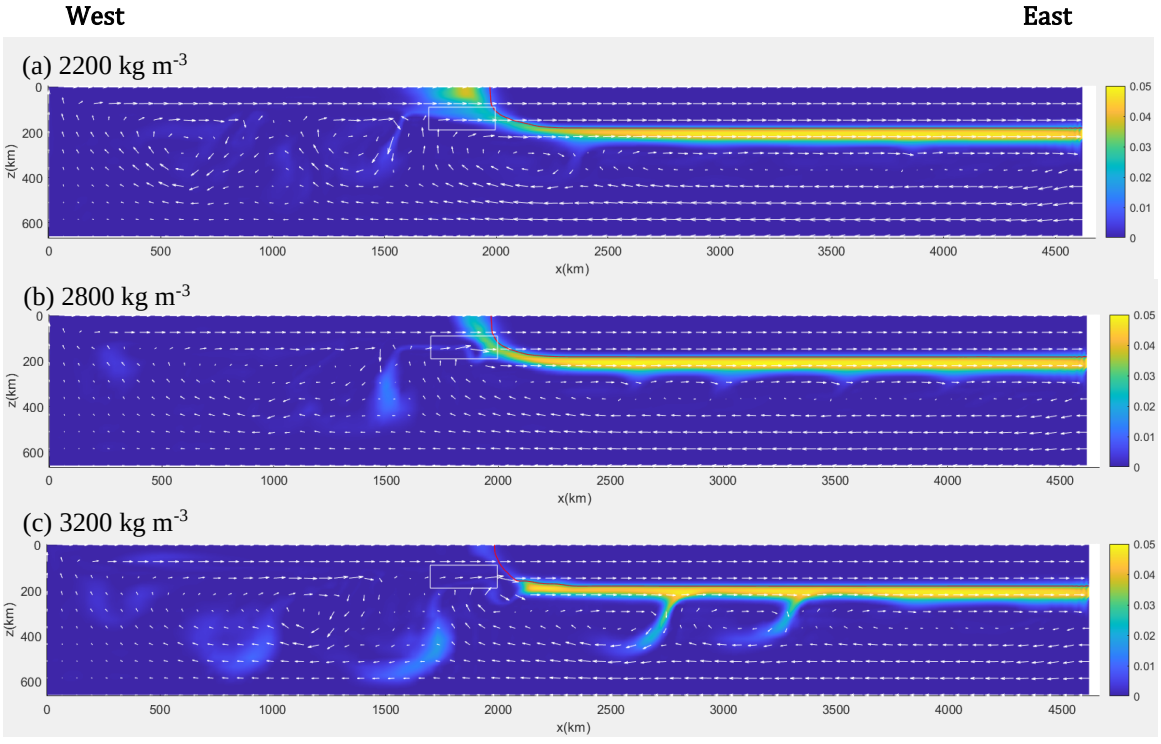

Figure 4.3 shows the fraction of fertile material with a density of a) 2200, b) 2800 and c) 3200 kg m^{-3}. All models within this figure are taken at t=100 Myr, with the red contour denoting the craton edge, the white arrows representing velocity vectors and the 300 x 100 km white box tracks the concentration of fertile material.

By observing the concentration of fertile material at the continent-ocean transition (COT) at 100-200 km depth over time, both fertile dynamics and potential influences on edge-driven convection derived melt can be inferred. More fertile material moves up the craton edge and into the thinner lithosphere for fertile material densities of <2800 kg m^{-3}. In comparison, the densest material fails to move up into the COT. Instead, lithospheric dripping from the base of the craton drags material into the mantle, which is slowly mixed via convection.

By collecting fertile material concentration over time for each density tested [Figure 4.3], a more qualtative comparison of metasomatized layer dynamics can be inferred, and can be used to determine the range of densities that is more favourable to the dynamics proposed by Guimarães *et al.* (2020).

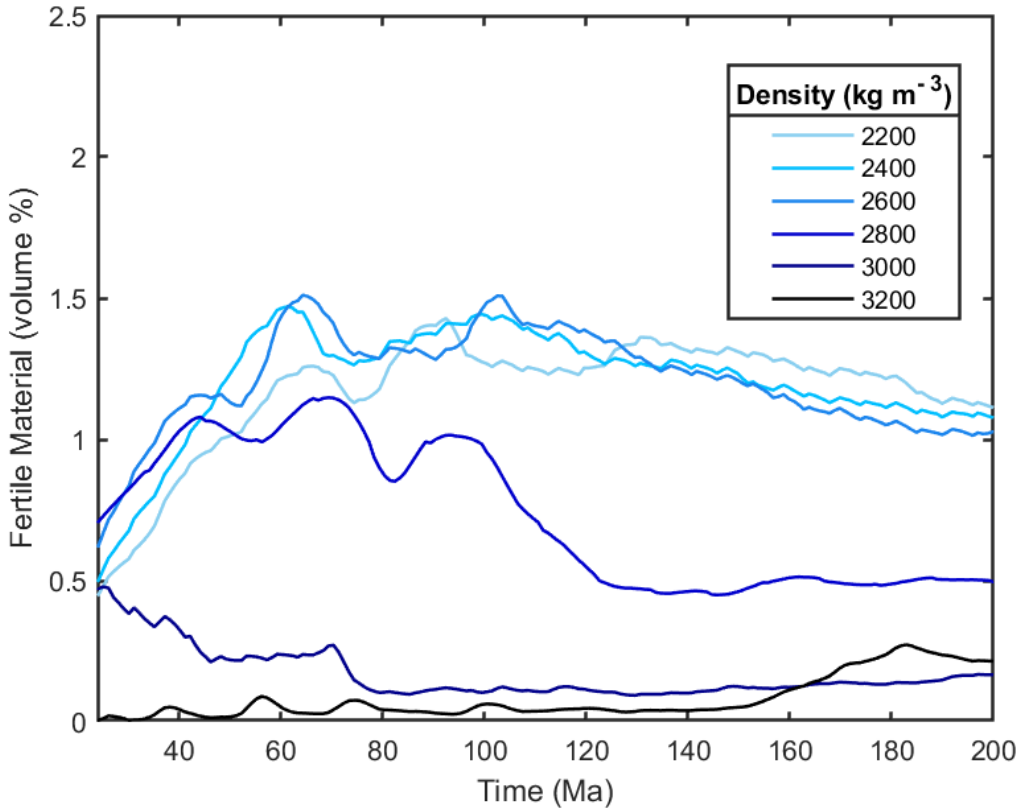

Figure 4.4 is the average volume percentage of fertile material in the data box (white box in Figure 4.2) through time, for different densities of the fertile material from 2200 kg m^{-3} to 3200 kg m^{-3} in intervals of 200

kg m^{-3}, which equates to a 10 kg m^{-3} change in the bulk metasomatized layer density. Lighter shades of blue denote lighter densities, with darker shades correlating to greater densities.

If the fertile material is denser than 3000 kg m^{-3}, the concentration of fertile material doesn't increase to a value >0.5 volume %. Conversely, the models with fertile material densities ≤2600 kg m^{-3} experience increasing concentrations of fertile material for ~40 Myr, before remaining relatively constant between 1-1.5 volume % for the rest of the model run. The density associated with carbonates, 2800 kg m^{-3}, is a combination of these two density ranges, with an increase in fertile material concentration in the first 40 Myr. However, instead of remaining constant, the concentration fluctuates until ~100 Ma, when the concentration drops steadily from 1 volume % to 0.5 volume % over a period of 20 Myr. After that, the concentration remains constant until the end of the model run.

Throughout the thesis, two forms of density measurement are used: fertile material density, which is the density given to the more fusible elements of the metasomatized layer, and bulk metasomatized layer density, which is the density of the metasomatized layer, including the 95% mantle material and the 5% fertile material. For example, a 200 kg m^{-3} change in fertile material density would equate to a 10 kg m^{-3} change in bulk metasomatized layer density.

4.3.2 Oceanic Spreading Rate

The rate of oceanic spreading can play a large role in asthenosphere dynamics by generating shearing forces (Conrad *et al.,* 2010; Bianco *et al.,* 2011; Ballmer *et al.,* 2013). This section will investigate the impact different velocities of spreading rate has on the formation of EDC, as well as the effects it has on metasomatized layer dynamics. The velocity of half-spreading rate varies greatly in location and time (Müller *et al.,* 2008), so for simplicity, a range of constant velocities from 2-5 cm/yr were chosen, to provide a sufficient range of real-world values.

The density of the fertile material for all the velocity models was set to 2800 kg m^{-3}, as suggested for carbonate-rich metasomatized material [Table 5] (Menzies *et al.,* 1987; Tappe *et al.,* 2017; Guimarães *et al.,* 2020; Groves & Santosh, 2021). Due to the changes in velocity, a change in model box width is also required, to allow ample space for the craton edge to remain within the model

box: the models testing velocity have an increase width from 4620 km to 10560 km, providing a new aspect ratio of 16:1 [Figure 4.5].

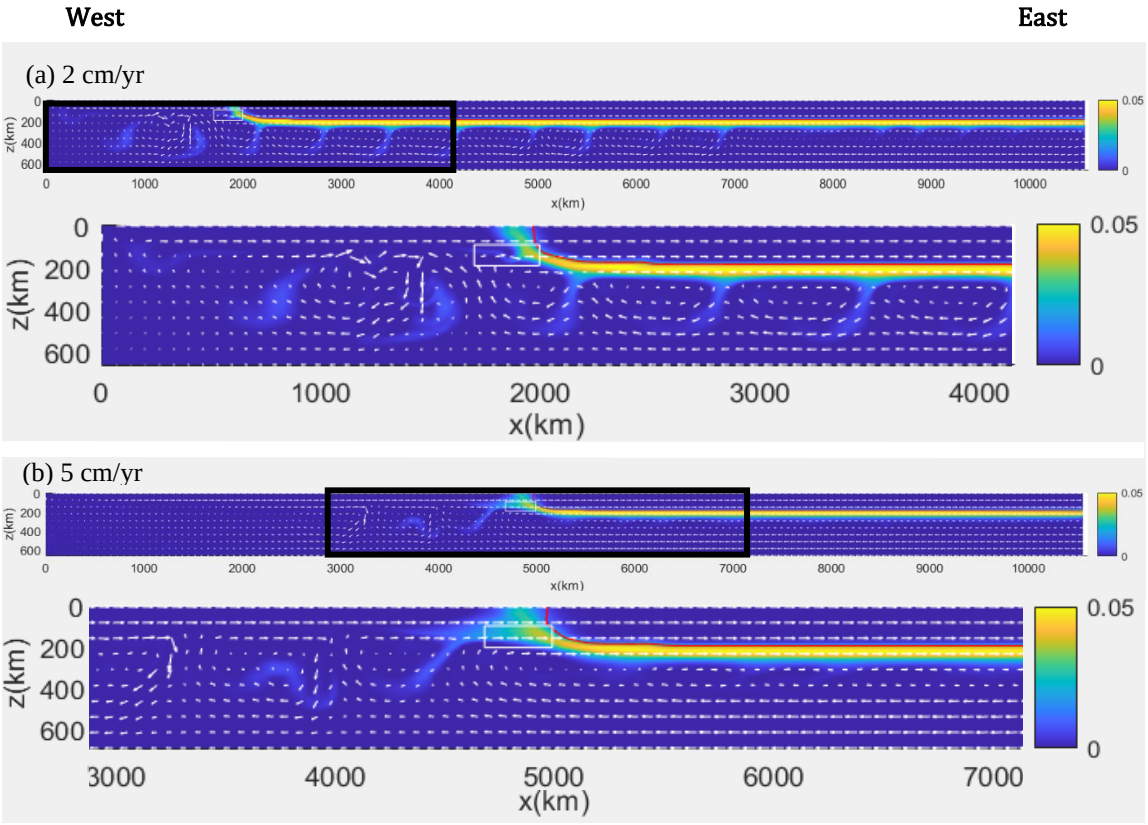

Figure 4.5 shows the fertile material concentration of the two end members of the half-spreading rate tests, 2 cm/yr and 5 cm/yr (a and b, respectively) at t=100 Myr. Due to the increased aspect ratio, there is a zoomed-in domain centred around the continent-ocean transition (COT), as the velocity of spreading differs. This domain is denoted by the black box on the full-width figure and is ~4000 x 660 km. Data shown in Figure 4.6 is collected from the white box at the COT. The red contour denotes the edge of the craton, the white arrows the velocity vectors, and the colour plot is the concentration of fertile material.

The slower velocity shows the fertile material being dragged down by lithospheric drips at the base of the craton, whilst the faster velocity models lack any cratonic lithospheric dripping, with the metasomatized layer staying coherent at the base of the continental lithosphere [Figure 4.5].

By investigating the fertile material within the white box over time, the effects of half-spreading rate on the asthenosphere and the metasomatized layer can be quantified [Figure 4.6].

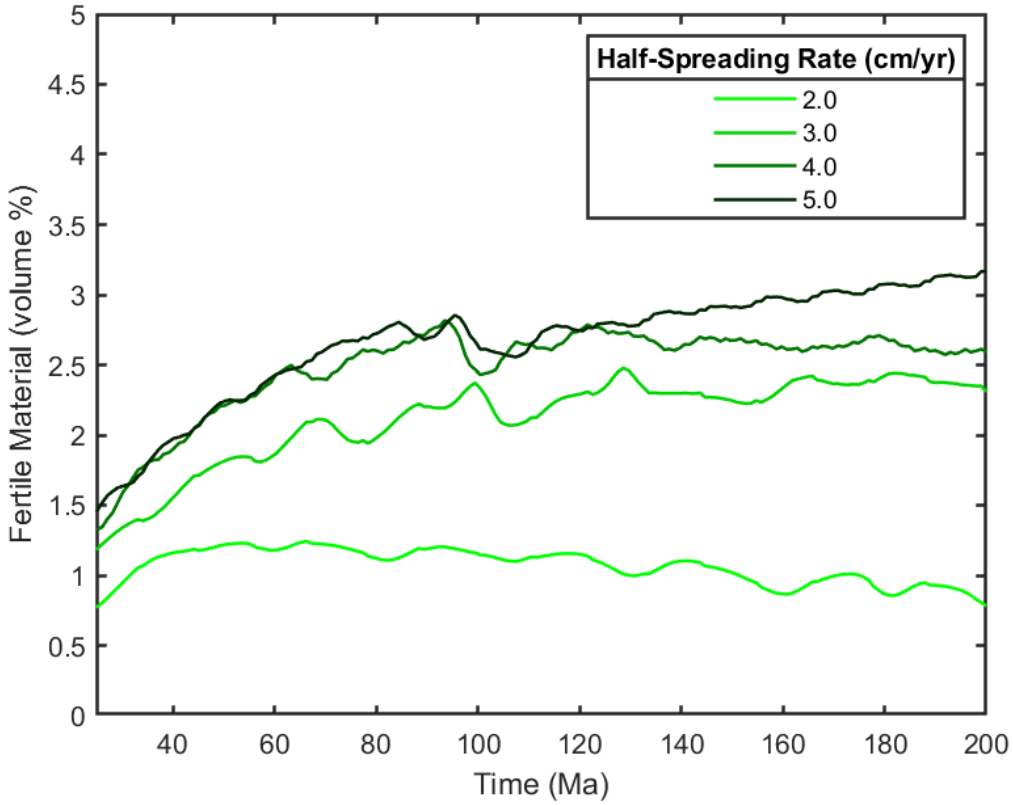

Figure 4.6 shows the concentration of fertile material in the white box at the continent-ocean transition for models of different half-spreading rate velocities ranging from 2-5 cm/yr, with increments of 1 cm/yr.

Higher half-spreading rates lead to greater concentrations of fertile material present at the COT. Velocities >2 cm/yr provide a steady increase in fertile material through time, with rates slowing or becoming constant after 100 Myr. Initially, velocities of 4 cm/yr and 5 cm/yr are very similar, however, the faster velocity continues its increase in fertile material to ~3.2 volume %, whilst the 4 cm/yr model remains at a constant ~2.5 volume % from 120-200 Myr. The slowest velocity of 2 cm/yr had an initially very small increase in fertile material, which becomes a fluctuating decline resulting in the same initial value 200 Myr later.

4.3.3 Relative Compositional Position of the Metasomatized Layer

The depth of the hypothesized subcontinental metasomatized layer relative to the thermal or compositional base of the lithosphere is poorly constrained. Whether the metasomatized layer is positioned within the cratonic mantle lithosphere, asthenospheric mantle or a combination of the two, can have implications on its mobility. The default position of the metasomatized layer in all previous models has been directly below the craton, starting at 180 km, which coincides with the

cratonic compositional base. In this section, the depth of this layer is defined as relative to this compositional base of the lithosphere. For example, in Figure 4.7, '0 km' (the default position in the other models) relates to the top of the metasomatized layer starting at the base of the cratonic lithosphere, so that the relative distance between these two depths is 0 km.

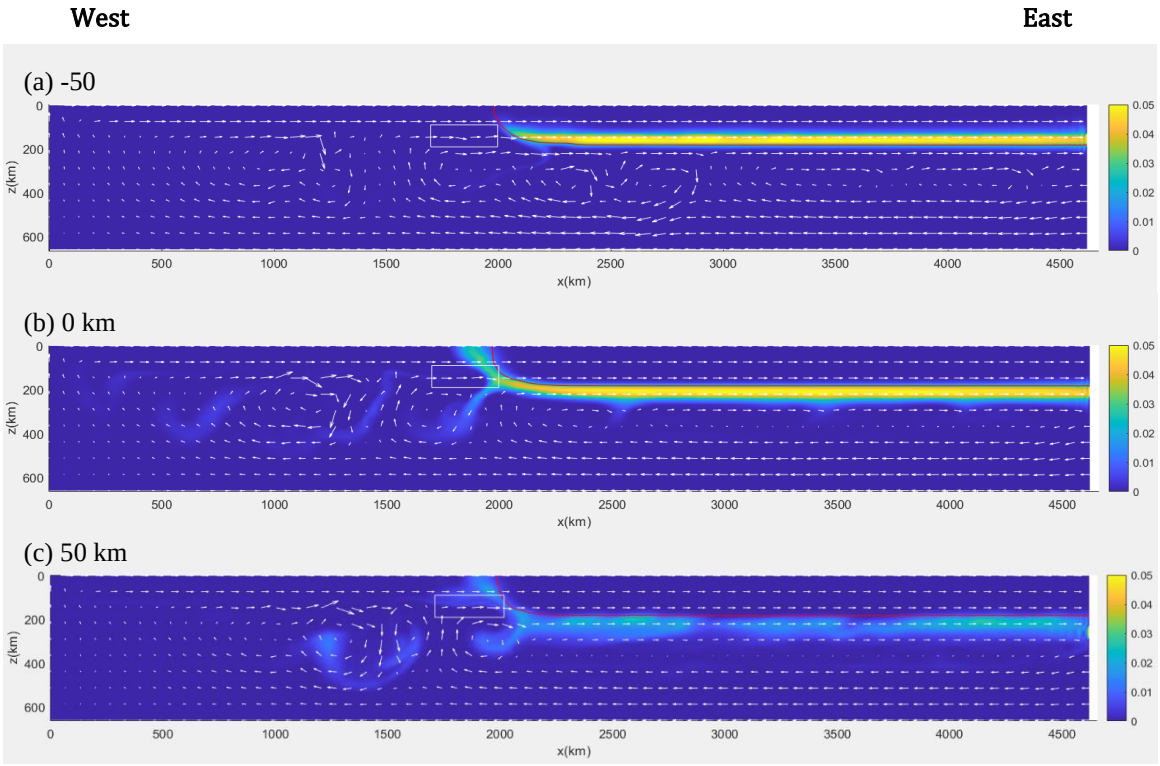

Figure 4.7 shows the default (b) relative compositional position, with the metasomatized layer beginning immediately below the craton; the two end members (a and c), with the metasomatized layer contained fully within the craton, and 50 km below the base of the cratonic lithosphere respectively. The models within this figure were taken at t=100 Myr. The white box is where fertile material data is taken, the red contour denotes the craton edge, and the white arrows display the velocity vectors.

The mobility of the metasomatized layer is strongly influenced by its position in relation to the craton, with greater concentrations of fertile material able to drain into the thinner lithosphere if the layer is positioned deeper.

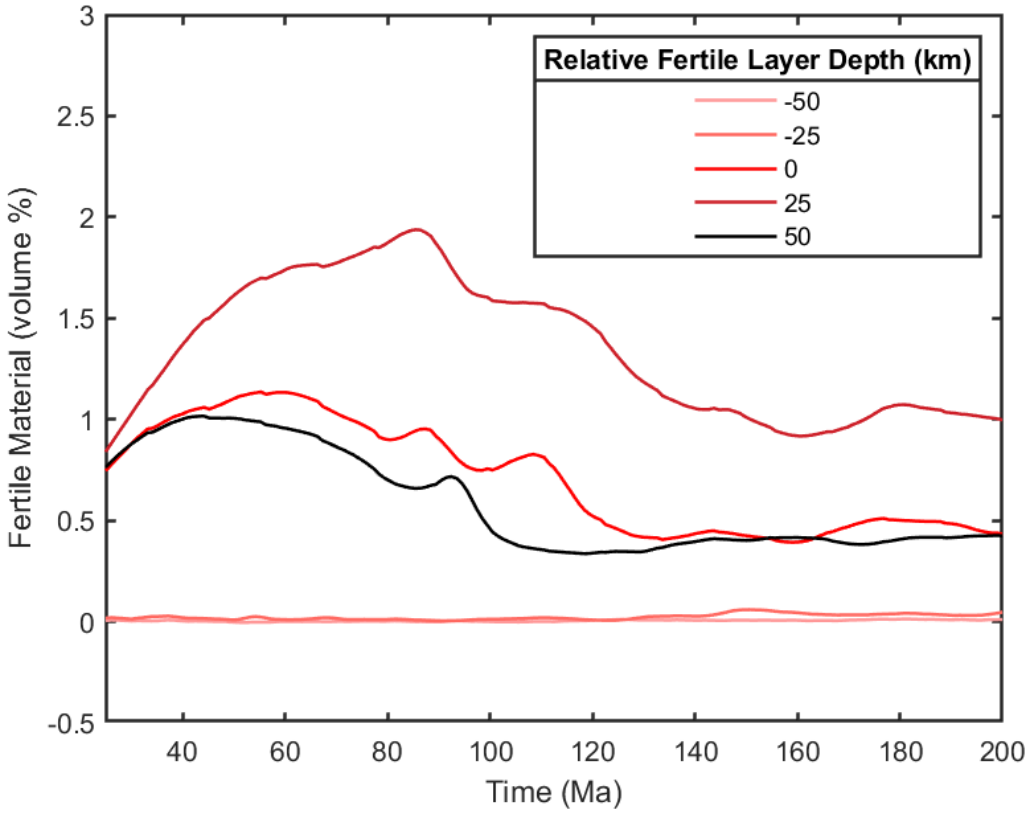

Figure 4.8 shows metasomatized layer concentrations below the oceanic lithosphere for models with different relative compositional positions of the metasomatized layer, in relation to the base of the cratonic lithosphere. The metasomatized layer is 50 km thick and the relative position is based on where the top of this layer is with respect to the base of the craton. Lighter shades of red denote shallower depths, with darker shades correlating to greater depths.

The models with the metasomatized layer located entirely within the asthenosphere show greater concentrations of fertile material in the COT. Figure 4.8 shows that there is less fertile material in the COT when the metasomatized layer starts 50 km deeper than the base of the craton, compared to when the metasomatized layer starts 25 km deeper than the base of the craton. Figure 4.7 shows the fertile material in the deepest position (50 km) diffusing into the mantle, with the shallowest part of the metasomatized layer potentially moving into the COT. This may suggest that there is an optimum depth at which fertile material is mobile enough to move into the COT, but not so mobile that it can be convected away easily. Models with the metasomatized layer either partially or entirely within the craton show a restricted fertile material mobility, with models -50 and -25 km showing fertile material concentrations <0.1 volume % [Figure 4.8].

4.4 2D Atlantic Ocean Opening Model Discussion

4.4.1 The Nature of Oceanic Spreading Models

The general dynamics of the rifting models correlate well with previous geodynamical models, with EDC_{SS} forming at the edge of the craton and with lithospheric dripping at the base of mature oceanic lithosphere. Models using a 2D static lithosphere model are predicted to have EDC_{SS} rolls form and influence depths of 660 km, as seen in models from Chapter 3 (King & Anderson, 1995, 1998; King & Ritsema, 2000), however with the introduction of ocean spreading, a mantle wind with an opposing force forms at the base of the model. The stronger the shearing, the more restricted EDC is in terms of its formation depth, with models producing convection rolls which have influence <410 km in depth (Till *et al.,* 2010) rather than 660 km (King & Anderson, 1995, 1998; King & Ritsema, 2000).

Some model assumptions and simplifications are worth noticing in this context. No mantle phase transitions are implemented in these models, or the associated rheological layering of the mantle transition zone. This could potentially influence the velocity of the 'mantle wind', and thus the depth at which EDC rolls have influence. In the cases where half-spreading rate was altered, there was some shearing as a result of return flow, which was an artefact of the tangential velocity boundaries emplaced on the model. Furthermore, the presented models are all performed in two dimensions, whereas a 3D model would probably display convection roll axes parallel to spreading direction (e.g. Kaislaniemi & van Hunen, 2014). In that case, the shearing would not affect the convection (van Hunen *et al.,* 2003; Ballmer *et al.,* 2009).

Guimarães *et al.* (2020) argue that the start of volcanism 40 Myr after the opening of the Atlantic suggests a slow mobilisation of the subcontinental metasomatized layer. However, our modelling results show that this mobilisation is almost instantaneous after the ocean basin forms. This suggests that another mechanism is required to explain the 40 Myr delay between Atlantic opening and the start of the volcanism along the Cameroon Volcanic Line.

4.4.2 The Effect of Half-spreading Rate Velocity

By altering the half-spreading rate, certain processes evolved which influenced the dynamics of the upper mantle. Modelling results show that for half-spreading rates > 3 cm/yr, lithospheric dripping is suppressed (van Hunen *et al.*, 2003), and is relevant for the dynamic evolution of the metasomatized layer.

This suppression impedes the formation of convection rolls, preventing the metasomatized layer from dripping, subsequently remaining as a coherent layer for longer. Intrinsically, more material is able to participate in shear-driven upwelling (SDU), a dynamical process where shear dominates the flow pattern such that upwellings are much closer to the COT than EDC_{WS}. SDU occurs due to asthenospheric shearing caused by half-spreading rates between 3-9 cm/yr (Conrad *et al.*, 2010; Bianco *et al.*, 2011; Ballmer *et al.*, 2013). Conrad *et al.* (2010) established that a half-spreading rate of 5 cm/yr correlated with a 0.5 cm/yr upwelling at the craton edge, and this explains the increase in fertile material as velocity of spreading increases. With SDU forming at velocities between 3-9 cm/yr, this may also explain the trend differences between the model with a half-spreading rate of 2 cm/yr and those ≥3 cm/yr [Figure 4.6].

4.4.3 Metasomatized Layer Parameters and Their Implications

Due to the ambiguity of a potential metasomatized layer, testing general parameters with a large range of values would supply a good sense of trends and the potential nature of a metasomatized layer. In these tests, the sensitivity of the dynamics to metasomatized layer density was established, with trends in fertile material concentration in the COT greatly affected over a 40 kg m^{-3} change in bulk metasomatized layer density (due to a fertile material density range of 2600-3000 kg m^{-3}). The critical point for fertile material density is 2800 kg m^{-3}, which correlates to the density of carbonates, the material most likely to be metasomatized in the craton, and generate carbonate-derived melt (Tappe *et al.*, 2017; Groves & Santosh, 2021). Here the values <2800 kg m^{-3} mostly drained into the COT throughout the model run, whilst those with densities >2800 kg m^{-3} sank to the base of the model, away from any region which may generate melt. The starting point of 2800 kg m^{-3} behaved like both denser and lighter models, transitioning from a buoyant metasomatized layer, to a denser

metasomatized layer ~100 Myr. This may suggest that fertile material would have to have a density <2800 kg m^{-3} to maintain a constant drainage of fertile material and therefore, volcanism along the Cameroon Volcanic Line.

In terms of the compositional position of the metasomatized layer, the further into the mantle it starts the more mobile the metasomatized layer is, leading to greater concentrations of fertile material in the COT. On the contrary, when large portions of the metasomatized layer are still within the craton, it remains immobile almost entirely. Even when testing a metasomatized layer with 25 km in the craton and 25 km in the mantle, the movement was limited. The extent of restriction may present an alternative to the CVL's origin: instead of being dependent on the Atlantic's opening, the fertile material may have required more time to thermally re-equilibrate after continental collision, moving from a cold, relatively stationary craton to a warmer, more mobile asthenosphere. 40 Myr after the Atlantic Ocean opened, the metasomatized layer was finally mobile enough to be released from the craton and mix into the upper mantle and generate melt.

Chapter 5

Discussion

5.1 Introduction

This chapter discusses both the static lithosphere models from Chapter 3 and how they compare to previous edge-driven convection (EDC) models, as well as the Atlantic Ocean opening model developed in Chapter 4. This will be followed by an analysis into the phenomena that occurred within the Atlantic Ocean opening model. Finally, model limitations and potential future work are discussed.

5.2 2D Static Lithosphere Model Comparison

5.2.1 Model Setup Comparison

To make numerical modelling studies conceptually and computationally tangible, a variety of simplified model setups have been adopted when investigating intraplate volcanism, reflecting the variety of hypothesized mechanisms previous work has focussed on. For example, in the construction of 2D numerical models, most edge-driven convection models have a limited depth extent down to either the 410 km (e.g. Till *et al.*, 2010) or 660 km discontinuity (e.g. van Wijk *et al.,* 2010; Kaislaniemi & van Hunen, 2014; Córdoba & Ballmer, 2021; Negredo *et al.,* 2022) to achieve high-enough spatial resolution with affordable computational power. Before further discussing the modelling results from Chapter 3 and 4, it is worth discussing a few model assumptions in more detail.

The vigour and longevity of EDC and its potential to explain intraplate volcanism have previously been examined, and lithosphere thickness plays a crucial role. A range of lithospheric thicknesses have been used, with cratonic thicknesses ranging from 100-200 km and oceanic lithosphere thicknesses ranging from 60-100 km. Due to these variations in thickness, there is a difference in the gradient of the continent-ocean transition (COT), with both steeper gradients and narrower

transition widths displaying larger and more vigorous EDC (Córdoba & Ballmer, 2021) and potentially more melt (Negredo *et al.*, 2022). Unless in extreme conditions (e.g. the Eastern part of the North China Craton, which lost most of its keel (Liu *et al.*, 2018)), typical intraplate cratons are between 150-300 km in thickness (e.g. Artemieva & Mooney, 2002; Hoggard *et al.*, 2020), providing a large lithospheric thickness gradient in models necessary for EDC formation and longevity.

Mantle plumes and whole mantle convection provide partial control on upper mantle temperatures. The associated dynamics of these deep mantle features complicate models that aim to focus on the development of EDC, especially if the model domain is confined to the upper mantle only. As such, different setups of sustained heating and simulation of heat permeating from the lower mantle has typically been used in those models. One approach is to impose a thermal boundary layer at the base of the model, which produces mantle plumes and convective upwelling from this boundary. Such upwellings are likely to occur in nature as well, but they complicate analysis if one is trying to isolate the effects of parameters on processes like EDC (e.g. Ballmer *et al.*, 2009; Córdoba & Ballmer, 2021). Alternatively, such upwellings are suppressed by imposing a bottom boundary condition that has no thermal boundary layer. In that case, heat supply to sustain realistic upper mantle temperatures is arranged through unrealistically high radiogenic heating (Kaislaniemi & van Hunen, 2014; Negredo *et al.*, 2022). The advantage of the latter model setup is that it removes the small plumes, so there is less of a disturbance in upper mantle dynamics and so a simple, yet clear understanding of the dynamical influences can be established. In this study, we adopted the latter approach. A radiogenic heating value that was 3.38 times higher than the present-day mantle average of 7.38×10^{-12} W kg^{-1} (Schubert *et al.*, 2001) was used to sustain statistically constant upper mantle temperatures. In comparison, Negredo *et al.* (2022) used a value of 16×10^{-12} W kg^{-1} for their models without basal heating, and 12×10^{-12} W kg^{-1} when EDC was accompanied by a mantle plume. Kaislaniemi & van Hunen (2014) used a range of different radiogenic values from 12 to 27 $\times 10^{-12}$ W kg^{-1}. Our applied radiogenic values therefore fall within the range of previously adopted values.

5.2.2 Mantle Dynamics

The type of edge-driven convection is an important factor to observe, as edge-driven convection as described by King & Anderson (1995, 1998) produces a much larger convection cell (EDC_{SS}) [see Section 1.3.3], which suggests volcanism further away from the craton. In comparison, the alternative form of edge-driven convection which requires asthenospheric shearing (EDC_{WS}) to induce a smaller convection roll at the continent-ocean boundary (COT), melt would potentially form closer to the craton. In terms of edge-driven convection and whether stricto sensu (EDC_{SS}) or with shear (EDC_{WS}) is the dominant type, our 2D numerical model shows parallels to Negredo *et al.* (2022), with an initial downwelling producing EDC_{SS}, which is quickly replaced and then dominated by EDC_{WS}. As mentioned in Section 1.3.3, the characteristics of these EDC-types are different, with EDC_{SS} influencing the deep upper mantle (King & Anderson, 1995, 1998) more than EDC_{WS} which is a smaller convection roll (Kaislaniemi & van Hunen, 2014; Negredo *et al.*, 2022).

The 2D static lithosphere numerical model are comparable to a failed rift, as seen along the CVL via the Benue Trough. The mantle dynamics predominantly displays EDC_{WS} which would suggest a narrow range of volcanism close to the COT, whilst the ocean spreading models exhibit EDC_{SS} which may produce wider spread melt further from the craton. Investigations into the extent of this melts width may reconcile with the observations of the CVL's width and its distance from the Congo craton.

5.2.3 Effects of a Metasomatized Layer on Melt Generation

To accurately calculate the amount of melt produced in the model, some form of tracking of melt depletion is required. However, in the present modelling setup, melting can only be calculated as a postprocessing step [Section 2.4] by way of comparison of the ambient temperature with the local solidus temperature. So, directly comparing observed melt from the Cameroon Volcanic Line (CVL) with model results is complicated, since depletion due to any melting is not accounted for. This simplification implies that material that has previously melted, will melt again just as easily. In the models presented, we circumvent this shortcoming by investigating if a metasomatized layer

flowing into the oceanic lithosphere from the base of the continents can enhance melting and explain the CVL. Instead of explicitly modelling melting, we track the movement of the metasomatized layer as a proxy for volcanism.

Whether edge-driven convection is capable of producing significant volumes of intraplate volcanism is unclear. The study by Córdoba & Ballmer (2021) displays small volumes of melt at an increased reference mantle temperature of 1400 °C, whilst Kaislaniemi & van Hunen (2014) observe that EDC provides periodical magmatism, with similar volumes and periodicity to the Atlas Mountains. This may be a result of increased internal heating, allowing for higher mantle temperatures, or a larger flow from below the craton, producing more asthenospheric shearing and mantle flow. Negredo *et al.* (2022) show the production of a 200 km narrow region of volcanism through EDC alone, which increases with the addition of a mantle plume and its associated increase in mantle temperature (1720 K). These studies illustrate that EDC-derived melt is difficult to produce without an added feature to enhance magmatism, with an increase in mantle temperature being a key factor. This increase in mantle temperatures is applicable in some cases. For example, the Canary Islands displays a HIMU geochemical signature suggesting a mantle plume in the region (Gurenko *et al.,* 2009; Negredo *et al.,* 2022). However, there is no recognised deep-seated positive thermal anomaly in the Cameroon region (Forte *et al.,* 2010; Reusch *et al.,* 2010, 2011; Celli *et al.,* 2020; Boyce *et al.,* 2021b). Instead, in this thesis we invoke a subcontinental metasomatized layer as a mechanism to enhance magmatism in the region.

5.3 Implications of an Ocean Opening Model

In the absence of a thermal anomaly, edge-driven convection may require an increase in volatiles to generate significant volumes of melt, with a metasomatized fertile layer explored in this thesis. This metasomatized layer would develop as cratons, which have been subjected to metasomatic events during their >2 Gyr existence (Foley, 2008; Wenker & Beaumont, 2017; Eeken *et al.,* 2018; Afonso *et al.,* 2022), become thicker due to continental collision (e.g. the formation of Gondwana). This thickening puts the carbonate-rich metasomatized base of the craton (Menzies *et al.,* 1987; Tappe *et al.,* 2017; Groves & Santosh, 2021) at increased depths, and stretches the geotherm

vertically. Over time, this stretched geotherm will re-equilibrate, with the lithosphere-asthenosphere boundary (LAB) moving back to shallower depths. By this process, the metasomatized fertile layer gradually becomes part of the asthenosphere, where it warms and weakens, which in turn, allows it to become mobile. The metasomatized layer may remain immobile below the lithosphere until continental break-up starts, which would allow the material to drain below thinner lithosphere, where it can replace or mix with the ambient mantle and reduce the local solidus [Section 1.5] (Guimarães *et al.*, 2020). This volatile rich material would melt at lower temperatures and pressures, aiding with melting derived from edge-driven convection processes. Our oceanic spreading models shows that for a bulk metasomatized layer density <3370 kg m^{-3}, this layer tends to flow into the continent-ocean transition (COT) [Section 4.3.1], as predicted by Guimarães *et al.* (2020).

The models in Section 4.3.2 show the significant impact of increasing the half-spreading rate velocity, particularly when the velocity is >3 cm/yr. At velocities of 3-9 cm/yr the dynamical process known as shear-driven upwelling (SDU) becomes prevalent (Conrad *et al.*, 2010; Ballmer *et al.*, 2013). As a result, SDU is able to pull greater concentrations of fertile material from the base of the cratonic lithosphere to the base of the oceanic lithosphere, in comparison to models which do not display SDU processes (<3 cm/yr half-spreading rates) [Figure 4.6]. Both EDC_{WS} and SDU share similar convective patterns, but they are derived from different dynamically mechanisms. In our models SDU strength changes are dictated by changes in plate velocity, as asthenospheric viscosity heterogeneity is not implemented. EDC_{WS} is dependent on asthenospheric shear generated by an increase in mantle temperature beneath thicker lithosphere (e.g. cratonic lithosphere). Distinguishing whether this flow is more greatly influenced by EDC_{WS} or SDU is hard to quantify. However, if compared to static lithosphere models where SDU is not present, there is an increase in upwelling fertile material. Another effect of increasing the spreading rate velocity is the suppression of lithospheric dripping which may impact the ability for convective processes like edge-driven convection to form (van Hunen *et al.*, 2003). However, this may be a feature only present in 2D numerical models, as Kaislaniemi & van Hunen (2014) observe longitudinal

convection rolls in their 3D models which are not prohibited by shearing, and form as a result of plate movement (e.g. Ballmer *et al.*, 2009).

Although not directly investigated the location of magmatism between models in Section 3 and Section 4 would differ slightly due to the mechanisms at play. The models in Section 3 demonstrated an intense upwelling, close to the COT which, in combination with the volatiles from the metasomatized layer, would restrict volcanism to a narrow width close to the craton. Models in section 4 displayed metasomatized material moving into the COT which may induce magmatism, as well as EDC_{SS} which provides the upwelling of the convection roll further from the craton. This combination may explain the Y-shaped nature of volcanism further in the continent, with volcanism found both close to the craton and further in the continent (Figure 1.2).

A key difference in the models presented in this thesis and the original proposal is the speed at which this subcontinental fertile material travels. Guimarães *et al.* (2020) proposed that the delay in volcanism after the opening of the Atlantic was due to the slow movement of the metasomatized layer, while our models show an early arrival, on the order of 1-3 Myr after the opening of the ocean basin.

The thermal position of the subcontinental metasomatized layer relative to the base of the craton plays a significant role in its mobility, and offers an alternative hypothesis to explain the ~40 Myr delay in volcanism. Instead of linking the timing of the metasomatized layer mobility directly to the opening of the Atlantic, we hypothesize that this timing is linked to the asthenospherization of this metasomatized layer [e.g. Figure 4.7a to Figure 4.7b]. After the continental collision and the associated continental shortening and thickening, the vertically stretched geotherm slowly re-equilibrates to its pre-collisional profile. This process exposes the subcontinental metasomatized layer to asthenospheric conditions, subsequently heating, weakening and increasing its mobility. Only then can this layer move into the COT as observed in models in Chapter 4. We therefore hypothesize that the time delay between the Atlantic Ocean opening and the onset of CVL volcanism is not due to the slow flow of mantle material, but due to the thermal changes resulting from the building and break up of supercontinents.

The presented modelling results exhibit a key difference in metasomatized layer drainage between the ocean opening model, which displays fertile material continually draining into the COT, and the numerical modelling in Chapter 3, which shows fertile material mixing is driven by the large-scale shearing forces. The implementation of spreading provides a change in convective patterns, with edge-driven convection stricto sensu the dominant form in the spreading models (Till *et al.*, 2010) compared to the edge-driven convection with shear forming in the static lithosphere-style numerical models which utilise an increased radiogenic heating value (e.g. Kaislaniemi & van Hunen, 2014; Negredo *et al.*, 2022). To obtain a better understanding of the resultant flow patterns at the COT, it is useful to view results in a different reference frame. All previous model results show velocities vectors relative to the model box [see Figure 5.1a]. However if they were plotted relative to the (moving) continent, the material below it, including the asthenosphere would be moving to the left. As a result, the movement of mantle material from this new reference frame makes observing EDC and asthenospheric flow easier [Figure 5.1b].

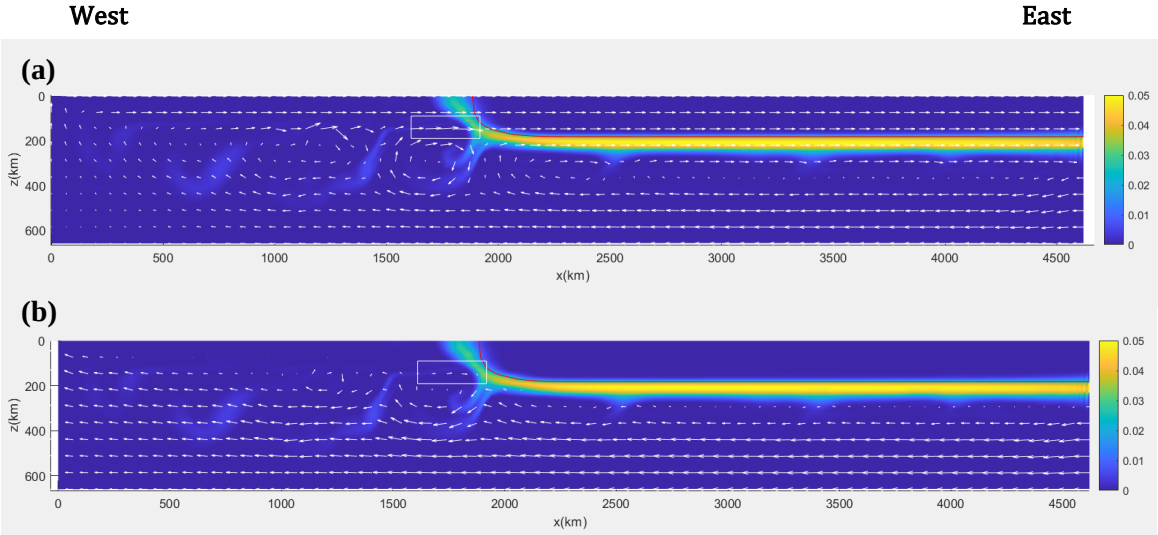

Figure 5.1a shows the ocean opening model using the same reference frame as models presented previously in this thesis, with the velocity vectors represented as white arrows. Here the model box is the reference frame, with the continent moving 2 cm/yr to the right, and the material beneath moving in the opposite direction.

Figure 5.1b shows the same model but showing velocities relative to that of the continent. Here, the velocity vectors are given an additional 2 cm/yr in the opposite direction to ocean spreading, making the continent stationary and the material below move relatively faster to the left.

5.4 Parameter Controls on Metasomatized Layer Drainage and Their Influence on Intraplate Volcanism

One of the main aims of this thesis was to determine the main controls on metasomatized layer drainage and assess their feasibility. Chapter 4 investigated the effects that half-spreading rate velocity, metasomatized layer position relative to the craton and metasomatized layer density has on the concentration and drainage of fertile material into the thinner oceanic lithosphere. Here, the concentration of fertile material acts as a proxy for melt due to the limitations in implementing melt depletion to give realistic melt values.

5.4.1 Half-spreading Rate Velocity

Generally, investigations into spreading rate velocity have shown it to be a highly influential parameter in forming intraplate volcanism. Ballmer *et al.* (2009) displays this by linking linear volcanic chains that lack an age progression in the Pacific, to self-organised small-scale convection induced by ocean spreading. In terms of spreading velocities and their interaction with cratons, the formation of shear-driven upwelling at velocities of 3-9 cm/yr drags material along the edge of the craton, with faster velocities correlating to greater upwelling velocities (Conrad *et al.*, 2010; Bianco *et al.,* 2011; Ballmer *et al.,* 2013). This process may explain why there is a large increase in the volume of fertile material at spreading rates of 5 cm/yr compared to 2 cm/yr. As the default value for half-spreading rate to test the other parameters was 2 cm/yr, it can be assumed that SDU does not occur in those tests, and that varying those parameters did not have as big of an impact as altering the velocities.

5.4.2 The Metasomatized Layer Density

The density plays a decisive role in the metasomatized layer's buoyancy, and therefore its ability to move up into the continent-ocean transition (COT). There is a narrow range of 30 kg m^{-3} in bulk metasomatized layer density determining whether the fertile material rises into the COT, or sinks with lithospheric drips. As this parameter is poorly constrained yet highly influential to fertile material drainage, it suggests this is an area that is essential for future work. Both the Cameroon

Volcanic Line and Fernando de Noronha display metasomatism at the base of the craton, as evidenced in xenoliths (Kogarko *et al.*, 2001) and thermochemical analysis via thermodynamically-constrained inversions of land and satellite datasets (Afonso *et al.*, 2022). This suggests that, in conjunction with the continental collision of Gondwana, a metasomatized layer could develop as predicted by Guimarães *et al.* (2020). A key parameter on metasomatized layer density is the volume of fertile material in this layer, as greater concentrations of fertile material will reduce the bulk density of the metasomatized layer. The metasomatized fertile layer is thought to be derived from carbonate-rich melts which are relatively lower density and are thought to remain buoyant in the upper mantle (Tappe *et al.*, 2017; Ritter *et al.*, 2020; Groves & Santosh, 2021). If future observations are able to determine the extent of cratonic metasomatism through either seismic studies or similar thermochemical analysis conducted by Afonso *et al.* (2022), then future models can have a more precise range of fertile material concentrations and densities.

5.4.3 The Relative Position of the Thermal Layer

The metasomatized layer is thought to derive from the separation of metasomatized material from the cratonic lithosphere via continental collision subjecting the fusible minerals to greater depths. As the geotherm begins to equilibrate after the continental collision, the lithosphere-asthenosphere boundary begins to move back to shallower depths, leading to the metasomatized layer's position changing from lithosphere to asthenosphere where it can be heated, weakened and become mobile (Foley, 2008; Guimarães *et al.*, 2020). This process allows fertile material to be released from the cratonic lithosphere into the asthenosphere, building up over time until the opening of an ocean can disturb it and initiate the migration of fertile material to shallower depths. As the extent at which the geotherm equilibrates is hard to know, so intrinsically is the depth at which the metasomatized layer resides. Here we test the mobility and dynamics of a 50 km thick metasomatized layer when it starts between 130 km and 230 km depths [Figure 5.2]. The results show that the depths can be categorised into 3 groups: the shallowest group which has its mobility restricted by being in the craton compositionally (-50 km and -25 km depth in relation to the base of the craton [Figure 4.7, 4.8]). the intermediate group that is outside the craton and in the asthenosphere and flows into the

continent-ocean transition (0 km and 25 km depth in relation to the craton [Figure 4.7, 4.8]). and the deepest group, where the effects of mantle convection move the fertile material around the upper mantle, rather than asthenospheric flow pulling material into the COT (50 km depth in relation to the base of the craton [Figure 4.7, 4.8]). The differences in mobility of the shallow group compared to the intermediate and deepest group is a result of the material the metasomatized layer is comprised of, with 95% of the metasomatized layer taking on the background material. For the shallow group they had elements of the craton which is highly viscous and restricting any flow, in comparison to the intermediate and deepest group with a background material of asthenosphere and mantle. To a lesser extent, the depth and therefore temperature has an impact on metasomatized layer mobility, with hotter material becoming weaker and thus more mobile [Figure 5.2]. As the deepest group shows, there if a point where the metasomatized layer is effected more by large-scale mantle convection processes, rather than asthenospheric flow moving material into the COT as seen in the intermediate group.

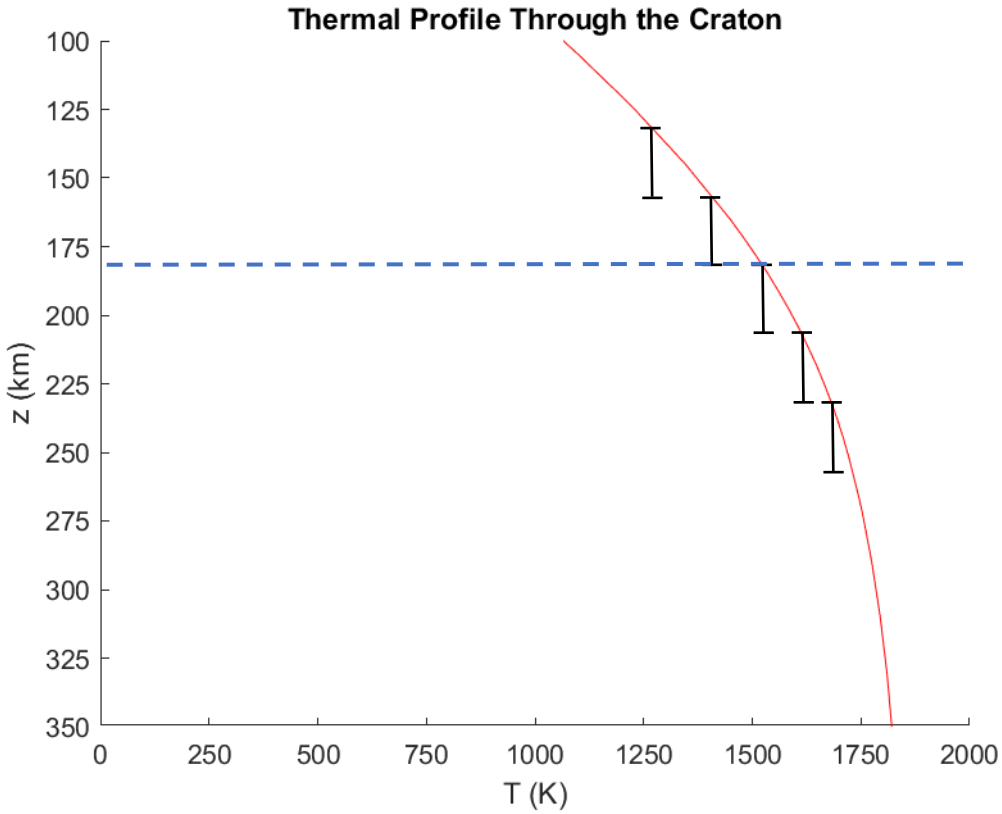

Figure 5.2. The location of the metasomatized layers (black vertical bars) in relation to the geotherm through the craton taken after 100 Myr of ocean spreading. The geotherm is zoomed in on this section to better show the metasomatized layer placement, which in order from top to bottom is -50 km, -25 km, 0 km, 25 km and 50 km deep in relation to the base of the craton (denoted by the blue dashed line).

As the results from Section 4.3.3 show, when the metasomatized layer was within the asthenosphere or mantle, the movement into the COT was rapid after the spreading began. This may be due to the density of the fertile material being low enough that it can flow into the COT. The speed at which fertile material flows into the COT does not correlate to the prediction made by Guimarães *et al.*, (2020), where it is suggested the metasomatized layer takes 40 Myr to move into the COT, corresponding to the delay in volcanism after the opening of the Atlantic. Looking at the difference in metasomatized layer position, we propose that the delay is not due to the metasomatized layer migration, but by the slow continuous build-up of material from the craton until it becomes unstable and released. In Figure 4.8 we see that when the metasomatized layer is half within the craton and half within the asthenosphere the metasomatized layer mobility is greatly impeded, where the volume of fertile material moving into the COT is negligible. However, once the metasomatized layer is fully within the asthenosphere, it can move more freely. As the geotherm still develops, more fertile material moves from the cratonic lithosphere and is present in the asthenosphere until the layer becomes unstable and begins to flow toward the COT.

The relative metasomatized layer depth is an important parameter in determining the volume of fertile material which can flow into the COT, and as such requires further investigation. The development of such models is beyond the scope of this work, but is planned for a future project, and may display the full evolution of a metasomatized layer as described by Guimarães *et al.* (2020). Cratons with metasomatized material undergo continental collision and then left for an appropriate length of time to equilibrate (e.g. ~500 Myr to simulate the formation and then splitting of Gondwana), before ocean spreading begins, triggering the movement of the fertile material.

5.4.4 Application to the Cameroon Volcanic Line

The Cameroon Volcanic Line (CVL) is a near-linear, ~1600 km in length volcanic chain between the Congo Craton and the West African Craton [Figure 2]. The feature shows no age progression and traverses both oceanic and continental lithospheres, with the difference in geochemistry slight due to crustal contamination (Fitton, 1987; Njome & de Wit, 2014). Volcanism along the chain has been long lived from 65 Ma to Present (Njome & de Wit, 2014), and therefore started ~40 Myr after

the continental break-up of Pangea (Guimarães *et al.*, 2020). The CVL shares similar features, geochemistry and magmatic history to a volcanic chain in NE Brazil, with evidence of: prolonged volcanism between 52 Ma and 1 Ma, a lack of age progression and alkaline geochemistry suggesting asthenospheric origin (Knesel *et al.*, 2011; Perlingerio *et al.*, 2013; Souza *et al.*, 2013). The contemporaneous nature of magmatism along the CVL and magmatism in the NE Brazil, post-continental break-up, suggests an alternative mechanism to mantle plumes is driving the intraplate volcanism.

Based on the results from the testing, appropriate values can be applied to fit those expected at the Cameroon Volcanic Line which can help determine if large concentrations of fertile material could drain in this region, aiding in melt generation.

The half-spreading rate of the Atlantic has been consistently slow through time with values between 1.5– 2.5 cm/yr, so as an average, the 2 cm/yr model would be a realistic fit to the half-spreading rate observations. Based on this, influences from shear driven upwelling would be weak, producing ~1.0 volume % of fertile material, and as such, fertile material drainage would be influenced primarily on the buoyancy of the metasomatized layer. With the percolation of carbonate melts thought to make up the fertile material (Tappe *et al.*, 2017; Guimarães *et al.*, 2020; Groves & Santosh, 2021), a reference density for the fertile material of $\leq$2800 kg m^{-3} would be the most viable, as carbonate melts remain buoyant in the upper mantle (Ritter *et al.*, 2020), and testing shows densities of $\leq$2800 kg m^{-3} displays positive buoyancy once the ocean opens [Section 4.3.1]. The fertile material within these models makes up a small percentage of the overall metasomatized layer, with the mantle of constant density comprising the rest. Caveats to this are that the volume of fertile material that composes the metasomatized layer is difficult to determine, and mantle density is not homogeneous, so may also play an influential role in regulating whether the metasomatized layer is buoyant or not. Here, the concentration of fertile material, as well as the density of the overall metasomatized layer are poorly constrained, but important parameters, and as such require work to better constrain them.

Due to the uncertainty of the metasomatized layer's positioning, it would be difficult to accurately gauge where the metasomatized layer lies during the opening of the Atlantic. If it is assumed that the delay in volcanism is through slow migration of material (e.g. Guimarães *et al.*, 2020), then the metasomatized layer would be positioned between 0 km and <50 km depth in relation to the base of the craton, as fertile material would be too restricted if it was situated in the craton. However, if the delay in volcanism is a result of the LAB still equilibrating, becoming shallower and allowing more metasomatized material to accumulate in the asthenosphere, then the metasomatized layer would be positioned closer to 0 km relative to the base of the craton. The models within this thesis model a relatively short period of time, when in fact the cratons would have ~500 Myr to allow the geotherm to equilibrate.

The thicknesses of the Congo and West African craton flanking the CVL are sufficient to produce a steep gradient at the COT [Figure 2], which, as observed by Negredo *et al.* (2022), aids in the generating of melt, particularly when ambient mantle temperatures are high. As the concentration of fertile material is used as a proxy for melt generation, it is hard to determine the quantitative impact these parameters and fertile material drainage would have on melt genesis under the CVL. Another key factor that may influence melt generation is the geological complexities of the CVL, such as the Benue Trough, which may impact the mantle dynamics to become more favourable to large-scale magmatism.

5.6 Model Limitations and Future Work

When models are used to investigate melt generation within the Earth, there is a level of simplification required due to the inherent complex nature of melting processes. The tracking of melt can simply be derived when a material reaches a temperature exceeding its solidus at a given pressure. Yet, in nature, melt can freeze and then later be remelted, with systems becoming far more complex when depletion and enrichment are introduced. As a material melts it loses fusible minerals first, leaving a depleted rock composed of high melting point minerals. As a result of this depletion, material becomes inherently harder to melt again due to the higher melting point of residual minerals. To add further complication, melt retention reduces both the density and viscosity of a

system, leading to slight differences in dynamics. Melt depletion was not implemented in the models presented within this thesis, and therefore tracking melt occurrence and melt volumes are not quantified. If melt were to be tracked and a sufficient depletion model was implemented, we could potentially observe an increase in the materials viscosity due to the reduction in water content alongside a potential decrease in buoyancy due to the change in composition. However, if melt is retained, then this may have the converse effect, making the material weaker whilst also decreasing its density. Instead, the concentration of fertile material was used as a proxy for melt. Although not vital to investigate metasomatized layer dynamics, it would have provided reliable melt generation values which could be compared to prior non-plume intraplate volcanism work. Having melt processes, including concurrent depletion as a result of melt within the models, offers the possibility to calculate melt volumes.

The processes within this thesis are modelled in 2D, and as a result is not capable of modelling 3D features (e.g. Ballmer *et al.,* 2009; Kaislaniemi & van Hunen, 2014). The Cameroon Volcanic Line is clearly a 3D structure, and adding a third dimension into the models would enable the investigation of the geological complexities in the region. In 3D the metasomatized layer would be more scattered potentially providing local zones of magmatism. The mantle and asthenospheric flow patterns observed in 2D would differ in 3D (e.g. Kaislaniemi & van Hunen, 2014 & Ballmer *et al.,* 2009). It is important to stress that if 3D models were produced, the local geology must also be implemented as we believe that features such as the Benue Trough may play a pivotal role in asthenospheric flow channelisation (Koch *et al.,* 2012; Elsheikh *et al.,* 2014; Li *et al.,* 2016) and subsequently the impact this has on self-organising mantle flow, particularly by the edge of the craton. Future work in this region may benefit from utilising a 3D ocean opening model, as it can encapsulate the geological features, such as the Benue Trough, the continental, oceanic and cratonic lithospheres and their geodynamical role in the enigmatic process of the CVL's formation. The transfer from 2D geodynamical models to 3D provides a distinct change in convection roll nature. Instead of forming perpendicular to the craton edge like as seen in 2D models, convection rolls in 3D models form parallel to the craton edge, with rolls forming perpendicular to plate movement

(Ballmer *et al.*, 2009; Kaislaniemi & van Hunen, 2014). This change in structure may explain why volcanism is offset from the Benue Trough, as this feature channelises material (Elsheikh *et al.*, 2014), small-scale convection can form with the movement of material, and decompression in combination with fertile material, may produce melt. This shows how integral the complexities are, with potentially all of them required to produced melt, further proving how unique EDC derived magmatism may be.

Chapter 6

Conclusion

This thesis investigated whether edge-driven convection in conjunction with a carbonate-rich metasomatized fertile layer (e.g. Foley, 2008; Afonso *et al.*, 2022), could explain the volcanism along the Cameroon Volcanic Line (Guimarães *et al.*, 2020). The dynamics of such a metasomatized layer was explored via a series of 2D ocean spreading numerical models, which aimed to determine the influential parameters controlling metasomatized layer behaviour, and whether it would impact the shallower lithosphere as predicted by Guimarães *et al.* (2020). The main conclusions of this work are as follows:

A metasomatized layer at the base of the craton is capable of moving into the thinner oceanic lithosphere, with the volume of fertile material dependent on several critical parameters. Density of the metasomatized layer played the most important role, with densities <2800 kg m^{-3} required for continuous drainage. The most influential parameter is the velocity of the spreading rate, as at the tested velocities of 3-5 cm/yr a dynamical process known as shear-driven upwelling (SDU) occurs, with faster velocities correlating with greater upwelling velocities. Here, SDU pulls material from initially below the craton, up its edge and into the thinner lithosphere. In addition, the higher spreading rate velocities impact the ability for lithospheric drips and subsequently small-scale convection to form, impeding edge-driven convection formation.

The fit between model results and the 40 Myr delay in volcanism after the opening of the Atlantic, requires more work, since the present models show that the metasomatized layer moves into the oceanic lithosphere after only 1-3 Myr. Other further improvements involve incorporating the intrinsically 3D features of the Cameroon Volcanic Line, including the mantle flow between the West African and Congo Cratons along the Benue Trough. The channelisation along this thin lithosphere may drive small-scale convective processes, leading to edge-driven convection and melt, due to the reduction in local solidus. By investigating the 3D structure of the region, work on

convection roll geometries and how they differ to 2D numerical models can be conducted, helping to establish if high spreading rate velocities impact small-scale convection and edge-driven convection in 3D.

Bibliography

Abdelsalam, M. G., Gao, S. S. & Liégeois, J-P., (2011). Upper mantle structure of the Saharan Metacraton. *Journal of African Earth Sciences*, **60**(5), 328-336, doi:10.1016/j.jafrearsci.2011.03.009

Adams, A., Wiens, D. A., Nyblade, A. A., Euler, G. G., Shore, P. J. & Tibi, R., (2015). Lithospheric instability and the source of the Cameroon Volcanic Line: Evidence from Rayleigh wave phase velocity tomography. *Journal of Geophysical Research: Solid Earth*, **120**(3), 1708-1727, doi:10.1002/2014JB011580

Afonso, J. C., Ben-Mansour, W., O'Reilly, S. Y., Griffin, W. L., Salajeghegh, F., Foley, S., Begg, G., Selway, K., Macdonald, A., Januszczak, N., Fomin, I., Nyblade, A.A. & Yang, Y., (2022). Thermochemical structure and evolution of cratonic lithosphere in central and southern Africa. *Nature Geoscience*, doi:10.1038/s41561-022-00929-y

Artemieva, I. M. & Mooney, W. D., (2002). On the relations between cratonic lithosphere thickness plate motions, and basal drag. *Tectonophysics* **358**, 211-231.

Ballmer, M. D., van Hunen, J., Ito, G., Bianco, T. A. & Tackley, P. J., (2009). Intraplate volcanism with complex age-distance patterns: a case for small-scale convection sublithospheric convection. *Geochemistry, Geophysics, Geosystems*, **10**, Q06015, doi:10.1029/2009GC002386

Ballmer, M. D., Conrad, C. P., Smith, E. I. Harmon, N., (2013). Non-hotspot volcano chains produced by migration of shear-driven upwelling towards the East Pacific Rise. *Geology*, **41**(4), 479-482, doi:10.1130/G33804.1

Bangerth, W., Dannberg, J., Gassmöller, R., Heister, T., (2020a). ASPECT v2.2.0 (version v2.2.0) Zenodo. doi:10.5821/ZENODO.3924694

Bangerth, W., Dannberg, J., Gassmöller, R., Heister, T., and others, (2020b). ASPECT: Advanced Solver for Problems in Earth's ConvecTion, User Manual. Figshare. doi:10.6084/m9.figshare.4865333

Bastow, I. D., Nyblade, A. A., Stuart, G. W., Rooney, T. O. & Benoit, M. H., (2008). Upper mantle seismic structure beneath the Ethiopian hot spot: Rifting at the edge pf the African low-velocity anomaly. *Geochemistry, Geophysics, Geosystems*, **9**(12), Q12022, doi:10.1029/2008GC002107

Bianco, T. A., Conrad, C. P. & Smith, E. I., (2011). Time dependence of intraplate volcanism caused by shear-driven upwelling of low-viscosity regions within the asthenosphere. *Journal of Geophysical Research*, **116**(B11103), doi:10.1029/2011JB008270

Billen, M. I. and Hirth, G., (2007). Rheologic controls on slab dynamics. *Geochem. Geophys. Geoosyst.* **8**(8), doi:10.1029/2007GC001597

Bonvalot, S., Briais, A., Peyrefitte, A., Gabalda, G., Balmino, G., and Moreaux, G., (2010). The World Digital Gravimetric Anomaly Map, *CGMW General Assembly / UNESCO, Paris, France*.

Boyce, A., Bastow, I. D., Cottaar, S., Kounoudis, R., Guilloud De Courbeville, J., Caunt, E. & Desai, S., (2021a). AFRP20: New P-wavespeed model for the African mantle reveals two whole-mantle plumes below East Africa and Neoproterozoic modification of the Tanzania craton. *Geochemistry, Geophysics, Geosystems*, **22**(3), e2020GC009302, doi:10.1029/2020GC009302

Boyce, A. & Cottaar, S., (2021b). Insights into deep mantle thermochemical contributions to African magmatism from converted seismic phases. *Geochemistry, Geophysics, Geosystems*, **22**, e2020GC009478, doi:10.1029/2020GC009478

Boyd, F. R., (1973). A Pyroxene geotherm. *Geochimica et Cosmochimica Acta*, **37**(12), 2533-2538, doi:10.1016/0016-7037(73)90263-9

Bürgmann, R., Dresen, G., (2008). Rheology of the lower crust and Upper Mantle: Evidence from Rock Mechanics, Geodesy, and Field Observations. *Annu. Rev. Earth Planet. Sci.* **36,** 531-567, doi:10.1146/annurev.earth.36.031207.124326

Burke, K. C. & Wilson, J. T., (1976). Hot spots on the Earth's surface. *Sci. Am.,* **235**, 46-57.

Burke, K., (2001). Origin of the Cameroon Volcanic Line of volcano-capped swells. *The Journal of Geology,* **109**, 349-362.

Byerlee, J., (1978). Friction of rocks. Pure Appl. Geophys. PAGEOPH 116, 615–626. doi:10.1007/BF00876528

Castaing, C., Feybesse, J. L., Thiéblemont, D., Triboulet, C. & Chèvremont, P., (1994). Palaeographical reconstructions of the Pan-African/Brasiliano orogen: closure of an oceanic domain or intracontinental convergence between major blocks? *Precambrian Research,* **69**(1-4), 327-344, doi:10.1016/0301-9268(94)90095-7

Cathles, L. M., (1975). The viscosity of the Earth's Mantle. *Princeston University Press, Princeton, NJ,* ISBN: 9781400867684.

Celli, N. L., Lebedev, S., Schaeffer, A. J., Ravenna, M. & Gaina, C., (2020). The upper mantle beneath the South Atlantic Ocean, South America and Africa from waveform tomography with massive data sets. *Geophysical Journal International,* **221**(1), 178-204, doi:10.1093/gji/ggz574

Chevrot, S. Vinnik, L. & Montagner J-P., (1999). Global-scale analysis of the mantle Pds phases. *Journal of Geophysical Research: Solid Earth,* **104**(B9) 20203-20219, doi:10.1029/1999JB900087

Christensen, U. R. and Yuen, D. A., (1985). Layered Convection Induced by Phase Transitions. *Journal of Geophysical Research*, **90**(B12), 10291-10300.

Conrad, C. P., Wu, B., Smith, E. I., Bianco, T. A & Tibbetts, A., (2010). Shear-driven upwelling induced by lateral viscosity variations and asthenospheric shear: A mechanism for intraplate volcanism. *Physics of the Earth and Planetary Interiors*, **178,** 162-175.

Córdoba, A. M-C. & Ballmer, M. D., (2021). The role of edge-driven convection in the generation of volcanism -Part 1: A 2D systematic study. *Solid Earth,* **12**, 613-632, doi:10.5194/se-12-613-2021

Currie, C. A. & van Wijk, J., (2016). How craton margins are preserved: Insights from geodynamical models. *Journal of Geodynamics,* **100**, 144-158, doi:10.1016/j.jog.2016.03.015

Daly, M., Chorowicz, J. & Fairhead, J. D., (1989). Rift basin evolution in Africa: The influence of reactivated steep basement shear zones. *Geological Society London, Special Publications*, **44**(1), 309-344, doi10.1144/GSL.SP.1989.044.01.17

Dannberg, J., Eilon, Z., Faul, U., Gassmöller, R., Moulik, P., Myhill, R., (2017). The importance of grain size to mantle dynamics and seismological observations. *Geochemistry, Geophysics, Geosystems*,**18**(8), 3034-3061, doi:10.1002/2017GC006944

Davies, D. R., Goes, S. Davies, J. H., Schuberth, B. S. A., Bunge, H.-P. & Ritsema, J., (2012). Reconciling dynamic and seismic models of Earth's lower mantle: The dominant role of thermal heterogeneity. *Earth Planetary Science Letters,* **353,** 253-269, doi:10.1016/j.epsl.2012.08.016

De Plaen, R. S. M., Bastow, I. D., Chambers, E. L., Keir, D., Gallacher, R. J. & Keane, J., (2014). The development of magmatism along the Cameroon Volcanic Line: Evidence from seismicity and seismic anisotropy. *Journal of Geophysical Research: Solid Earth,* **119**(5), 4233-4252, doi:10.1002/2013JB010583

Déruelle, B., Ngounouno, I. & Demaiffe, D., (2007). The 'Cameroon Hot Line' (CHL): A unique example of active alkaline intraplate structure in both oceanic and continental lithospheres. *Geoscience Reviews*, **339**(9), 589-600, doi:10.1016/j.crte.2007.07.007

Dimanov, A. & Dresen, G., (2005). Rheology of synthetic anorthite-diopside aggregates: implications for ductile shear zones. *Journal of Geophysical Research*, **110**(B07203), doi:10.1029/2004JB003231

Dorbath, C., Dorbath, L., Farihead, J. D. & Stuart, G. W., (1986). A teleseismic delay time study across the Central African Shear Zone in the Adamawa Region of Cameroon, West Africa. *Geophysical Journal International,* **86**(3), 751-766, doi:10.1111/j.1365-246X.1986.tb00658.x

Duncan, R. A. & Richards, M. A., (1991). Hotspots, mantle plumes, flood basalts, and true polar wander. *Reviews of Geophysics*, **29**(1), 31-50.

Dunlop, H. M. & Fitton, G. J., (1979). A K-Ar and Sr-isotopic study of the volcanic rocks of the island or Principe, West Africa – Evidence for mantle heterogeneity beneath the Gulf of Guinea. Contrib. Mineral. Petrol., **71**(2), 125-131, doi:10.1007/BF00375428

Ebinger, C. J. & Sleep, N. H., (1998). Cenozoic magmatism throughout east Africa resulting from impact of a single plume. *Nature*, **385**, 788-791.

Eeken, T., Goes, S., Pedersen, H. A., Arndt, N. T. & Bouilhol, P., (2018). Seismic evidence for depth-dependent metasomatism in cratons. *Earth and Planetary Science Letters*, **491**, 148-159, doi:10.1016/j.epsl.2018.03.018

Elkins-Tanton, L. T., (2007). Continental magmatism, volatile recycling, and a heterogeneous mantle caused by lithospheric gravitational instabilities. *Journal of Geophysical Research* **112**(B03405), doi:10.1029/2005JB004072

Elsheikh, A. A. Gao, S. S. & Liu, K. H., (2014). Formation of the Cameroon Volcanic Line by lithospheric basal erosion: Insight from mantle seismic anisotropy. Journal of African Earth Sciences, **100**, 96-108, doi:10.1016/j.jafrearsci.2014.06.011

Fairhead, J. D., (1988). Mesozoic plate tectonic reconstructions of the central South Atlantic Ocean: The role of the West and Central African rift system. *Tectonophysics*, **155**(1-4), 181-191, doi:10.1016/0040-1951(88)90265-X

Fairhead, J. D. & Okereke, C. S., (1990). Crustal thinning and extension beneath the Benue Trough based on gravity studies. *Journal of African Earth Sciences*, **11**(3-4), 329-335, doi:10.1016/0899-5362(90)90011-3

Fishwick, S. & Bastow, I. D., (2011). Towards a better understanding of African topography: A review of passive-source seismic studies of the African crust and upper mantle. *Geological Society London Special Publications*, **357**(1), 343-371, doi:10.1144/SP357.19

Fitton, J. G. & Dunlop, H. M., (1985). The Cameroon Line, West Africa, and its bearing on the origin of oceanic and continental alkali basalt. *Earth and Planetary Science Letters*, **72**(1), 23-38, doi:10.1016/0012-821X(85)90114-1

Fitton, J. G., (1987). The Cameroon Line, West Africa: A comparison between oceanic and continental alkaline volcanism. *Alkaline Igneous Rocks*, **30**, 273-291.

Fodor, R. V., Mukasa, S. B. & Sial, A. N., (1998). Isotopic and trace-element indications of lithosperhic and asthenospheric components in Tertairy alkalic basalts, northeast Brazil. *Lithos*, **43**(4), 197-217, doi:10.1016/S0024-4937(98)00012-7

Foley, S. F., (2008). Rejuvenation and erosion of the cratonic lithosphere. *Nature Geoscience,* **1**, 503-510, doi:10.1038/ngeo261

Forte, A. M. & Mitrovica, J. X., (1996). New inferences of mantle viscosity from joint inversion of long-wavelength mantle convection and post-glacial rebound data. *Geophysical Research Letters*, **23**(10), 1147-1150.

Forte, A. M., Quéré, S., Moucha, R., Simmons, N. A., Grand, S. P., Mitrovica, J. X. & Rowley, D. B., (2010). Joint Seismic-geodynamic-mineral physical modelling of African geodynamics: A reconciliation of deep-mantle convection with surface geophysical constraints. *Earth and Planetary Science Letters*, **295**(3-4), 329-341, doi:10.1016/j.epsl.2010.03.017

French, S. W. & Romanowicz, B., (2015). Broad plumes rooted at the base of the Earth's mantle beneath major hotspots. *Nature,* **525**, 95-99, doi:10.1038/nature14876

Gasperini, P. & Sabadini, R., (1989). Lateral heterogeneities in mantle viscosity and post-glacial rebound. *Geophysical Journal International*, **98**(3), 413-428, doi:10.1111/j.1365-246X.1989.tb02279.x

Gassmöller, R., Dannberg, J., Bangerth, W., Heister, T. and Myhill, R., (2020). On formulations of compressible mantle convection. *Geophysical Journal International*, **221**, 1264-1280, doi:10.1093/gii/ggaa078

Gassmöller, R., Lokavarapu, H., Heien, E., Puckett, E. G. and Bangerth, W., (2018). Flexible and scalable particle-in-cell methods with adaptive mesh refinement for geodynamic computations. *Geochemistry, Geophysics, Geosystems,* **19**(9), 3596-3604, doi:10.1029/2018GC007508

Gassmöller, R., Dannberg, J., Bredow, E., Steinberger, B., Torsvik, T. H., (2016). Major influence of plume-ridge interaction, lithosphere thickness variations, and global mantle flow on hotspot volcanism – The example of Tristan. *Geochemistry, Geophysics, Geosystems,* **17**(4), 1454-1479, doi:10.1002/2015GC006177

Gerlach, D. C., Stormer, J. C. & Mueller, P. A., (1987). Isotopic geochemistry of Fernando de Noronha. *Earth and Planetary Science Letters,* **85**(1-3), 129-144, doi:10.1016/0012-821X(87)90027-6

Gerya, T., (2010). Introduction to Numerical Geodynamic Modelling. *Cambridge University Press*, Cambridge.

Griffin, W. L., O'Reilly, S. Y., Abe, N., Aulbach, S., Davies, R. M., Pearson, N. J., Doyle, B. J. & Kivi, K., (2003). The origin and evolution of Archean lithospheric mantle, *Precambrian Research*, **127**(1-3), 19–41, doi:10.1016/S0301–9268(03)00180-3

Groves, D. I. & Santosh, M., (2021) Craton and thick lithosphere margins: The sites of giant mineral deposits and mineral provinces. *Gondwana Research,* **100**, 195-222, doi:10,1016/j.gr.2020.06.008

Guimarães, A. R., Fitton, G., Kirstein, L. & Barfod, D. N., (2020). Contemporaneous intraplate magmatism on conjugate South Atlantic margins: a hotspot conundrum. *Earth and Planetary Science Letters*, **536**, 116-147, doi:10.1016/j.epsl.2020.116147

Gurenko, A. A., Sobolev, A. V., Hoernle, K. A., Hauff, K. & Schmincke, H-U., (2009). Enriched, HIMU-type peridotite and depleted recycled pyroxenite in the Canary plume: A mixed-up mantle. *Earth and Planetary Science Letters,* **277**(3-4), 514-524, doi:10.1016/j.epsl.2008.11.013

Hall, C. E. & Parmentier, E. M., (2003). Influence of grain size evolution on convective instability. *Geochemistry, Geophysics, Geosystems*, **4**(3), 1029, doi:10.1029/2002GC000308

Halliday, A. N., Dickin, A. P., Fallick, A. E. & Fitton, J. G., (1988). Mantle dynamics: a Nd, Sr, Pb and O isotopic study of the Cameroon Line volcanic chain. *Journal of Petrology,* **29**(1), 181-211, doi:10.1093/petrology/29.1.181

Halliday, A. N., Davies, G. R., Lee, D. -C., Tommasini, S. Paslick, C. R., Fitton, J. G. & James, D. E., (1992). Lead isotope evidence for young trace element enrichment in the oceanic upper mantle. *Nature*, **359**, 623-627, doi:10.1038/359623a0

Hansma, J., Tohver, E., Schrank, C., Jourdan, F. & Adams, D., (2016). The timing of the Cape Orogeny: New $^{40}Ar/^{39}Ar$ age constraints on deformation and cooling of the Cape Fold Belt, South Africa. *Gondwana Research,* **32**, 122-137, doi:10.1016/j.gr.2015.02.005

Heister, T., Dannberg, J., Gassmöller, R., Bangerth, W., (2017). High Accuracy Mantle Convection Simulation through Modern Numerical Methods. II: Realistic Models and Problems. *Geophysical Journal International,* **210**, 833-851, doi:10.1093/gji/ggx195

Henriques, M. H. & Neto, K. A., (2019). Geoheritage at the Equator: Revisiting selected geosites of São Tomé Island (Cameron Line, Central Africa). In: Maria Helena Henriques, editor. *Prime Archives in Sustainability*. Hyderabad, India: Vide Leaf. 2019.

Hirth, G. & Kohlstedt, D., (2003). Rheology of the upper mantle and the mantle wedge: A view from the experimentalists. *Inside the Subduction Factory,* **138**, 83-105, doi:10.1029/138GM06

Hoggard, M. J., Czarnota, K., Richards, F. D., Huston, D. L., Jaques, L. A. & Ghelichkhan, S., (2020). Global distribution of sediment-hosted metals controlled by craton edge stability. *Nature Geoscience*, **13,** 504-510, doi:10.1038/s41561-020-0593-2

Ishii, T., Huang, R., Myhill, R., Fei, H., Koemets, I., Liu, Z., Maeda, F., Yuan, L., Wang, L., Druzhbin, D., Yamamoto, T., Bhat, S., Farla, R., Kawazoe, T., Tsujino, N., Kulik, E., Higo, Y., Tange, Y. & Katsura, T., (2019). Sharp 660-km discontinuity controlled by extremely narrow binary post-spinel transition. *Nature Geoscience*, **12**, 869-872, doi:10.1038/s41561-019-0452-1

Ismail-Zadeh, A. & Tackley, P., (2010). Computational Methods for Geodynamics. *Cambridge University Press, New York, 2010.* 322pp. ISBN 9780521867672

Janse, A., (1991). Is Clifford's Rule Still Valid? Affirmative Examples from Around the World. *International Kimberlite Conference: Extended Abstracts*, **5**, 196–198. https://doi.org/10.29173/ikc2510

Jordan, T.H., (1978). Composition and development of the continental tectosphere. *Nature*, **274**, 544-548, doi:10.1038/274544a0

Kaislaniemi, L., van Hunen, J., Allen, M. B. & Neill, I., (2014). Sublithospheric small-scale convection – A mechanism for collision zone magmatism. *Geology*, **42**(4), 291-294, doi:10.1130/G35193.1

Kaislaniemi, L. & van Hunen, J., (2014). Dynamics of lithospheric thinning and mantle melting by edge-driven convection: Application to Moroccan Atlas mountains. *Geochemistry, Geophysics, Geosystems*, **15**(8), 3175-3189, doi:10.1002/2014GC005414

Kamgang, P., Chazot, G., Njinfang, E., Ngongang, N. B. T., Tchoua, F. M., (2013). Mantle source and magma evolution beneath the Cameroon Volcanic Line: Geochemistry of mafic rocks from the Bamenda Mountains (NW Cameroon). Gondwana Research, **24,** 727-741, doi:10.1016/j.gr.2012.11.009

Karato, S., (1988). The role of recrystallization in the preferred orientation of olivine. *Physics of the Earth and Planetary Interiors*, **51**(1-3), 107–122, doi:10.1016/0031-9201(88)90029-5

Karato, S., (2010). Rheology of the Earth's mantle : A historical review. *Gondwana Research*, **18**(1), 17-45, doi:10.1016/j.gr.2010.03.004

Karato, S. & Wu, P., (1993). Rheology of the Upper Mantle: A Synthesis. *Science*, **260**(5109), 771–778.

Katz, R. F., Spiegelman, M. & Langmuir, C. H., (2003). A new parameterization of hydrous mantle melting. *Geochemistry, Geophysics, Geosystems*, **4**(9), 1073, doi:10.1029/2002GC000433

Kaufmann, G. & Lambeck, K., (2000). Mantle dynamics, postglacial rebound and the radial viscosity profile. *Physics of the Earth and Planetary Interiors*, **121**(3-4), 301-324, doi:10.1016/S0031-9201(00)00174-6

King, S. D., (1995). Radial models of mantle viscosity: results from a genetic algorithm. *Geophysical Journal International*, **122(**3**)**, 725-734, doi:10.1111/j.1365-246X.1995.tb06831.x

King, S. D. & Anderson, D. L., (1995). An alternative mechanism of flood basalt formation. *Earth and Planetary Science Letters*, **136**(3-4), 269-279, doi:10.1016/0012-821X(95)00205-Q

King, S. D. & Anderson, D. L., (1998). Edge-driven convection. *Earth and Planetary Science Letters*, **160**(3), 289-296, doi:10.1016/S0012-821X(98)00089-2

King, S. D. & Ritsema, J., (2000). African hot spot volcanism: Small-scale convection in the upper mantle beneath cratons. *Science*, **290** 1137-1140

Knesel, K. M., Souza, Z. S. D, Vasxonxelos, P. M., Cohen, B. E. & Silveria, F. V., (2011). Young volcanism in the Borborema Province, NE Brazil, shows no evidence for a trace of the Fernando de Noronha plume on the continent. *Earth Planetary Science Letters*, **302**, 38-50, doi:10.1016/j.epsl.2010.11.036

Koch, F. W., Wiens, D. A., Nyblade, A. A., Shore, P. J., Rigobert Tibi, Ateba, B., Tabod, C. T., Nnange, J. M., (2012). Upper-mantle anisotropy beneath the Cameroon Volcanic Line and Congo Craton from shear wave splitting measurements. *Geophysical Journal International*, **190**(1), 75-86, doi:10.1111/j.1365-246X.2012.05497.x

Kogarko, L., Kurat, G. & Ntaflos, T., (2001) Carbonate metasomatism of the oceanic mantle beneath Fernando de Noronha Island, Brazil. *Contributions to Mineralogy and Petrology*, **140,** 577-587, doi:10.1007/s004100000201

Korenaga, J. & Jordan, T. H., (2004). Physics of multiscale convection in Earth's mantle: Evolution of sublithospheric convection. *Geodesy and Gravity/ Tectonophysics,* **109**(B1), doi:10.1029/2003JB002464

Kronbichler, M., Heister, T., Bangerth, W., (2012). High accuracy mantle convection simulation through modern numerical methods. *Geophysical Journal International,* **191**(1), 12-29, doi:10.1111/j.1365-246X.2012.05609

Larson, R. L., (1991). Latest pulse of Earth: Evidence for a mid-Cretaceous superplume. *Geology*, **19**(6), 547-550, doi:10.1130/0091-7613(1991)019<0547:LPOEEF>2.3.CO;2

Lambeck, K. & Nakada, M., (1990). Late Pleistocene and Holocene sea-level change along the Australian coast, *Palaeogeography, Palaeoclimatology, Palaeoecology (Global and Planetary Change Section),* **89,** 143-176.

Lawrence, J. F. & Shearer, P. M., (2006). A global study of transition zone thickness using receiver functions. *Journal of Geophysical Research: Solid Earth*, **111**(B6), doi:10.1029/2005JB003973

Lécorché, J. P., Bronner, G., Dallmeyer, R. D., Rocci, G. & Roussel, J., (1991). The Mauritanide Orogen and its Northern Extensions (Western Sahara and Zemmour), West Africa. In: Dallmeyer, R. D., Lécorché, J.P. (eds) *The West African Orogens and Circum-Atlantic Correlatives*. IGCP-Project 233. Springer, Berlin, Heidelberg, doi:10.1007/978-3-642-84153-8_9

Lee, D-C., Halliday, A. N., Fitton, G. J. & Poli, G., (1994). Isotopic variations with distance and time in the volcanic islands of the Cameroon line: evidence for a mantle plume origin. *Earth and Planetary Science Letters,* **123**, 119-138.

Lenardic, A. & Moresi, L. -N., (1999). Some thoughts on the stability of cratonic lithosphere: Effects of buoyancy and viscosity. *Journal of Geophysical Research,* **104**, 12747-12758, doi:10.1029/1999JB900035

Lenardic, A., Moresi, L. -N. & Mühlhous, H., (2003). Longevity and stability of cratonic lithosphere: insight from numerical simulations of coupled mantle convection and continental lithosphere. *J. Geophys. Res.,* **108**, (B6), doi:10.10129/2001JB000169

Li, Z-H., Liu, M. & Gerya, T., (2016). Lithosphere delamination in continental collisional orogens: A systematic numerical study. *J. Geophys. Res. Solid Earth*, **121,** 5186-5211, doi:10.1002/2016JB013106

Liu, D. & Chen, L., (2019). Edge-driven convection and thinning of craton lithosphere: Two-dimensional thermal-mechanical modeling. *Science China Earth Sciences,* **62**, 2106-2120, doi:10.1007/s11430-019-9371-0

Liu, L., Morgan, J. P., Xu, Y. & Menzies, M., (2018). Craton Destruction 1: Cratonic keel delamination along a weak midlithospheric discontinuity layer. *Journal of Geophysical Research: Solid Earth*, **123**(11), 10044-10068, doi:10.1029/2017JB015372

Liu, X. & Zhong, S., (2016). Constraining mantle viscosity structure for a thermochemical mantle using the geoid observation. *Geochemistry, Geophysics, Geosystems*, **17**(3), 895-913, doi:10.1002/2015GC006161

Menzies, M. A., Rogers, N., Tindle, A. & Hawkesworth, C. J., (1987). Metasomatic and enrichment processes in lithospheric peridotites, an effect of asthenosphere-lithosphere interaction. In: Menzies, M. A. and Hawkesworth, C. J. eds. *Mantle Metasomatism.* London, UK: Academic Press, pp.313-361.

Meyers, J. B., Rosendahl, B. R. Harrison, C. G. A. & Ding, Z-D., (1998). Deep-imaging seismic and gravity results from the offshore Cameroon Volcanic Line, and speculation of African hotlines. *Tectonophysics,* **284**, 31-63.

Milelli, L., Fourel, L. & Jaupart C., (2012). A lithospheric instability origin for the Cameroon Volcanic Line. *Earth and Planetary Sciences Letters*, **335-336**, 80-87, doi: 10.1016/j.epsl.2012.04.028

Missenard, Y., Zeyen, H., Frizon de Lamotte, D., Leturmy, P., Petit, C., Sébrier, M. & Saddiqi, O., (2006). Crustal versus asthenospheric origin of relief of the Atlas Mountains of Morocco. *Journal of Geophysical Research,* **111**(B3), doi:10.1029/2005JB003708

Missenard, Y. & Cadoux, A., (2012). Can Moroccan Atlas lithospheric thinning and volcanism be induced by Edge-Driven Convection?, *Terra Nova*, **24**(1), 27–33, doi:10.1111/j.1365-3121.2011.01033.x

Mitrovica, J. X. & Peltier, W. R., (1991a). A complete formalism for the inversion of post-glacial rebound data: resolving power analysis. *Geophysical Journal International,* **104**(2), 267-288, doi:10.1111/j.1365-246X.1991.tb02511.x

Mitrovica, J. X. & Peltier, W. R., (1991b). Radial resolution in the inference of mantle viscosity from observations of glacial isostatic adjustment. In: Sabadini, R., Lambeck, K., Boschi, E. (eds) Glacial Isostasy, Sea-level and Mantle Rheology. NATO ASI Series, vol 334. Springer, Dordrecht. doi:10.1007/978-94-011-3374-6_4, ISBN:978-94-011-3374-6.

Montigny, R., Ngounouno, I. & Déruelle, B., (2004). Ages K-Ar magmatic rocks from the Garoua rift: their place in the frame of the 'Cameroon Line'. *Geoscience Reviews*, **336**(16), 1463-1471, doi:10.1016/j.crte.2004.08.005

Morgan, W. J., (1971). Convection Plumes in the Lower Mantle. *Nature*, **230**, 42-43.

Müller, D. R., Sdrolias, M., Gaina, C. & Roest, W. R., (2008). Age, spreading rates, and spreading asymmetry of the world's ocean crust. *Geochemistry, Geophysics, Geosystems*, **9**(4), doi:10.1029/2007GC001743

Nakada, M. & Lambeck, K., (1989). Late Pleistocene and Holocene sea-level change in the Australian region and mantle rheology. *Journal of Geophysical Research,* **96(**3), 497-517, doi:10.1111/j.1365-246X.1989.tb06010.x

Negredo, A. M., van Hunen, J., Rodrígues- González, J. & Fullea, J., (2022). On the origin of the Canary Islands: Insights from mantle convection modelling. *Earth and Planetary Science Letters,* **584**, doi:10.1016/j.epsl.2022.117506

Ni, S. D., Tan, E., Gurnis, M. & Helmberger, D., (2002). Sharp sides to the African Superplume, *Science*, **296**,1850-1852

Ngako, V., Affaton, P. Nnange, J.M. & Njanko, T., (2003). Pan-African tectonic evolution in central and Southern Cameroon: Transpression and transtension during sinistral shear movements. *Journal of African Earth Sciences,* **36**(3), 207-214, doi:10.1016/S0899-5362(03)00023-X

Njome, S. M. & de Wit, M. J., (2014). The Cameroon Line: Analysis of an intraplate magmatic province transecting both oceanic and continental lithospheres: Constraints, controversies and models. *Earth-Science Reviews,* **139**, 168-194, doi:10.1016/j.earscirev.2014.09.003

Oxburgh, E. R. and Turcotte, D. L., (1978). Mechanisms of continental drift. *Rep. Prog. Phys.* **41,** 1251-1312.

Paulson, A., Zhong, S. & Wahr, J., (2007). Limitations on the inversion for mantle viscosity from postglacial rebound. *Geophysical Journal International,* **168**(3), 1195-1209, doi:10.1111/j.1365-246X.2006.03222.x

Peltier, W. R., (1974). The impulse response of a Maxwell Earth. *Review of Geophysics,* **12**(4), 649-669, doi:10.1029/RG012i004p00649

Peltier, W. R. & Tushingham, A. M., (1989). Global sea level rise and the greenhouse effect: Might they be connected? *Science,* **244**, 806-810.

Perlingerio, G., Vasconcelos, P. M., Knesel, K. M., Thiede, D. S. & Cordani, U. G., (2013). $^{40}Ar/^{39}Ar$ geochronology of the Fernando de Noronha Archipelago and implications for the origin of alkaline volcanism in the NE Brazil. *Journal of Volcanology and Geothermal Research,* **249**, 140-154, doi:10.1016/j.jvolgeores.2012.08.017

Petit, C., (2010). Continental hearts: Ancient expanses called cratons pose a geological puzzle. *Science News* **178**(13), 22-26, doi:10.1002/scin.5591781325. ISSN 0036-8423

Pollack, H. N., 1986. Cratonization and thermal evolution of the mantle. *Earth and Planetary Science Letters*, **80**, 175-182, doi:10.1016/0012-821X(86)90031-2

Poudjom Djomani, Y. H., Nnange, J. M., Diament, M., Ebinger, C. J. & Fairhead, J. D., (1995). Effective elastic thickness and crustal thickness variations in west central Africa inferred from gravity data. *Journal of Geophysical Research: Solid Earth*, **100**(B11), 22047-22070, doi:10.1029/95JB01149

Rankenburg, K., Lassiter, J. C. & Brey, G., (2005). The role of continental crust and lithospheric mantle in the genesis of Cameroon Volcanic Line lavas: Constraints from isotopic variations in lavas and megacrysts from the Biu and Jos Plateaux. *Journal of Petrology*, **46**(1), 169-190, doi:10.1093/petrology/egh067

Reusch, A. M., Nyblade, A. A., Wiens, D. A., Shore, P. J., Ateba, B., Tabod, C. T. & Nnange, J. M., (2010). Upper mantle structure beneath Cameroon from body wave tomography and the origin of the Cameroon Volcanic Line. *Geochemistry, Geophysics, Geosystems*, **11**(10), 1-17, doi:10.1029/2010GC003200

Reusch, A. M., Nyblade, A. A., Tibi, R., Wiens, A. D., Shore, P. J., Bekoa, A., Tabod, C. T. & Nnange, J. M., (2011). Mantle transisiton zone thickness beneath Cameroon: Evidence for an upper mantle origin for the Cameroon Volcanic Line. *Geophysical Journal International*, **187**(3), 1146-1150, doi:10.1111/j.1365-246X.2011.05239.x

Ricard, Y. & Vigny, C., (1989). Mantle dynamics with induced plate tectonics. *Journal of Geophysical Research*, **94**, 17543-17559.

Richter, F. M., (1973). Convection and the large-scale circulation of the mantle. *J. Geophys. Res.*, **78**, 8735-8745, doi:10.1029/JB078i035p08735

Richter, F. M. & Parsons, B., (1975). On the interaction of two scales of convection in the mantle. *J. Geophys. Res.*, **80**(17), 2529-2541

Ritter, X., Sanchez-Valle, C., Sator, N., Desmaele, E., Guignot, N., King, A., Kupenko, I., Berndt, J. & Guillot, B., (2020). Density of hydrous carbonate melts under pressure, compressibility of volatiles and implications for carbon melt mobility in the upper mantle. *Earth and Planetary Science Letters*, **533**(116043), doi:10.1016/j.epsl.2019.116043

Rudolph, M. L., Moulik, P. & Lekić, V., (2020). Bayesian inference of mantle viscosity from whole-mantle density models. *Geochemistry, Geophysics, Geosystems*, **21(**11), doi:10.1029/2020GC009335

Rutter, E. H. & Brodie, K. H., (2004a). Experimental grain size-sensitive flow of hot-pressed Brazilian quartz aggregates. *Journal of Structural Geology*, **26**(11), 2011-2013, doi:10.1016/j.jsg.2004.04.006

Rutter, E. H. & Brodie, K. H., (2004b). Experimental intracrystalline plastic flow in hot-pressed synthetic quartzite prepared from Brazilian quartz crystals. *Journal of Structural Geology*, **26**, 259-270, doi:10.1016/S0191-8141(03)00096-8

Rybacki, E. & Dresen, G., (2000). Dislocation and diffusion creep of synthetic anorthite aggregates. *Journal of Geophysical Research*, **105**(B11), 26017-26036

Rybacki, E., Gottschalk, M. Wirth, R. & Dresen, G., (2006). Influence of water fugacity and activation volume on the flow properties of fine-grained anorthite aggregates. *Journal of Geophysical Research*, **111**(B03203), doi:10.1029/2005JB003663

Schubert, G., Turcotte, D., & Olson, P., (2001). Viscosity of the Mantle. In *Mantle Convection in the Earth and Planets*, pp. 212-250 & pp. 940, Cambridge: Cambridge University Press, doi:10.1017/CBO9780511612879.006

Schubert, G., (2015). Treatise on Geophysics. 2nd ed. Elsevier. ISBN: 978-0-444-53803-1

Sleep, N. H., (2003). Survival of Archean cratonic lithosphere. *Journal of Geophysical Research,* **108**(B6), 2302, doi:10.1029/2001JB000169

Sleep, N. H., (2007). Edge-modulated stagnant-lid convection and volcanic passive margins. *Geochemistry, Geophysics, Geosystems*, **8**(12), doi:10.1029/2007GC001672

Souza, Z. S. D., Vasconcelos, P. M., Knesel, K. M., da Silveira Dias, L. G., Roesner, E. H., de Farias, P. R. C. & de Morais Neto, J. M., (2013). The tectonic evolution of Cenozoic extensional basins, northeast Brazil: geochronological constraints from continental basalt $^{40}Ar/^{39}Ar$ ages. *Journal of South American Earth Sciences*, **48**, 159-172, doi10.1016/j.jsames.2013.09.008

Stein, M. & Hofmann, A. W., (1994). Mantle plumes and episodic crustal growth. *Nature*, **372**, 63-68, doi:10.1038/372063a0

Storey, B. C., (1995). The role of mantle plumes in continental breakup: case histories form Gondwanaland. *Nature*, **377,** 301-301, doi:10.1038/377301a0

Suh, C. E., Ayonghe, S. N., Sparks, R. S. J., Annen, C., Fitton, J. G., Nana, R. & Luckman, A., (2003). The 1999 and 2000 eruptions of Mount Cameroon: eruption behaviour and petrochemistry of lava. *Bulletin of Volcanology*, **65**, 267-281.

Tappe, S., Romer, R. L., Stracke, A., Smart, K., Muehlenbachs, K. & Torsvik, T. H., (2017). Sources and mobility of carbonate melts beneath cratons, with implications for deep carbon cycling, metasomatism and rift initiation. *Earth and Planetary Science Letters*, **466**, 152-167, doi:10.1016/j.epsl.2017.03.011

Tatsumoto, M. Nakamura, Y., (1991). DUPAL anomaly in the Sea of Japan: Pb, Nd, and Sr isotopic variations at the eastern Eurasian continental margin. *Geochimica et Cosmochimica Acta,* **55**, 3697-3708, doi:10.1016/0016-7037(91)90068-G

Thieulot, C., (2011). FANTOM: Two-and three-dimensional numerical modelling of creeping flows for the solution of geological problems. *Physics of the Earth and Planetary Interiors,* **188**(1-2), 47-68, doi:10.1016/j.pepi.2011.06.011

Till, C. B., Elkins-Tanton, L. T. & Fischer, K. M., (2010). A mechanism for low-extent melts at the lithosphere-asthenosphere boundary. *Geochemistry, Geophysics, Geosystems,* **11**(10), doi:10.1029/2010GC003234

Toteu, S. F., Penaye, J. & Poudjom Djomani, Y. H., (2004). Geodynamic evolution of the Pan-African belt in central Africa with special reference to Cameroon. *Canadian Journal of Earth Science,* **41**(1), 73-85, doi:10.1139/e03-079

Van Hinsbergen D. J. J., Buiter, S. J. H., Torsvik, T. H., Gaina, C. & Webb, S. J., (2011). The formation and evolution of Africa from the Archaean to Present: introduction. *Geological Society, London, Special Publications,* **357**, 1-8, doi:10.1144/SP357.1

Van Hunen, J., Huang, J., Zhong, S., (2003).The effect of shearing on the onset and vigor of small-scale convection in a Newtonian rheology. *Geophysical Research Letters*, **30**(19), doi:10.1029/2003GL018101

Van Hunen, J., Zhong, S., Shapiro, N. M. & Ritzwoller, M. H., (2005). New evidence for dislocation creep from 3-D geodynamical modeling of the Pacific upper mantle structure. *Earth and Planetary Science Letters,* **238**(1-2), 146-155, doi:10.1016/j.epsl.2005.07.006

Van Keken, P. E., Karato, S. & Yuen, D. A., (1996). Rheological control of oceanic crust separation in the transition zone. *Geophysical Research Letters*, **23**(14), 1821-1824, doi:10.1029/96GL01594

Van Wijk, J. W., Baldridge, W. S., van Hunen, J., Goes, S., Aster, R., Coblentz, D. D., Grand, S. P. & Ni, J., (2010). Small-scale convection at the edge of the Colorado Plateau: Implications for topography, magmatism, and the evolution of Proterozoic lithosphere. *Geology*, **38**(7), 611-614, doi: 10.1130/G31031.1

Wang, J., Zhao, D. & Yao, Z., (2017). Seismic anisotropy evidence for dehydration embrittlement triggering intermediate-depth earthquakes. *Scientific Reports,* **7**(2613), doi:10.1038/s41598-017-02563-w

Weaver, B. L., (1991). The origin of ocean island basalt end-member compositions: Trace element and isotopic constraints. *Earth and Planetary Science Letters*, **104,** 381-397.

Wen, L. X., Silver, P., James, D. & Kuehnel, R., (2001). Seismic evidence for a thermos-chemical boundary at the base of the Earth's mantle, *Earth Planetary Science Letters*, **189**, 141-153.

Wenker, S. & Beaumont, C., (2017). Can metasomatic weakening result in the rifting of cratons? *Tectonophysics*, **746**, 3-21, doi:10.1016/j.tecto.2017.06.013

White, W. M., (2010). Oceanic island basalts and mantle plumes: The geochemical perspective. *Annual Review Earth and Planetary Science*, **38**, 133-160, doi:10.1146/annurev-earth-040809-152450

Wilson, J. T., (1963). Hypothesis of earth's behaviour. *Nature*, **198** (4884), 925–929, doi:10.1038/198925a0

Woodhead, J. D., Greenwood, P., Harmon, R. S. & Stoffers, P., (1993). Oxygen isotope evidence for recycled crust in the source of EM-type ocean island basalts. *Nature*, **362**, 809-813.

Yuan, H. & Dueker, K., (2005). Teleseismic P-wave tomogram of the Yellowstone Plume. *Geophysical Research Letters*, **32**(L07304), 1-4, doi:10.1029/2004GL022056

Zindler, A. & Hart, S., (1986). Chemical geodynamics, *Annual Review Earth and Planetary Science*, **14**, 493-571

Appendices

Appendix A

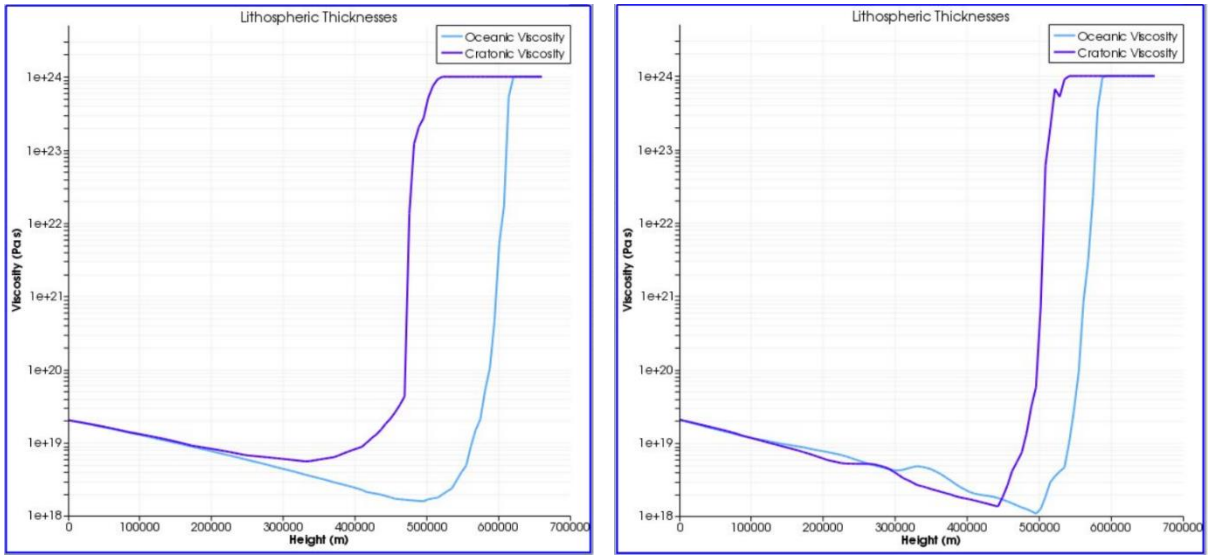

Appendix A. The viscosity profile through both cratonic and oceanic lithosphere from the beginning to the end of the 2D static lithosphere model run, showing the change in lithospheric thickness over the 300 Myr run.

Appendix B

```
########## Velocity ##########
# The half-spreading rate choosen is u0=3cm/yr

subsection Boundary velocity model
  set Prescribed velocity boundary indicators = top:function, right:function
  set Tangential velocity boundary indicators = left, bottom
  subsection Function
    set Function constants  = u0=0.02, x0=10000
    set Variable names      = x,y,t
    set Function expression = if (t<100e6, 0, if(x<x0,(1-(x/x0-1)*(x/x0-1))*u0,-u0*tanh(((660e3-y)-330000)/50000))); 0
  end
end
```

Appendix B. The implementation of the: initial delay in spreading, half-spreading rate, and the subsequent velocity equation on the right hand side boundary.

Appendix C

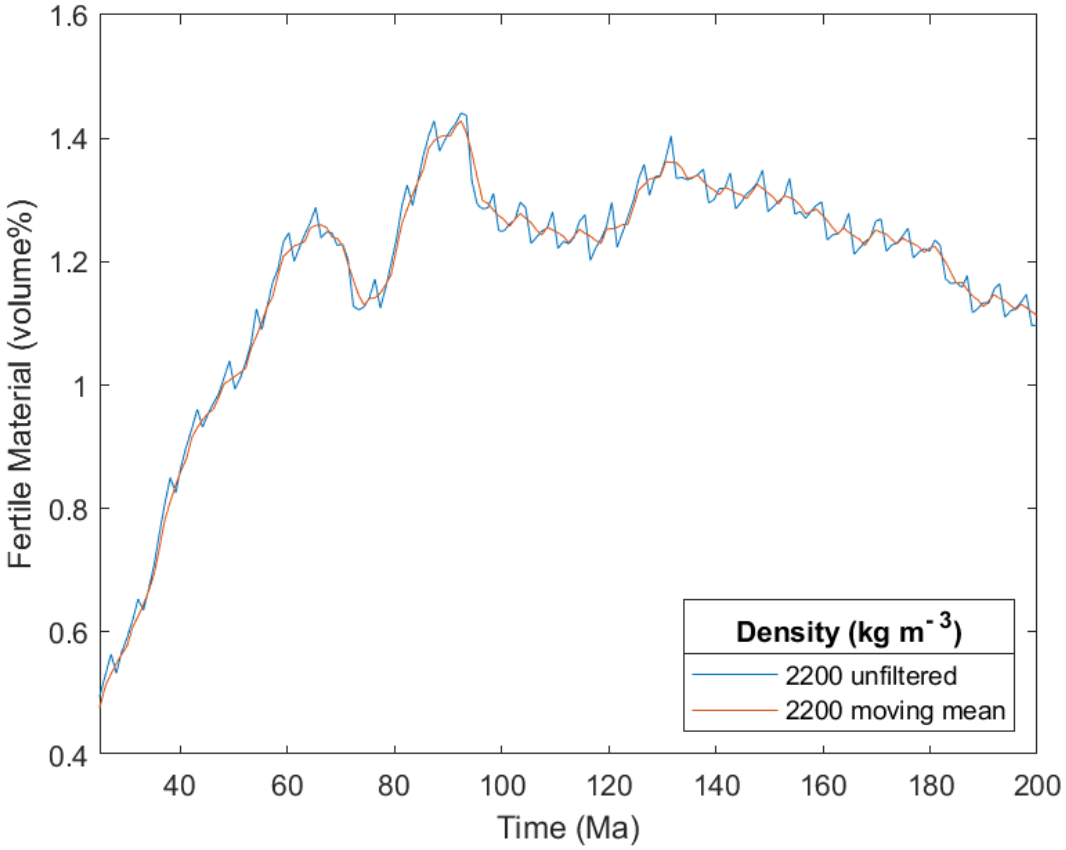

Appendix C. The effect of filtering data using the movemean function in MATLAB. Due to the movement of the white box collecting data based on grid points, there is a continuous fluctuation as the box moves. Here the movemean filtering smooths out this periodic movement, whilst keeping the changes seen in the model.